Pions in Neutron-rich Matter: Implications for Neutron Stars and Supernovae

Bryce Fore

A dissertation
submitted in partial fulfillment of the
requirements for the degree of

Doctor of Philosophy

University of Washington

2021

Reading Committee:
Sanjay Reddy, Chair
Larry Mclerran
Silas Beane

Program Authorized to Offer Degree:
Physics

University of Washington

Abstract

Pions in Neutron-rich Matter:
Implications for Neutron Stars and Supernovae

Bryce Fore

Chair of the Supervisory Committee:
Sanjay Reddy
Department of Physics

The effects of pions on astrophysical phenomena have been studied for decades. In the 1970s, Migdal and Sawyer independently proposed that pions could condense in dense matter due to attractive p-wave interactions with nucleons. Many other studies have investigated the possibility of pion condensation in dense neutron-rich matter. However, due to the strong interactions between nucleons and pions, there is a large degree of uncertainty in condensate formation. We have considered the effects of a thermal population of negatively charged pions, where the enhancement from strong interactions with nucleons is taken into account with a virial approximation and find that even without the formation of a condensate, pions are likely to have a large effect on neutron-rich matter at high densities and temperatures, such as the conditions in the proto-neutron star of a core-collapse supernova or inside neutron star mergers. This model is also used for calculations of neutrino mean free path in the processes $\nu_\mu + \pi^- \to \mu^-$ and $\bar{\nu}_\mu + \mu^- \to \pi^-$ as well as calculations of axion emissivity through a pion induced reaction $\pi^- p \to na$.
Due to the pions repulsive s-wave interaction with nucleons and strongly attractive p-wave interactions, the majority of studies have focused on investigations of pion condensation at finite momentum. Early studies concluded that a condensed state at finite momentum was favored, but later more sophisticated analysis found that these results may not be robust at the densities encountered in neutron stars. In this thesis we reevaluate the possibility of s-wave pion condensation through improved calculations of the pion self-energy using Chiral Perturbation Theory.

CONTENTS

PREFACE

The contents of section 3.2 and 3.3 as well as section 4.2 are based on the content of the published paper: Bryce Fore and Sanjay Reddy. Pions in hot dense matter and their astrophysical implications. Physical Review C, 101(3):35809, 2020. This work was inspired by calculations of the effect of muons in supernova explosions [1]. We considered if a thermal population of pions may have similarly large effects. The model-independent virial approximation was a logical choice to include the effects of the nucleon interactions on the pion population. My contribution to this work included creating an equation of state (EOS) which included the pions by using the virial approximation and using our pseudo-potential model for the pion self-energy. We considered various forms the pseudo-potential could take, based on results which have worked well for nucleons, and I was tasked with determining which form was able to most closely reproduce our virial approximation results. Martin Hoferichter, beyond contributing the phase shift data for virial approximation and pseudo-potential calculation, was of tremendous help in understanding the basis conversion necessary to use the phase shift data in our calculations. The results in section 4.2 arose from joint discussions of the effects of pions. I realized the reactions $\nu_\mu + \pi^- \to \mu^-$ and $\bar{\nu}_\mu + \mu^- \to \pi^-$ would be allowed and would modify the neutrino mean free path in the presence of pions. I performed the mean free path calculations in this section and used our pion model to compare them to other relevant reaction channels.

The content of sections 5.2 is based on the publication: Pierluca Carenza, Bryce Fore, Maurizio Giannotti, Alessandro Mirizzi, and Sanjay Reddy. Enhanced Supernova Axion Emission and Its Implications. Physical Review Letters, 126(7):071102, 2021. Pierluca Carenza, Maurizio Giannotti, and Alessandro Mirizzi realized that the larger population of pions predicted by my virial model increased the production of axions through the channel $\pi^- p \to na$, which was previously thought to be a negligible effect due to the assumed small abundance of pions. My contribution to this work was to provide calculations of the pion population, using my previously created numerical EOS, for the axion emissivity calculations of Pierluca Carenza.

The calculated axion emissivity from this pion-induced reaction was large enough that inclusion into a supernova simulation was the next logical step. Tobias Fischer, who had previous experience with calculations of axion emissivity within supernova simulations, agreed to include the pion-induced reaction into his supernova simulations, resulting in the publication: Tobias Fischer, Pierluca Carenza, Bryce Fore, Maurizio Giannotti, Alessandro Mirizzi, and Sanjay Reddy. Observable signatures of enhanced axion emission from protoneutron stars. Physical Review D, 104(10):103012, 2021. My contribution to this work required modifications to my numerical EOS including pions such that it would function with any nuclear EOS table, with the assumption that the direct effect of the pions on the nucleon self-energies is negligible. Tobias provided the equation of state table he used within his supernova simulation, and I returned a corresponding table which specified the number density of pions and their self-energy as a function of momentum, as well as the energy density, entropy per baryon, and pressure contribution of the pions.

During the publication of my first paper, I began work with Steven Harris and Mark Alford on modifications to the bulk viscosity of dense matter from the reactions outlined in section 4.2. The analysis of these reactions requires analysis of the full system as the effects from individual reaction channels to the bulk viscosity cannot be easily separated. The complex dependence of the bulk viscosity on each reaction channel is highlighted by appendix E and F. The publication of this work has been delayed by unfortunate timing with respect to Steven's graduation and my own, but we have made great progress in the time between our respective graduations such that it is now close to publication. My contribution to this work was the modification of my pion EOS to account for trapped neutrinos, so that I was able to provide calculations of the susceptibility parameters along with density- and temperature-dependent information from the EOS. Steven provided an analytic expression of the full bulk viscosity including pions and has used the results I provide to calculate the reaction rates and bulk viscosity. My method of adding pions to existing nuclear EOS is described in appendix A. The various modifications to this model, which apply to each of the situations in which I have used it, are also detailed in appendix A. Additionally, the changes required to use our pseudo-potential model for the pion self-energy are described in appendix B.

Lastly, the contents of section 6 are based on the work of Sanjay Reddy, Neill Warrington, and myself. My contribution to this project has been in the construction of a model for the EOS of neutron matter with a pion condensate, using calculations of the pion self-energy from Chiral Perturbation Theory (χPT). Neill and Sanjay performed the self-energy calculations. Additionally, we have received tremendous guidance in this work from Norbert

Kaiser, who is intimately familiar with the χPT theory calculations. This work is in the final stages of writing and was almost ready for publication. However, in the process of adding the full pion self-energy to the model of the condensed state, I discovered the that the self-energy's dependence on baryon density, proton fraction, and the charge chemical potential has dramatic effects on the onset of condensation. With a subset of the full terms contributing to the full self-energy, I find that there exists a first-order phase transition to the pion condensed state. This new development requires more investigation. My analysis using the full self-energy is underway and will be completed soon.

1. INTRODUCTION

1.1. Core-collapse supernovae

All stars fuse lighter elements into elements as heavy as iron, releasing the energy which opposes the gravitational attraction, keeping the star from falling in on itself. Iron is the stopping point for this process because fusion to heavier elements no longer releases energy. Stars more massive than about $8M_\odot$ build up cores of iron which gradually increase in mass, supported by the degeneracy of electrons rather than the energy of fusion. As the mass of the core grows the electrons become more relativistic. The pressure they provide now increases less rapidly with increasing density than was the case when electrons were nonrelativistic [2]. When the core grows to a mass exceeding the Chandrasekhar limit ($\sim 1.4M_\odot$), the core can no longer be supported by electron degeneracy pressure and begins to collapse [3]. As the core collapses, electrons and protons form neutrons and electron neutrinos and the core is eventually stopped from falling further due to neutron degeneracy pressure as well as nuclear interactions within the core of the star. At this point, the core has formed a proto-neutron star (PNS), which can reach temperatures up to several 10^{11} K (≈ 10 MeV), and densities larger than nuclear saturation density [4]. If the progenitor star's mass was larger than $30M_\odot$, then neutron repulsion will not be strong enough to support the remnant and the star will collapse into a black hole or some other, more exotic, form of matter.

After the core collapse stops and the outer layers of the star impact the newly formed surface of the PNS, the sudden stop of the outer layers triggers the formation of a shock wave which travels through the outer layers of the star. After propagating around 100 to 200 km the shock wave stalls due to energy loss from neutrino production and nuclear dissociation in the material it passes. The shock wave is eventually revived and within seconds accelerates outward, expelling the stellar mantle [5]. The means of the shock wave's resuscitation has been under investigation for decades. The most likely candidate currently seems to be the delayed heating from neutrinos, formed from electron capture on protons in the core [3, 5, 6], possibly assisted by the effects of rotation, convection, or magnetic fields [5]. The complex nature of the supernova makes accurate, three-dimensional simulations only recently feasible, but they are still expensive and resource intensive. This is partially why research into the explosion mechanism has been delayed [7].

Neutrinos produced within the PNS have a mean free path on the order of 10 cm which is much smaller than the radius of the PNS (> 10 km) [5]. This means that neutrinos will be temporarily trapped within the PNS, only slowly diffusing out of the star for 10 to 20 seconds. However, the neutrino mean free path scales as the inverse of the square of the mean neutrino energy, so after about 50 seconds the mean free path becomes larger than the radius of the star, allowing neutrinos to freely stream out of the, now transparent, neutron star [5]. Within a few days, the loss of neutrinos will cool the PNS to temperatures of about 1 MeV [8]. The neutrino emission is powered by the binding energy released in the collapse of the iron core into a neutron star ($2 - 5 \times 10^{53}$ ergs)[9]. Further analysis of the neutrino signal suggests each of the 6 neutrino degrees of freedom should carry about 0.5×10^{53} ergs of energy over a timescale of about 1 second with typical energies on the order of several 10's MeV [10]. Together the neutrinos account for almost 99% of the radiated energy. The most significant supernova observation in nuclear astrophysics is supernova 1987A, from which 30 neutrinos were observed over the course of about fifteen seconds [11, 12]. This observation confirms the timescale of neutrino emission as well as the overall energy release [5].

The progenitor star's core has nearly equal amounts of neutrons, protons, and electrons. This corresponds to an electron fraction, the ratio of the density of electrons to the density of protons plus the density of neutrons, of about 0.5. During the collapse of the core, which was previously supported by a degenerate electron gas, it is energetically favorable for protons to capture electrons and produce neutrons and neutrinos. This results in a decrease of the electron fraction and decrease of the pressure the electrons created to support the core, further accelerating the collapse [7, 13]. Once the collapse has stopped, and the newly formed PNS is supported by neutron degeneracy pressure, the star reaches chemical equilibrium between the neutrons, protons, electrons, and (temporarily) the trapped neutrinos.

$$\mu_n - \mu_p = \mu_e - \mu_{\nu_e} \tag{1.1}$$

Once the stellar remnant becomes transparent to neutrinos, the electron neutrino chemical potential will drop to zero, reaching a condition called beta equilibrium.

$$\mu_n - \mu_p = \mu_e \tag{1.2}$$

With increasing density in the newly formed neutron star, the electron chemical potential increases. It can reach values exceeding the rest mass of the muon, at which point a significant population of muons can appear [1].

The explosion of the supernova is a known and important site of the creation of the heavy elements, also known as nucleosynthesis. The vast majority of the material from the progenitor star is ejected from the supernova and expands outward at a great velocity. This material can be seen at all wavelengths of light between radio and X rays, hinting at the processes happening within [2]. The composition of the ejecta depends on how quickly it expands. If the expansion is fast then some of the material can "freeze out", meaning that it is no longer undergoing significant interactions with neutrinos, and will subsequently be slightly neutron-rich. If the expansion is slower, then the bulk of the material will have time to interact with the neutrinos escaping the PNS, pushing it toward a more proton-rich composition. This may make supernovae a site for the rp-process, where protons are rapidly captured by smaller nuclei producing larger nuclei [6, 7, 9, 13]. During its life, the progenitor star created elements as heavy as iron, much of which ends up expanding outward as ejecta from the supernova. In the violent explosion, many of the heaviest elements are formed. The many generations of stars that have passed since the beginning of the universe have produced most of the elements heavier than lithium.

1.2. Neutron stars

The existence of neutron stars was theorized quickly after the discovery of the neutron in 1932. The original models of neutron stars consisted of a dense, free neutron gas. Theoretical work on neutron stars was slow due to a lack of observational evidence. Since neutron stars are degenerate and no longer able to produce energy, it was assumed they would be very difficult to observe at astronomical distances. However, the discovery of pulsars in 1967 created the first avenue for neutron star observation [2, 8]. A pulsar is an astrophysical object which produces periodic signals of detectable radiation. The mechanism for the pulsations is assumed to be a cone of radiation of small angular width which emitted along the magnetic axis of a compact object. The rotation beams the radiation cone in our direction with each rotation. Calculations by Woltjer showed that the conservation of magnetic flux in a star contracting from a red giant to a neutron star could produce enormous magnetic fields [14]. It is currently widely believed that the compact object which powers pulsars are highly magnetized neutron stars [2]. Since their discovery, over 1000 pulsars have been identified.

After a supernova, a neutron star begins its life as a high temperature, 50 MeV [5], proto-neutron star with a neutrino mean free path much less than its radius. The neutron star cools via an initially slow emission of neutrinos. Because the neutrino mean free path is inversely proportional to the square of the neutrino energy, the neutrino mean free path becomes greater than the neutron star radius, and thus the star becomes transparent to neutrinos, in about one minute [5, 9]. Once the neutrinos can freely stream from the star, it rapidly cools to 1 MeV over the course of the first day [8]. Within 10 to 100 years, the star reaches an isothermal state where the temperature will be less than 1 MeV [5, 8].

There are bounds for both the minimum mass and maximum mass for stable neutron stars. The maximum mass of a neutron star, also called the Tolman–Oppenheimer–Volkoff limit, must be larger than the largest observed neutron star which is currently PSR J0740+6620, which was measured in 2019 to have a mass of $2.14M_\odot$ [15]. This is thought to be very close to the theoretical maximum possible mass for neutron stars. The minimum stable neutron star mass comes from knowledge of their formation. It may be possible for a theoretical neutron star to be stable with a mass of about $0.1M_\odot$, however, the only known way to form neutron stars is from the core of a star undergoing a core-collapse supernova, so a more practical bound for the minimum mass can be found by taking this into account. The PNS produced by the core collapse is very lepton-rich and will be unbound for masses less than about $1M_\odot$ [5, 8].

The matter content of the NS can vary greatly depending on its depth. Fig. 1 shows the most prevalent forms of matter with a neutron star with mass $1.4M_\odot$ in radial view of the star. The outer layers of the star, called the crust, consist of bound nuclei and a sea of electrons at densities below about $10^{11} g/cm^3$. Higher densities favor more neutron rich nuclei. When the neutron drip density is reached at about 4×10^{11} g/cm^3, free neutrons appear in the medium as the outermost neutrons are no longer bound to nuclei [8, 13]. The crust has a subdominant effect on global properties of NSs such as mass or radius [13], while the bulk of the neutron star is composed of matter with density closer to or greater than nuclear saturation density, $n_0 = 0.16$ fm^{-3}, from the core of the star. In the core, near densities of n_0, the nuclei dissolve and the matter becomes a uniform liquid of neutrons, protons, electrons, and small fractions of other light particles like muons and perhaps pions [8]. This view of matter is reasonable until about $2n_0$ in the inner core where the composition

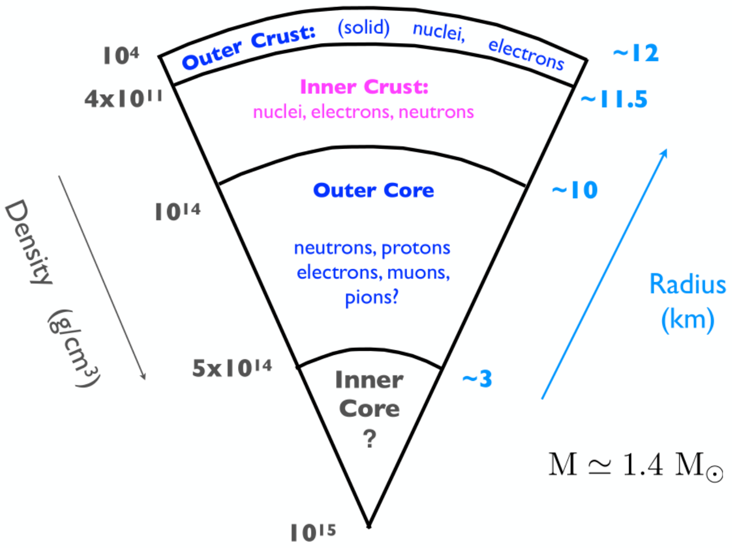

FIG. 1. Radial slice of a 1.4 solar mass neutron star showing the expected matter content. The outermost layer of the crust is composed of nuclei and a Fermi gas of electrons. Deeper within the crust of the star, a Fermi gas of neutrons which are not bound to nuclei, appear. Within the outer layer of the core nuclei are no longer stable instead favoring a Fermi gas of neutrons and protons. Other particles like muons become more prevalent. The composition within the inner core of the star is still under investigation.

and structure become more uncertain [13]. Possible and proposed forms for the dominant composition of matter in the inner core include: pion or kaon condensates, hyperonic matter, and quark matter [8, 13].

1.3. Neutron star mergers

It's common for stars to form in binary pairs, in fact, about half of all stars are in binaries [2]. So binary pairs of neutron stars can be formed from stellar binaries which both have masses within the $8 - 30M_\odot$ range required to form neutron stars. The exact rate we can expect to have a binary neutron star merger with a set time and radius is a complex quantity to predict due to many assumptions, including the mass distribution of stars, however, one estimate is given as 20 to 600 $\text{Gpc}^{-3}\ \text{yr}^{-1}$ [16].

A pair of binary stars gradually radiates its orbital energy as gravitational waves, GW, decreasing the distance between them. Once a pair of neutron stars are close enough deform one another through gravitational interactions the energy radiated increases dramatically and soon after the pair merge in a violent process which produces, among other things, a burst of gamma rays. The advent of gravitational wave observatories has opened a new window into these events. In figure 2 the sensitivity of some current and planned gravitational wave telescopes are shown in comparison to the signal of a binary neutron star merger and a binary black hole merger at a distance of 100 Mpc. Observation of GW from the point particle phase of the merger is interesting in many ways, but the effects of the dense matter EOS on it are negligible. As the stars approach one another close enough to affect each other tidally, the signal from the gravitational waves is affected by how easily deformed the stars are. Giving useful information in the form of the tidal deformability parameter, Λ. The post-merger GW signal is drastically affected by the EOS and accurate measurement of this signal would be incredibly useful to investigations of the dense matter EOS. To contrast this we can see from the plot of the binary black hole merger signal, which is not affected by the matter EOS, is comparatively simpler. The differences in these regions allow us to determine the origin of gravitational wave signals from different types of mergers: NS-NS, BH-BH, and NS-BH.

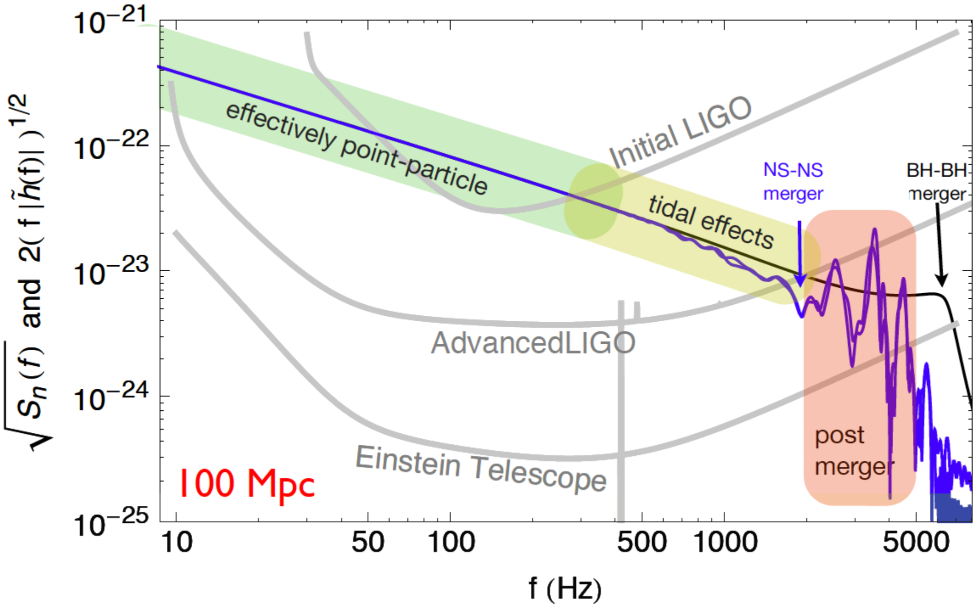

FIG. 2. Gravitational wave signal from a binary neutron star merger and a binary black hole merger at a distance of 100 Mpc compared to the sensitivity of LIGO and Einstein Telescope. As the merger progresses the frequency increases and the strain decreases. Only when the NS are able to interact through tidal effects do the effects of the nuclear EOS begin to affect the gravitational wave signal. From [17] based on results from [18]

Due to the large amount of time required to radiate the orbital energy, typical neutron stars in a merger event will begin at very low temperatures (< 1 MeV) due to energy loss from neutrino radiation, until the dynamics of the merger increase the temperature dramatically. During the merger matter goes from cold, equilibrium matter with typical densities of 2 to 3 times nuclear saturation density, to densities up to 5 to 6 times nuclear saturation density and temperatures from 50 to 500 MeV on a timescale of milliseconds [19]. The merger also comes with increased values of the electron chemical potential which, in equilibrium, is tied directly to the appearance of other, more massive charged particles.

Besides supernova, neutron star mergers are the largest site for nucleosynthesis. The exact composition of nuclei created in both processes is still under active investigation, however, it is known that the most massive nuclei are predominantly created in neutron star mergers. During the merger large amounts of material are ejected. This material begins just as neutron rich as the star it came from. This makes neutron star mergers excellent sites for r-process, or rapid neutron-capture process. This process entails the rapid capture of free neutrons by heavy seed nuclei, at rates faster than the nuclei can decay. the seed nuclei capture neutrons until they reach the neutron drip line, which is the point where the binding energy per nucleon in the nuclei reaches zero due to the repulsive neutron-neutron interactions and thus additional neutrons cannot be bound to the nucleus. At this point the nuclei will beta decay to more stable ratios of protons and neutrons, usually by beta decay of neutrons. If the rapid neutron-capture process is still proceeding at this time then the nuclei will restart this process and capture more neutrons, becoming heavier and heavier.

The most significant observation for neutron star mergers is still comes from GW170817 and its corresponding electromagnetic observations. The detection of the electromagnetic counterpart to the event marked the most significant advancement in multi-messenger astronomy since the observation of a handful of neutrinos from SN1987A. Many impressive discoveries were made thanks to GW170817. For example, the observation of a short gamma-ray burst (GRB), most of which are observed at much larger distances, counterpart to the gravitational waves has confirmed that neutron star mergers are at least one of the sources of these events. Additionally, the days long observation of the electromagnetic counterpart to the GWs is consistent with the production of a large abundance of r-process elements.

1.4. Chiral perturbation theory

Due to its strong coupling, a perturbative treatment of QCD at low energies isn't possible. Instead, we can construct an effective field theory (EFT) to describe the particles and interactions at energies low compared to a specified cutoff energy. One such theory which is very powerful for understanding the interactions of the lightest hadrons is called chiral perturbation theory (ChPT). ChPT is based on the global $SU(3)_L \times SU(3)_R \times U(1)_V$ symmetry of the QCD Lagrangian in the chiral limit (the limit of massless up, down, and strange quarks). The QCD vacuum spontaneously breaks this symmetry to $SU(3)_V \times U(1)_V$ and, by Goldstone's theorem, would result in the existence of 8 massless, scalar particles called Goldstone bosons. The explicit symmetry breaking by the quark masses means no such massless particles exist in nature; however, the up, down, and strange quarks are much lighter than the three heavier quarks, and thus these masses can be treated as a perturbation on the explicit symmetry limit. This results in a theory describing the 8 approximate Goldstone modes. These can be identified with the lightest eight mesons in the full theory which are pions, kaons, and the eta meson [20]. In the remainder of this section I will introduce pion-only chiral perturbation theory which is defined by the breaking of the $SU(2)_L \times SU(2)_R \times U(1)_V$ symmetry to $SU(2)_V \times U(1)_V$, where the strange quark is left out. This theory can be expected to have better convergence than the $SU(3)$ theory because the mass of the up and down quarks is much smaller than that of the strange quarks, and thus chiral symmetry is not broken as badly.

1.4.1. Energy scales

In the process of creating an effective field theory, we must determine what our cutoff energy scale will be. Properly constructed, the EFT will be able to describe processes at low momenta relative to the cutoff. In pion-only chiral perturbation theory, the cutoff must be above the mass of the pions. We can see from table I that the three pions are the lightest of the mesons. The next most massive mesons are the kaons, but because the kaon and eta mesons include strange quarks, they must be produced as pairs, meaning that the cutoff energy scale for our theory is set by the rho meson.

Meson	Mass
π^0	135 MeV
$\pi^\pm$	140 MeV
$K^\pm$	494 MeV
K^0, $\bar{K}^0$	498 MeV
η	548 MeV
ρ	775 MeV

TABLE I. List of the lightest mesons, the lightest 8 of which are the pseudo-scalar octet of approximate Goldstone bosons which exist due to chiral symmetry breaking. Data from [21]

1.4.2. Chiral symmetry

Quarks are the fundamental matter particles of QCD. There are six flavors of quarks which can each come with one of three color charges, red, green, and blue, where color charge is the name for the charge of the strong force. In addition to quarks, the force carriers of QCD are the gluons. These are massless vector bosons similar to the photon, but with an important difference; the gluons carry color charge.

The dynamics of quarks and gluons are governed by the QCD Lagrangian which is given by

$$\mathcal{L} = \sum_i (\bar{q}_i i \not{D} q_i - m_i \bar{q}_i q_i) - \frac{1}{2} \mathrm{Tr}\, G_{\mu\nu} G^{\mu\nu} \tag{1.3}$$

where $G_{\mu\nu}$ is the gluon field strength and D_μ is the color covariant derivative which contains the kinetic term for the quarks and also the couplings to the gluon fields. The kinetic term can be rewritten in terms of right-handed and left-handed quarks, projecting by $(1 \pm \gamma_5)/2$ respectively, as

$$\sum_i \bar{q}_i i \not{D} q_i = \sum_i (\bar{q}_{Li} i \not{D} q_{Li} + \bar{q}_{Ri} i \not{D} q_{Ri}) \tag{1.4}$$

By itself this term respects a $U(2)_L \times U(2)_R$ symmetry where the two left handed quark flavors and two right handed quark flavors can be independently rotated by unitary matrices. One combination of these symmetries, $U(1)_A$, is actually not respected by the measure of the path integral, leaving us with a $SU(2)_L \times SU(2)_R \times U(1)_V$ symmetry. The $U(1)_V$ is just the baryon number and the $SU(2)_L \times SU(2)_R$ is called "chiral symmetry" [22].

As mentioned previously, chiral symmetry is not a symmetry of the full theory. Attempting to write the mass term from Eq. 1.4 will show that it couples the left- and right-handed quarks. This term explicitly breaks chiral symmetry meaning it is only an approximate symmetry for the theory. The $SU(2)_L \times SU(2)_R$ symmetry, in which left and right components are rotated independently, can be rewritten as $SU(2)_V \times SU(2)_A$ where the vector symmetry, $SU(2)_V$, is one where both fields are rotated identically and the axial symmetry, $SU(2)_A$, rotates the fields in the opposite way relative to one another. While the mass term respects the vector symmetry, it does not respect the axial symmetry, meaning the remaining exact symmetry is given by $SU(2)_V \times U(1)_V$. An added complication is that the QCD vacuum spontaneously breaks the chiral $SU(2)_L \times SU(2)_R$ symmetry down to $SU(2)_V$. What this means is that while the Lagrangian respects the full symmetry, the dynamics of the theory create a ground state which is not symmetric with respect to the full symmetry. This means that, if chiral symmetry was exact for QCD, we would find a massless Goldstone boson for each of the continuous symmetry generators that are spontaneously broken. Since chiral symmetry is not exact for QCD, we instead have three light pions corresponding to the three broken generators of the broken $SU(3)_A$ subgroup.

We are specifically interested in how the excitations interact and evolve and so we will parameterize them by

$$\phi = \tau_a \phi_a = \begin{pmatrix} \phi_3 & \phi_1 - i\phi_2 \\ \phi_1 + i\phi_2 & -\phi_3 \end{pmatrix} = \begin{pmatrix} \pi^0 & \sqrt{2}\pi^+ \\ \sqrt{2}\pi^- & -\pi^0 \end{pmatrix} \tag{1.5}$$

Each field ϕ_a comes with a generator of $SU(2)$ which are the Pauli matrices, τ_a. By checking the quantum numbers of the fields and comparing them to the known quantum number of pions, we can reexpress these fields in terms of the pion fields.

Additionally, we can take higher order terms into account in a simple fashion by exponentiation of the ϕ field:

$$U = \exp\left(i \frac{\phi}{f_\pi} \right) \tag{1.6}$$

where the constant $f_\pi \approx 92.4$ MeV which can be found by matching to pion decay $\pi^- \rightarrow \mu^- \nu_\mu$ which is what we do in section 1.4.4 [20].

1.4.3. Chiral Lagrangian

To construct the Lagrangian for our theory of pions, we can write down terms with U which are consistent with our symmetries. The kinetic term must respect the full chiral symmetry. The only allowed term with two derivatives, which will contain the pion kinetic energy terms, is given by

$$\frac{f_\pi^2}{4}\mathrm{Tr}\left(\partial_\mu U \partial^\mu U^\dagger\right) \tag{1.7}$$

All other terms with two derivatives can be written in the same form. The constant $f_\pi^2/4$ is chosen so that it contains the conventional normalization for the kinetic term. Next we would like to include the symmetry-breaking term resulting from the non-zero quark masses. This contribution can be written as

$$\mathrm{Tr}\left(\chi^\dagger U + \chi U^\dagger\right) \tag{1.8}$$

where χ is a matrix containing the quark masses [23].

Putting the terms together, the leading order chiral perturbation theory Lagrangian is given by

$$\mathcal{L}_0^\pi = \frac{f_\pi^2}{4}\left(\mathrm{Tr}\left(\partial_\mu U \partial^\mu U^\dagger\right) + \mathrm{Tr}\left(\chi^\dagger U + \chi U^\dagger\right)\right) \tag{1.9}$$

1.4.4. Charged pion decay

Charged pions undergo decay via the weak interaction to a charged lepton (anti-lepton) and the associated anti-neutrino (neutrino). One might expect, due to phase space considerations, that the decay to the lowest-mass charged lepton, the electron, would be the dominant decay channel. However, charged pions predominantly decay to muons rather than the lighter electrons. This is due to the vector-nature of the weak interaction creating an effect called helicity suppression. Take the decay of a negatively charged pion for example. Decay to an electron and electron anti-neutrino is allowed and observed but would be forbidden if the electron was massless. Because the weak interaction only interacts with the left chirality component if both decay products are massless then they would both have left chirality. However, this would not conserve spin since the originating pion is spin zero. Since the electron is much less massive than the muon this effect results in a suppression of decays to electrons, favoring decay to muon and muon anti-neutrino with more than 99.9% of decays following this channel [24].

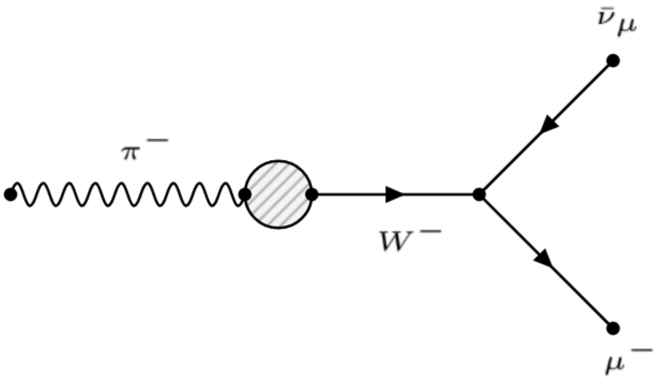

FIG. 3. Tree level Feynman diagram for decay of negatively charged pion.

With the degrees of freedom of the Standard Model, negative pion decay is described by the annihilation of its composite $\bar{u}$ antiquark and d quark into a W^- boson, which subsequently decays to μ^- and $\bar{v}_\mu$. Within our pion-only chiral perturbation theory, the pions are the degrees of freedom, so it is reasonable to describe pion decay instead with a coupling between pions and W bosons. The leading-order Feynman diagram for this process can be seen in Fig. 3.

The pion couples to the W boson with a strength proportional to the weak coupling constant, g, as well as the pion decay constant , f_π. In addition, since this term involves quarks participating in weak interactions, we can expect an element from the CKM matrix to appear, specifically $V_{ud} \approx 0.97$. Finally, this coupling must contain a four-vector to contract with the vector from the lepton factor. Since pions are spin zero, the only four-vector this could be is the pion momentum. The total coupling is thus given by

$$\frac{V_{ud} g f_\pi}{2} P_\pi^\mu \tag{1.10}$$

Because the W boson is so much more massive than the pion, its propagator can be approximated as

$$\frac{-i\left(g_{\mu\nu} - \frac{k_\mu k_\nu}{m_W^2}\right)}{k^2 - m_W^2} \approx \frac{i g_{\mu\nu}}{m_W^2} \tag{1.11}$$

Finally, the vertex connecting the W boson to the leptons is given by

$$-i\frac{g}{2\sqrt{2}}\gamma^\mu(1-\gamma^5) \tag{1.12}$$

It is useful to simplify the expression by rewriting in terms of the Fermi constant,

$$G_F = \frac{g^2}{4\sqrt{2}m_W^2} = 1.16639 \times 10^{-5}\,\mathrm{GeV}^{-2} \tag{1.13}$$

After doing so, the Feynman rule for the invariant amplitude for the weak pion decay reads [20]

$$iM = G_F f_\pi V_{ud} \bar{u}_{\mu^-} \not{P}_\pi (1-\gamma^5) v_{\nu_\mu} \tag{1.14}$$

The squared amplitude can be easily evaluated, and after applying the spin sum and evaluating the trace, in terms of the four-momenta of the particles I find

$$|M|^2 = 8(G_F f_\pi V_{ud})^2[2P_\pi \cdot P_\mu P_\pi \cdot P_\nu - P_\pi \cdot P_\pi P_\mu \cdot P_\nu] \tag{1.15}$$

Evaluating this term in the pion rest frame and evaluating the phase space integral to find the decay rate results in

$$\frac{1}{\tau} = \frac{(G_F V_{ud} f_\pi)^2}{4\pi} m_\pi m_\mu^2 \left(1 - \frac{m_\mu^2}{m_\pi^2}\right)^2 \tag{1.16}$$

The lifetime for the charged pion can be measured by experiment, meaning all the quantities in Eq. 1.16 are known except or the pion decay constant. Calculating its value using these known quantities I find $f_\pi \approx 93$ MeV.

2. DENSE MATTER EQUATION OF STATE

The equation of state (EOS) of cold nuclear matter can be experimentally measured at nuclear saturation density via investigations of nuclei. Investigation of the nuclear EOS at higher densities is less straightforward for Earth based experiments, however, astrophysical observations are able to reveal a wealth of information. One such observation is the discovery of a pulsar with mass larger than $2M_\odot$ [15]. This measurement alone is a very useful constraint since it invalidates any EOS which cannot support neutron stars that massive.

Stable neutron stars can be assumed to be charge-neutral since if they were significantly charged, nearby charges would be pulled in to neutralize them. So for a given EOS it should be assumed that the total number of positive charges overall will be equal to the total number of negative charges. For example, in matter containing only neutrons, protons, and electrons we would expect the fraction of electrons to be equal to the fraction of protons.

Another simplifying assumption that can be made for stable neutron stars is that of beta equilibrium. Neutrons constantly undergo the process $n \to p + e^- + \bar{\nu}_e$ but for a stable system we should expect the neutrons to be replenished at the same rate. Since neutrinos are not trapped in isothermal neutron stars, we can expect the process $p + e^- \to n + \nu_e$ to occur just as often. This gives us a relation on the chemical potentials of neutrons, protons, and electrons: $\mu_n = \mu_p + \mu_{e^-}$. An equivalent description can be found using the fact that both baryons and charge are conserved. Each of these conserved quantities will come with a chemical potential, μ_B and μ_Q, respectively. Neutrons only have baryon number and no charge, so their chemical potential is μ_B. Similarly, electrons have charge but no baryon number. Protons receive a contribution from both chemical potentials [25]. Using either of these descriptions of beta equilibrium one can see that muons should have equal chemical potential to electrons and, assuming neutrinos are not trapped, pions should as well. The equilibrium of the process of neutron decay and electron capture on protons is what creates the beta equilibrium condition. This occurs on the timescale of the weak interaction, so events occurring faster than this, such as supernova or neutron star mergers, can push matter out of beta equilibrium. Note however that the presence of pions can possibly equilibrate the proton and neutron fractions faster via the reaction $\pi^- + p + n \leftrightarrow n + n$ which occurs purely through strong interactions. More investigation is needed to determine if and when this reaction can actually equilibrate faster than the neutron decay/electron capture channel [26]. In section 4.4, we investigate a system where this reaction equilibrates the proton and neutron fractions infinitely quickly.

The remainder of this section will focus on different aspects of matter found in neutron stars. Section 2.1 will discuss the relation between the EOS of dense matter and its mass-radius relationship while sections 2.2 and 2.3 will outline two different types of models for uniform nuclear matter, giving examples of each.

2.1. Mass-Radius Relationship

The relationship between mass and radius of stellar bodies is determined by the forces which oppose the pull of gravity. For main sequence stars like our sun, the thermal pressure of fusion is able to oppose the forces of gravity for most of the star. Within the cores of stars that are massive enough to produce iron through fusion, fusion in the core no longer produces energy and the star is supported by the degeneracy pressure of electrons instead. This is the same effect which supports white dwarfs. For these types of stars, the relation between mass and radius can be expressed through the Newtonian equations for stellar structure

$$\begin{aligned} \frac{dP(r)}{dr} &= -\frac{GM(r)\rho(r)}{r^2}, \\ \frac{dM(r)}{dr} &= 4\pi\rho(r)r^2 \end{aligned} \tag{2.1}$$

Where $M(r)$ is the cumulative mass inside a radius r and the EOS $\rho(P)$ must be included to solve the system.

At larger masses, the Fermi gas of electrons will increase in energy. As the electrons reach relativistic energies the amount of pressure they can provide the system decreases, relative to non-relativistic electrons, creating an upper limit on the mass where the electrons are no longer able to support the object. This is called the Chandrasekhar limit and is equal to about 1.4 times the mass of our sun. Passing this limit and collapsing results in an object that is supported by a combination of neutron degeneracy and nuclear interactions, called a neutron star. Prior to the formation of the neutron star the gravitational forces resisted by the star could be well described by Newtonian gravity. However, at the density of neutron stars it is necessary to include effects from general relativity.

The allowed masses and radii of (isothermal, non-rotating, with negligible magnetic field) neutron stars for any given EOS can be found using the Tolman-Oppenheimer-Volkoff (TOV) equations [13, 27, 28]:

$$
\begin{aligned}
\frac{dP(r)}{dr} &= -G\frac{[\epsilon(r)+P(r)]\,[M(r)+4\pi r^3 P(r)]}{r^2\left[1-\frac{2GM(r)}{r}\right]}, \\
\frac{dM(r)}{dr} &= 4\pi\epsilon(r)r^2
\end{aligned}
\tag{2.2}
$$

with the EOS relating the pressure, P, and energy density, ϵ, to close the system of equations, and M is the gravitational mass of the star within a radius, r.

This relationship between mass and radius being directly mediated by the EOS means that measurement of a single neutron star's mass and radius results in another constraint on the EOS of nuclear matter. Measurements of neutron star masses can be accomplished in more than one way; in the case of [15], measurement of the Shapiro delay is used. Measurement of the radius of neutron stars has traditionally been more difficult than mass measurements, but recent work has made significant advancements using thermal emissions of x-rays from the surface of neutron stars [29].

The measurement of gravitational waves from mergers of neutron stars is a very new, but also potentially very powerful measurement of neutron star structure. At its most basic, the inspiral phase of a merger provides information about the masses of the neutron stars involved. During this phase of the merger the two stars are only interacting gravitationally, and so no information other than their masses can be gained. As the stars approach one another close enough to affect each other tidally, the signal from the gravitational waves is affected by how easily deformed the stars are, giving useful information in the form of the tidal deformability parameter, Λ. This information can be combined with measurements of pulsar masses to gain further insights into the dense matter equation of state [29]. After the collision of the neutron stars, the new object is still emitting gravitational waves while settling into its new stable configuration. At later times in the merger, the frequency of the gravitational waves increases and the signal strength decreases, so that at late times, such as post merger, it is very difficult for current detectors to measure the signal, as seen in figure 2. Any future measurements of the post merger gravitational waves will be of immense importance to determining the dense matter EOS.

2.2. Non-relativistic nuclear potentials

One method for including nucleon-nucleon interactions within a model of nuclear matter is the use of an effective nuclear potential. One of the first examples comes from [30]. Due to the high densities encountered in nuclear matter like neutron stars, the many-body effects from strong interactions between nucleons is impossible to exactly calculate in all situations. Instead, an effective potential model can be developed which can be fit to empirical properties of nuclear matter at nuclear saturation density, $n_0 = 0.16\ \mathrm{fm}^{-3}$, and to the properties of neutron matter which can be calculated in ab initio many-body theory. The properties of nuclear matter come from scattering experiments and measurements of nuclei structure. Since the data with non-zero proton fraction comes from nuclei, this only explores a small region of density-temperature space for nuclear interactions around nuclear density. This results in a model which is able to accurately capture information about nuclear matter around nuclear saturation density and up to two to three times nuclear saturation density. At higher densities it is likely that relativistic effects become more important [13].

One non-relativistic nuclear potential is given in [31] which I will describe here. The parameters we use for this model are called NRAPR and the same model is used later in section 3.2 when constructing equations of state which include pions.

The nucleon contribution to the energy density is given by

$$\begin{aligned}\mathcal{E}_N(n_n, n_p, T) = {} & \frac{\tau_n}{2m_n} + \frac{\tau_p}{2m_p} \\ & + n_B(\tau_n + \tau_p)\left[\frac{t_1}{4}\left(1 + \frac{x_1}{2}\right) + \frac{t_2}{4}\left(1 + \frac{x_2}{2}\right)\right] \\ & + (\tau_n n_n + \tau_p n_p)\left[\frac{t_2}{4}\left(\frac{1}{2} + x_2\right) - \frac{t_1}{4}\left(\frac{1}{2} + x_1\right)\right] \\ & + \frac{t_0}{2}\left[\left(1 + \frac{x_0}{2}\right) n_B^2 - \left(\frac{1}{2} + x_0\right)(n_n^2 + n_p^2)\right] \\ & + \frac{t_3}{12}\left[\left(1 + \frac{x_3}{2}\right) n_B^2 - \left(\frac{1}{2} + x_3\right)(n_n^2 + n_p^2)\right] n_B^{\epsilon}] \,,\end{aligned} \tag{2.3}$$

where $t_0, t_1, t_2, t_3, x_0, x_1, x_2, x_3$, and ϵ are the Skyrme parameters taken from Ref. [31]. The neutron and proton densities are denoted by n_n and n_p, respectively, and $n_B = n_n + n_p$ is the total baryon density. The variables τ_n and τ_p are defined such that the first two terms in Eq. 2.3 correspond to the neutron and proton kinetic energy densities, respectively. In the investigation that follows we restrict ourselves to zero temperature for simplicity.

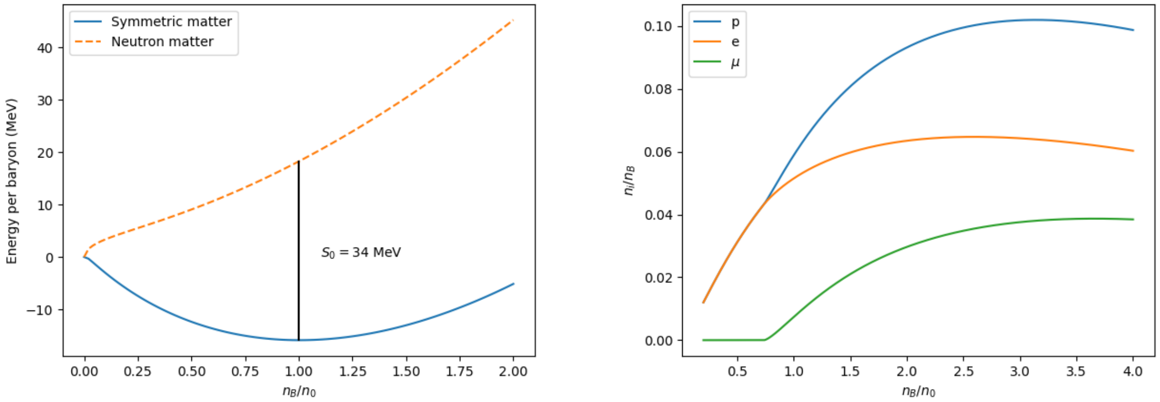

FIG. 4. *Left*: The energy per baryon using the NRAPR model for neutron matter and symmetric nuclear matter. The difference between the two is called the symmetry energy, $S(n_B)$. This model fits the value of the symmetry energy at nuclear density to be close to the measured value. *Right*: Particle fractions for protons, electrons and muons using the NRAPR model in charge neutral, beta equilibrated matter. The neutron fraction is much larger than those shown here and so is omitted for clarity. The neutron fraction is equal to one minus the proton fraction by definition.

One of the simplest quantities to which a nuclear potential can be fit is the symmetry energy at nuclear saturation density, S_0. Its value has been measured to be about 32 MeV [13]. The value of S_0 that a potential predicts is given by the difference between the energy per baryon of pure neutron matter and the energy per baryon of symmetric matter, with equal numbers of protons and neutrons. Each of these is easily obtained from Eq. 2.3 since it is a function of the proton and neutron densities. The left plot in figure 4 shows the energy per baryon of nuclear matter and symmetric matter for the NRAPR EOS. The plot also indicates the value which is obtained for S_0 from this EOS which was used to construct its parameter set.

Understanding the composition of matter in terms of particle fractions is vital to understanding a given equation of state. In order to determine the composition of matter we will need to use the fact that a given compact object like a neutron star should be charge neutral, so the total particle fraction of positive charge should equal the total fraction of negative charge. Electrically neutral, dense stellar matter will contain a high density of electrons and, at higher densities, muons as well. The large chemical potential for electrons and muons in this matter will suppress their positive counterparts. Since electrons and muons don't interact with the nucleons through strong interactions, they can be assumed to be free

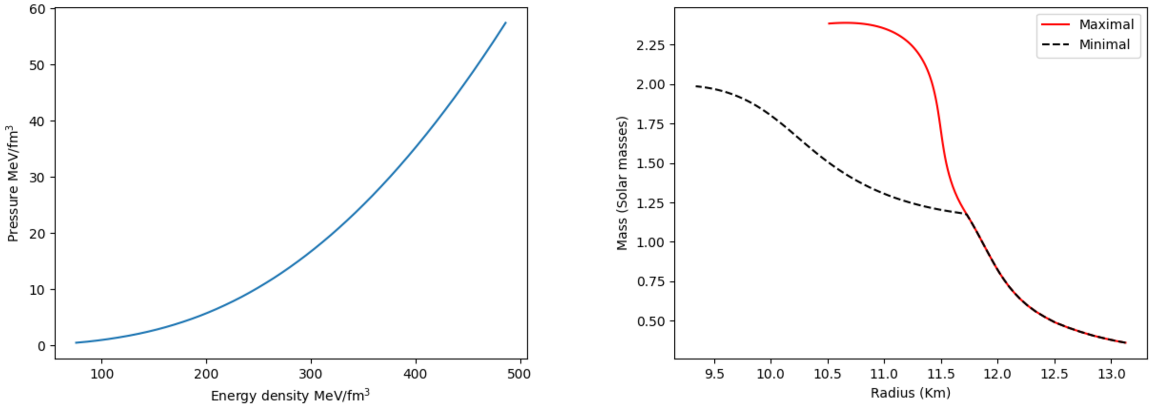

FIG. 5. *Left*: The total pressure for the NRAPR model in charge-neutral matter containing neutrons, protons, electrons, and muons with beta equilibrium enforced. *Right*: The mass radius curve for the NRAPR equation of state within the same type of matter. At low density the BPS equation of state [32, 33] is used. From half nuclear density up to three times nuclear density the NRAPR equation of state is used. This combined equation of state is shown in the mass radius plot as the dashed red and black line. The maximally stiff extension to the EOS is shown in solid red and the minimally stiff extension is shown by the dashed black line. All allowed extensions to the NRAPR EOS should lie between these two lines.

particles to a good approximation. We can obtain chemical potentials for the neutron and proton from Eq. 2.3 through derivatives with respect to the neutron and proton densities respectively.

$$\mu_n = \frac{\partial \mathcal{E}_N}{\partial n_n} \tag{2.4}$$

$$\mu_p = \frac{\partial \mathcal{E}_N}{\partial n_p} \tag{2.5}$$

As we are currently interested in the composition of matter in equilibrium, we can assume beta equilibrium is satisfied to find the chemical potentials for electrons and muons, $\mu_n - \mu_p = \mu_e = \mu_\mu$. An iterative procedure of guessing a proton fraction and solving for the densities of the electrons and muons can be used in order to find the proper proton fraction to satisfy charge neutrality. Applying this procedure, we find the right plot in figure 4 showing the composition of protons, electrons, and muons as a function of density using the NRAPR EOS. A slightly more complex version of this procedure, used to include pions, is outlined in appendix A.

One of the most often discussed and most useful data sets for a given EOS, to the point that the term "equation of state" is sometimes synonymous with it, is a plot of pressure vs the energy density. Given our stated assumption of zero temperature, the pressure of the system can be calculated from the energy density and our previously calculated chemical potentials and particle densities.

$$P = -(\mathcal{E} - \sum_i \mu_i n_i) \tag{2.6}$$

Where $\mathcal{E}$ is the total energy density, including electrons and muons, and the sum is to be performed over all the particle types in the system. The left plot in figure 5 shows the pressure as a function of the total energy density for the NRAPR EOS.

Finally, one of the most relevant measures of an EOS in relation to neutron stars is a plot of the predicted mass of a star vs its radius. More information and details of this calculation can be found in section 2.1. The right plot in figure 5 shows mass radius information relevant to the NRAPR EOS. Below half nuclear density the BPS equation of state [32, 33] is used. This is because at these low densities the uniform nuclear matter assumption made for nuclear potential equations of state is not a good approximation. From half nuclear density up to three times nuclear density, the NRAPR equation of state is used. This combined equation of state is shown in the mass-radius plot as the dashed red and black line. In order to construct the mass radius plot the equation of state must extend to higher densities, two possible extensions to the equation of state are shown, one as the solid red line and the other as the dashed black line, the maximally stiff equation of state and the minimally stiff equation of state, respectively. The maximally stiff line is constructed by switching to an EOS which has a speed of sound equal to the speed of light at densities above three times nuclear density. The minimally stiff line is constructed by switching to an EOS which has zero speed of sound above three times nuclear density, while changing the speed of sound to equal the speed of light at the highest energy density which will support observations of two solar mass neutron stars. All allowed extensions to the NRAPR EOS should lie between these two lines.

2.3. Relativistic mean field theory models

At densities above $4n_0$, the Fermi momentum and effective mass of the nucleons is expected to be on the order of 500 MeV, so a relativistic model is preferred [25]. Relativistic mean field (RMF) theories model the strong interactions between nucleons as exchanges of mesons. The most basic RMF theory is the $\sigma - \omega$ model, in which there are only two mesons which mediate the force between nucleons. This model is outlined in detail in Ch. 4 of [2]. More advanced models add a ρ-meson to the model as well, which differentiates the neutrons and protons. Note that while the mesons in the theory take inspiration from their real world counterparts, their masses and couplings are changed to fit nuclear interactions.

Here I will outline a simple RMF theory called the NL3 model whose Lagrangian is given by

$$\begin{aligned}\mathcal{L}_{\text{RMF}} =& \bar{N}(i\gamma^\mu\partial_\mu - g_\omega\gamma^\mu\omega_\mu - g_\rho\gamma^\mu\vec{b}_\mu\cdot\vec{\tau} - M + g_\sigma\sigma)N \\ & \frac{1}{2}\partial_\mu\sigma\partial^\mu\sigma - \frac{1}{2}m_\sigma^2\sigma^2 - U(\sigma) - \frac{1}{4}F_{\mu\nu}F^{\mu\nu} + \frac{1}{2}m_\omega^2\omega_\mu\omega^\mu - \frac{1}{4}\vec{B}_{\mu\nu}\cdot\vec{B}^{\mu\nu} + \frac{1}{2}m_\rho^2\vec{b}_\mu\cdot\vec{b}^\mu\end{aligned} \tag{2.7}$$

The ρ-meson field is denoted by $\vec{b}_\mu$, $\vec{\tau}$ is the is the isospin operator that acts on the nucleons, and the field strength tensors for the vector mesons are given by the usual expressions $F_{\mu\nu} = \partial_\mu\omega_\nu - \partial_\nu\omega_\mu$, $\vec{B}_{\mu\nu} = \partial_\mu\vec{b}_\nu - \partial_\nu\vec{b}_\mu$. N is the isospin doublet of protons and neutrons with the mass of both particles set to $M = 939$ MeV. The scalar self couplings are included in the function

$$U(\sigma) = \frac{\kappa}{3!}(g_\sigma\sigma)^3 + \frac{\lambda}{4!}(g_\sigma\sigma)^4 \tag{2.8}$$

For the NL3 model, the meson masses, couplings, and other fitting parameters are given by $m_\sigma = 508.194$ MeV, $m_\omega = 782.501$ MeV, $m_\rho = 763.000$ MeV, $g_\sigma^2 = 104.3871$, $g_\omega^2 = 165.5854$, $g_\rho^2 = 79.6000$, $\kappa = 3.8599$ MeV, and $\lambda = -0.01591$.

We are interested in static uniform matter in its ground state, so we approximate the meson fields by their mean values in this state: $\sigma \rightarrow <\sigma>$, $\omega_\mu \rightarrow <\omega_\mu>$, and $\vec{b}_\mu \rightarrow <\vec{b}_\mu>$. This is known as the relativistic mean-field approximation [2]. For convenience of notation, we leave off the angle brackets and keep in mind that the meson fields are replaced by their mean values. In addition to this, we use the simplifying assumption that the vector mesons have only a time-like component, leaving only σ, ω_0, and the third component of the rho meson's time-like component, b_0.

Using the given assumptions, we can finding the self-energies of the nucleons by diagonalizing the corresponding Hamiltonian. One can show that the nucleon effective mass is given by $M^* = M - g_\sigma \sigma$ with $E^* = \sqrt{k^2 + M^{*2}}$. In addition, the chemical potentials, μ_N, can be found from the effective chemical potentials, υ_N, by

$$\mu_N = \upsilon_N + g_\omega \omega_0 + g_\rho \tau_{3N} b_0 \tag{2.9}$$

Where the third component of isospin for protons will be 1/2 and for neutrons will be $-1/2$.

In order to use this model, we will need to find the values for the meson fields. We can use the Euler-Lagrange equations for each of the remaining meson fields to find their equations of motion. Using our assumptions, the simplified Euler-Lagrange equations are given by

$$\begin{aligned} m_\omega^2 \omega_0 &= g_\omega (n_p + n_n) \\ m_\rho^2 b_0 &= g_\rho \frac{n_p - n_n}{2} \\ m_\sigma^2 \sigma &= -\frac{\partial U(\sigma)}{\partial \sigma} + g_\sigma (n_p^s + n_n^s) \end{aligned} \tag{2.10}$$

Where the nucleons' number density, n_N, and scalar density, n_N^s, are given in terms of their distribution functions, $f(E_N^*)$, by

$$n_N = 2 \int \frac{d^3k}{(2\pi)^3} f(E_N^*) \tag{2.11}$$

$$n_N^s = 2 \int \frac{d^3k}{(2\pi)^3} \frac{M^*}{E_N^*} f(E_N^*) \tag{2.12}$$

In the zero-temperature matter we consider below, the nucleons are fully degenerate, so their distribution function is given by the Heaviside step function, $H(\upsilon_N - E_N^*)$.

The equations of motion in Eq. 2.10 can be solved in a straightforward way. Given values for the effective chemical potentials, υ_n and υ_p, the only unknown quantity in the third equation of motion is the meson field σ. After solving for σ, the nucleon densities are known and thus the other two equations of motion can be solved for the remaining meson fields.

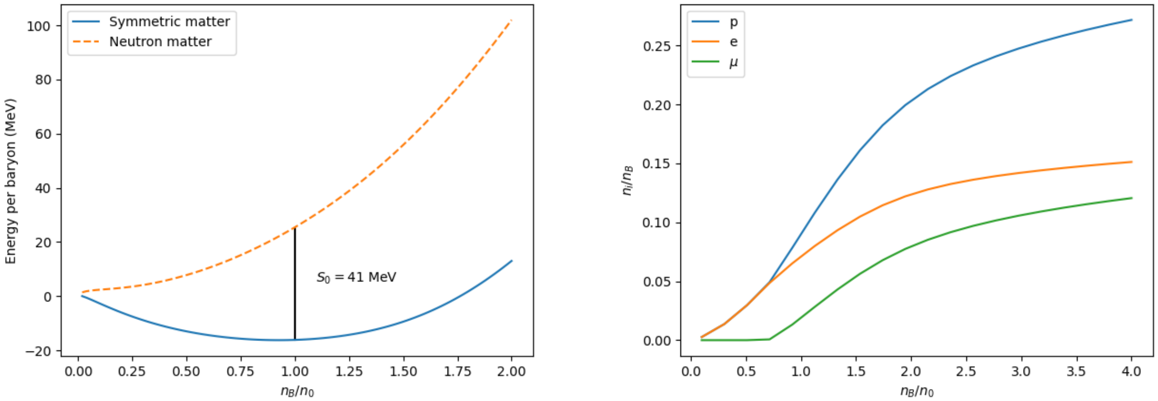

FIG. 6. *Left*: The energy per baryon using the NL3 model for neutron matter and symmetric nuclear matter. The difference between the two is called the symmetry energy, $S(n_B)$. The value for the symmetry energy at nuclear density in this model is shown. *Right*: Particle fractions for protons, electrons and muons using the NL3 model in charge neutral, beta equilibrated matter. The neutron fraction is much larger than those shown here and for clarity. The neutron fraction is equal to one minus the proton fraction by definition.

As can be seen in the left plot of figure 6, this model for nuclear matter includes a larger symmetry energy than the NRAPR potential model described in the previous section. The larger symmetry energy leads to a larger charge chemical potential, increasing the presence of electrons and muons and, since the matter is charge neutral, protons as well which can be seen in the composition plot on the right side of figure 6.

The large symmetry energy of this EOS has strong effects on both the pressure and mass-radius curves which are shown in in figure 7. The pressure increases much more rapidly with increasing energy density due to the large symmetry energy, which can be described as a more “stiff” EOS. The high pressure means that the EOS can support much higher masses of neutron stars.

3. PIONS IN HOT DENSE MATTER

Pions are the lightest meson due to being approximate Goldstone modes. Thus, negative pions might be expected to be relatively common in dense nuclear matter, appearing in

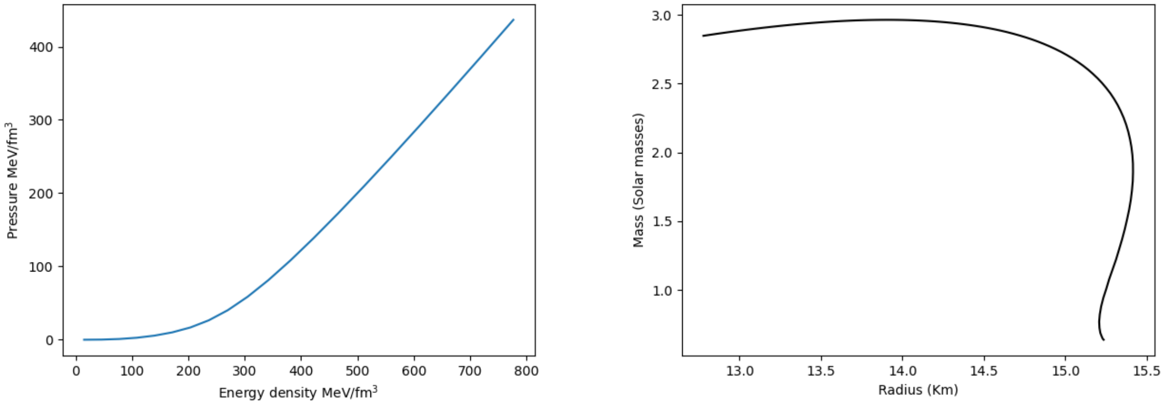

FIG. 7. *Left*: The total pressure for the NL3 model in charge neutral matter containing neutrons, protons, electrons, and muons with beta equilibrium enforced. *Right*: The mass radius curve for the NL3 equation of state within the same type of matter. At low density the BPS equation of state [32, 33] is used. Above half nuclear density the NL3 equation of state is used.

similar proportion to muons as they are both enhanced by the negative charge chemical potential and have similar masses. In addition to this, pions are bosons and so have the possibility of forming a condensate. Unlike electrons and muons, pions interact with the strong force and cannot be approximated as being free particles in nuclear matter. This creates large uncertainties in calculations of pion number density and the critical density for condensation.

During supernova, peak temperatures reach 30 MeV and the electron chemical potential exceeds the muon rest mass. In these conditions the thermal population of muons can play a significant role [1]. Similarly, while the thermal population of negatively charged pions may not be significant, it is enhanced through an attractive interaction with neutrons [34], which allows for a population of pions to be larger than the population of muons under the same conditions [26].

If there were a significant quantity of negatively charged pions in the medium we would expect their charge to be canceled by an increased proton fraction which in turn creates a softer EOS.

3.1. History of bosons in hot dense matter

Most historical considerations of pions in neutron star matter have been concerned with whether or not a condensed phase of pions will form at high density [35–41]. The complicating factor in this calculation, and the reason the answer is still up for debate, is the complex nature of the pion-nucleon interaction which is sensitive to nuclear many-body effects that are difficult to calculate reliably at high density. A further complication comes from pion condensation being driven by a p-wave interaction with nucleons, meaning a condensate of pions would likely form at finite momentum. This has led to the consideration that kaon condensation may be more likely due to a larger number of attractive interactions with nucleons [42, 43]. However, the expected density threshold would naively be higher due to their larger mass. This is because the formation of a condensate requires the chemical potential of the particle to surpass the minimum energy of the particle, and a higher mass will usually imply a higher minimum energy.

Many effects of a pion or kaon condensate would be largely similar. The charge chemical potential in neutron stars will favor negative particles and suppress positive particles, meaning any condensate that forms is likely to be negatively charged. After the formation of a negative condensate, one can expect an increase in the proton fraction to maintain an overall neutral charge. In the extreme case, it may also be favorable for positrons to exist in the core with the condensate. The increase in proton fraction comes with a commensurate softening of the nuclear EOS. In addition to these effects, with the formation of a pion condensate one can expect an increase in neutrino cooling of neutron stars. This is because in the presence of sufficient numbers of pions, the reaction $n\pi^- \to ne^-\nu_e$ proceeds much more rapidly than the modified Urca reaction, which is thought to be the dominant process for cooling newly formed neutron stars. The number of free pions is likely not sufficient to facilitate the reaction, but in the presence of a pion condensate the pions in the condensed phase can serve the same role. A similar effect should be expected from a kaon condensate [44].

Calculations from first principles of the pion and kaon self-energies have been done [45] and provide evidence for or against condensation of each; but the strength of the interaction between these mesons and the eponymous nucleons of nuclear matter make the perturbation calculations difficult to compute to a high enough order to give a definitive answer.

Another possibility is EOS calculations within a mean field model. Within [42, 43] the authors discuss the possibility of a kaon condensate and estimate the condensation density using a simplified mean field model. This method is described in more detail in the following section.

There are a few ways in which we can try to experimentally answer the question of whether or not a meson condensate exists in nuclear matter. Measurements of distant neutron stars can reveal more information about the nuclear matter EOS, but these measurements are limited by a deficiency of observable neutron stars in addition to the limited information about the EOS presented by these measurements. See section 2.1 for a description of the relation between measurements of neutron stars and the EOS. New ways of directly measuring the EOS of neutron stars are still being developed, such as analysis of late time inspiral signals from neutron star mergers. Much more controllable experimental measurements can be done on nuclear matter that exists on earth in the form of nuclei, however the amount these measurements can tell us about the EOS of neutron stars is limited by the fact that stable nuclei tend to have similar numbers of neutron and protons rather than the excess of neutrons found in neutron stars.

3.1.1. A model for pion condensation

In references [42] and [43], Kaplan and Nelson propose a simple model for s-wave kaon condensation at zero temperature and find that one can expect a charged kaon condensate at several times nuclear saturation density. Additionally, this model is thoroughly analyzed in [46] with respect to the kaon condensate's effect on neutron stars. In this section I preform a similar, but simplified, calculation for pion condensation. Since pions have strong p-wave interactions it is unclear if a p-wave or s-wave condensate is more likely to form, but we perform a more detailed analysis of s-wave pion condensation in section 6 so it is useful to detail a simpler calculation of an s-wave pion condensate here. This calculation differs from that of [42, 43, 46] in that it uses a $SU(2)$ model, but the methods are very similar; once the Lagrangian is simplified into a form depending only on the condensate amplitude, θ, the calculations are almost identical.

We begin with a very simple Lagrangian containing terms for pions from chiral perturbation theory as well as the strongest interaction term between pions and nucleons, in addition to the kinetic and mass contributions of the nucleons themselves.

$$\mathcal{L}_\pi = \frac{f_\pi^2}{4} \langle \partial_\mu U \partial^\mu U^\dagger + \chi_+ \rangle + \bar{N}(i(\not{\partial} + \not{V}) - M)N \tag{3.1}$$

Since we do not consider neutral pions, we can write the mass contribution as $\chi_+ = m_\pi^2(U + U^\dagger)$. The symbol $\langle \cdot \rangle$ denotes a trace over flavor degrees of freedom. U is the exponential of the matrix of pion fields given by

$$U = \exp\left(\frac{i}{f}\begin{bmatrix} \pi^0 & \sqrt{2}\pi^+ \\ \sqrt{2}\pi^- & -\pi_0 \end{bmatrix}\right), \tag{3.2}$$

The nucleons are represented by the isospin vector $N = \begin{pmatrix} p \\ n \end{pmatrix}$. The interacting term of the Lagrangian is given by

$$V_\mu = \frac{1}{2}[\xi^\dagger, \partial_\mu \xi] \tag{3.3}$$

Where $\xi = \sqrt{U}$.

At this point we will make the assumption that the charge pion condensate can be approximated by a spatially uniform classical field in the mean field approximation

$$\langle \pi^- \rangle = \langle \pi^+ \rangle^\dagger = \frac{f_\pi}{\sqrt{2}}\theta e^{-i\hat{\mu}t}, \tag{3.4}$$

where the amplitude is parameterized in terms of θ for convenience of future notation. At this point it is convenient to simplify each of the terms in the Lagrangian in terms of this assumption.

$$\begin{aligned} U &= \cos(\theta) + i\sin(\theta)\begin{bmatrix} 0 & e^{i\hat{\mu}t} \\ e^{-i\hat{\mu}t} & 0 \end{bmatrix} \\ \langle \chi_+ \rangle &= 4m_\pi^2 \cos(\theta) \\ V_\mu &= -i\hat{\mu}\delta_{\mu 0}\sin^2\left(\frac{\theta}{2}\right)\begin{bmatrix} 1 & 0 \\ 0 & -1 \end{bmatrix} \end{aligned} \tag{3.5}$$

The newly simplified Lagrangian can be written as

$$\mathcal{L}_\pi = \frac{f_\pi^2}{2}\hat{\mu}^2 \sin^2(\theta) - 2f_\pi^2 m_\pi^2 \sin^2\left(\frac{\theta}{2}\right) + \bar{N}((i\partial\!\!\!/ - M) + \gamma^0 M_1)N \tag{3.6}$$

Where M_1 is defined by

$$M_1 \equiv \hat{\mu}\sin^2\left(\frac{\theta}{2}\right)\begin{bmatrix} 1 & 0 \\ 0 & -1 \end{bmatrix} \tag{3.7}$$

Our goal now will be to compute the free energy of the system which can then be minimized in order to find the ground state. Using the Lagrangian, we can find the Hamiltonian by the Legendre transformation,

$$H = \sum_q p_q \dot{q} - L \tag{3.8}$$

where the sum is over each of the fields and the momentum conjugates are given by $p_q = \frac{\partial \mathcal{L}}{\partial \dot{q}}$. Before computing the Hamiltonian, we couple the system to the electric charge through the $\hat{\mu}$ chemical potential, which allows us to construct a charge neutral ground state

$$H' = H + \hat{\mu}(n_p - n_e - n_\mu - n_\pi) \tag{3.9}$$

While not immediately obvious, this expression can be simplified greatly such that the computation of the momentum conjugates of the pion fields is not necessary. Using Noether's theorem, the charge density of the pions can be found to be $i(p_{\pi^+}\pi^+ - p_{\pi^-}\pi^-)$. Due to the assumption that the pion fields have only time dependence, the pion terms from the Legendre transform exactly cancel the $\hat{\mu}n_\pi$ term.

$$p_{\pi^+}\dot{\pi}^+ + p_{\pi^-}\dot{\pi}^- = i\hat{\mu}(p_{\pi^+}\pi^+ - p_{\pi^-}\pi^-) = \hat{\mu}n_\pi \tag{3.10}$$

The remaining expression for H' can be evaluated, and by including the lepton energies one finds

$$H' = \bar{N}\left[(-i\vec{\gamma}\cdot\vec{\nabla} + M) - \gamma^0 M_1\right] - \frac{f_\pi^2}{2}\hat{\mu}^2\sin^2(\theta) + 2f_\pi^2 m_\pi^2 \sin^2\left(\frac{\theta}{2}\right) + H_e - \hat{\mu}n_e + H_\mu - \hat{\mu}n_\mu \tag{3.11}$$

By assuming the nucleons are non-relativistic and diagonalizing H' we can find the single-particle energies for the neutron and proton are given by

$$\begin{aligned}\epsilon_n &= M + \frac{p^2}{2M} + \mu \sin^2\left(\frac{\theta}{2}\right) \\ \epsilon_p &= M + \frac{p^2}{2M} + \mu - \mu \sin^2\left(\frac{\theta}{2}\right)\end{aligned} \tag{3.12}$$

To construct a state of fixed baryon number, we occupy the neutron and proton energy states up to their Fermi momentum: p_{Fn} and p_{Fp}, respectively. Since only the kinetic term is dependent on momentum, the other terms will end up proportional to the neutron and proton densities due to the phase space integrals. To make the calculation more general, and to include nucleon interactions, we replace the nucleon energy terms by $\epsilon_B(n_n, n_p)$, which can be replaced by a non-relativistic model for the nucleon energy given through a potential model. The final free energy density is given by

$$\Omega = \epsilon_B(n_n, n_p) + \hat{\mu} n_p + \hat{\mu}(n_n - n_p)\sin^2\left(\frac{\theta}{2}\right) - \frac{f_\pi^2}{2}\hat{\mu}^2 \sin^2(\theta) + 2 f_\pi^2 m_\pi^2 \sin^2\left(\frac{\theta}{2}\right) + \Omega_e + \Omega_\mu \tag{3.13}$$

Where Ω_e and Ω_μ are the contributions from the filled Fermi sea of leptons.

It is useful to rewrite Ω in terms of the convenient parameters $u = n_B/n_0$, $x = n_p/n_B$, where n_0 is nuclear saturation density and x is just the fraction of protons within the full baryon number.

$$\Omega = \epsilon_B(u, x) + u n_0 \hat{\mu} x + u n_0 \hat{\mu}(1 - 2x)\sin^2\left(\frac{\theta}{2}\right) - \frac{f_\pi^2}{2}\hat{\mu}^2 \sin^2(\theta) + 2 f_\pi^2 m_\pi^2 \sin^2\left(\frac{\theta}{2}\right) + \Omega_e + \Omega_\mu \tag{3.14}$$

At this point we can determine the ground state of the system at a fixed value of baryon density by extremizing Ω with respect to x, $\hat{\mu}$, and θ.

$$\frac{\partial \Omega}{\partial x} = 0, \frac{\partial \Omega}{\partial \theta} = 0, \frac{\partial \Omega}{\partial \hat{\mu}} = 0 \tag{3.15}$$

Given a nuclear energy density which can be expressed in terms of a nuclear symmetry energy, $S(u)$, as

$\epsilon(u, x) \approx \epsilon(u, x = 1/2) + S(u)(1 - 2x)^2$, the extremized equations can be written as

$$\mu = \frac{4(1-2x)S(u)}{\cos\theta} \tag{3.16}$$

$$0 = un_0x - \left(\frac{\hat{\mu}^3}{3\pi^2} + \eta(|\hat{\mu}| - m_\mu)\frac{(\hat{\mu}^2 - m_\mu^2)^{3/2}}{3\pi^2} + f_\pi^2\hat{\mu}\sin^2(\theta) - un_0(1-2x)\sin^2\left(\frac{\theta}{2}\right)\right) \tag{3.17}$$

$$\cos(\theta) = \frac{f_\pi^2 m_\pi^2 + un_0\frac{\hat{\mu}}{2}(1-2x)}{f_\pi^2\hat{\mu}^2} \tag{3.18}$$

The second equation comes from the derivative with respect to $\hat{\mu}$ and is just an expression of charge neutrality, where $\eta(|\hat{\mu}| - m_\mu)$ is the Heaviside function which comes with the muon density (the electrons are approximated as massless) and the pion density can be inferred to be $n_\pi = f_\pi^2\hat{\mu}\sin^2(\theta) - un_0(1-2x)\sin^2\left(\frac{\theta}{2}\right)$.

The final equation comes from the derivative with respect to θ and is the solution for conditions where a condensate exists. Without a pion condensate, the solution to $\partial\Omega/\partial\hat{\mu} = 0$ is just $\theta = 0$.

By setting $\theta = 0$ and solving all three of these equations, it is possible to determine the critical density of pion condensation. Additionally, at values of u above this density, the values of x, $\hat{\mu}$, and θ are found by solving this same set of equations.

3.2. Virial expansion

Systems of ideal particles with no interactions can be easily modeled, but when interactions are included, modeling the system accurately becomes more difficult. The virial expansion expands the partition function into powers of density, with each term being a correction to the ideal equation of state for a system of particles.

At the temperatures of interest, in the range 10 − 50 MeV, the matter is composed of nucleons, leptons and pions. To include the effects of interactions between pions and nucleons, we calculate the second-virial coefficient for the pion-nucleon system directly in terms of the measured pion-nucleon phase shifts. This approach was used to describe the hot hadronic gas encountered in heavy-ion collisions in Ref. [47–49], and to describe a dilute gas of nucleons encountered in outer regions of the newly born neutron star in Ref. [50]. The virial expansion provides a systematic approach to calculate the thermodynamic properties of interacting multi-component gases when the particle fugacities are small. The fugacity of a particle species i is given by $z_i = \exp\beta(\mu_i - m_i)$ where μ_i is the chemical potential which includes mass, m_i is the rest mass of the particle, $\beta = 1/T$ is the inverse temperature. To justify the use of the virial expansion, we restrict our analysis to densities that are low enough, and temperatures that are high enough, to ensure that the fugacity $z_{\pi^-} < 1$ and that Bose-Einstein condensation of pions does not occur.

At the modest densities that we consider, $\rho \lesssim 3 \times 10^{14}$ g/cm^3, it is adequate, as a first step, to account for interactions between nucleons using a simple non-relativistic Skyrme model [30]. The parameters of the model we employ, called NRAPR, are obtained by fitting to the empirical properties of nuclear matter at nuclear saturation density $n_0 = 0.16$ fm^{-3} [31, 51], and to the properties of neutron matter predicted by ab initio many-body theory which employ realistic nuclear interactions [52, 53]. The nucleon contribution to the energy density is given by

$$\begin{aligned}
\mathcal{E}_N(n_n, n_p, T) &= \frac{\tau_n}{2m_n} + \frac{\tau_p}{2m_p} \\
&+ n_B(\tau_n + \tau_p)\left[\frac{t_1}{4}\left(1 + \frac{x_1}{2}\right) + \frac{t_2}{4}\left(1 + \frac{x_2}{2}\right)\right] \\
&+ (\tau_n n_n + \tau_p n_p)\left[\frac{t_2}{4}\left(\frac{1}{2} + x_2\right) - \frac{t_1}{4}\left(\frac{1}{2} + x_1\right)\right] \\
&+ \frac{t_0}{2}\left[\left(1 + \frac{x_0}{2}\right) n_B^2 - \left(\frac{1}{2} + x_0\right)(n_n^2 + n_p^2)\right] \\
&+ \frac{t_3}{12}\left[\left(1 + \frac{x_3}{2}\right) n_B^2 - \left(\frac{1}{2} + x_3\right)(n_n^2 + n_p^2)\right] n_B^{\epsilon}]\,,
\end{aligned} \tag{3.19}$$

where $t_0, t_1, t_2, t_3, x_0, x_1, x_2, x_3$, and ϵ are the Skyrme parameters taken from Ref. [31]. The neutron and proton densities are denoted by n_n and n_p, respectively, and $n_B = n_n + n_p$ is the total baryon density. The variables τ_n and τ_p are defined such that the first two terms in Eq. 3.19 correspond to the neutron and proton kinetic energy densities, respectively.

The dense matter we consider is homogeneous, electrically neutral, and close to beta equilibrium. Under these conditions, the chemical potential for negative charge $\hat{\mu} = \mu_n - \mu_p$ acts as a source for negatively charged particles. In beta equilibrium the electron, muon and pion chemical potentials are equal $\mu_e = \mu_{\mu}^{-} = \mu_{\pi^-} = \hat{\mu}$, and electric charge-neutrality requires that $n_p = n_e + n_\mu + n_{\pi^-}$. When $\hat{\mu} = \mu_n - \mu_p \gtrsim T$, it is reasonable to neglect the presence of π^0 and π^+ particles in the ground state since their density is suppressed by the factor $\exp(-\hat{\mu}/T)$ and $\exp(-2\hat{\mu}/T)$, respectively, relative to the abundance of π^-.

The second virial coefficient for the π^-−neutron system is given by

$$b_2^{n\pi^-} = \frac{e^{\beta M}}{2\pi^3}\int_M^\infty dE E^2 K_1(\beta E)\sum_{l,\nu}(2l+1)\delta_{l,\nu}^{3/2}\,, \tag{3.20}$$

where K_1 is the modified Bessel function of the second kind, and $M = m_N + m_\pi$ is the invariant mass of the interacting pair at the threshold. This result was obtained using the relativistic formalism in Ref. [47, 48] and is appropriate for our study because pions can be relativistic as their typical pion momenta $p_\pi \simeq \sqrt{3m_\pi T}$ is comparable to m_π. Note that the phase shifts δ are dependent on E which is the center-of-mass energy. The sum is over the angular momentum l of the scattering state and the nucleon spin-projections, $\nu = +, -$. Since $n\pi^-$ scattering only involves the isospin $I = 3/2$ state, only the pion-nucleon phase shift in the isospin $I = 3/2$ channel denoted by $\delta_{l,\nu}^{3/2}$ contributes to $b_2^{n\pi^-}$. We note that this definition differs from Ref. [47, 48] in that it contains an extra factor of $e^{\beta M}$. We find it convenient to include this factor and redefine the thermodynamic functions that appear later in the text.

Proton-π^- scattering involves two reaction channels: $\pi^- p \to \pi^- p$ and $\pi^- p \to \pi^0 n$, which implies these reactions do not have definite isospin. However, since b_2 is independent of the basis in which we consider the S matrix [54], $b_2^{p\pi^-}$ depends on the sum of the phase shifts from the two mixed isospin channels.

$$b_2^{p\pi^-} = \frac{e^{\beta M}}{2\pi^3}\int_M^\infty dE E^2 K_1(\beta E)\sum_{l,\nu}(2l+1)(\delta_{l,\nu}^{3/2} + \delta_{l,\nu}^{1/2})\,. \tag{3.21}$$

In this study we will only include $l = 0, 1$, i.e. the s-wave and p-wave contributions. At the energies of interest, we find them to be the dominant contributions. In Fig. 8 we show the s-wave and p-wave phase shifts taken from the analysis of experimental data in Ref. [55]. The phase shifts are plotted as a function of $E - M$ where $E = \sqrt{p^2 + m_\pi^2} + \sqrt{p^2 + m_N^2}$ is the center-of-mass energy and p is the magnitude of the pion and nucleon momenta in the center-of-mass frame. The large and attractive p-wave phase-shift $\delta_{+1}^{3/2}$ due to the Δ−resonance is the dominant channel. The second virial coefficients calculated using Eqns. 3.20 & 3.21 at a few temperatures of interest are shown in Table 1.

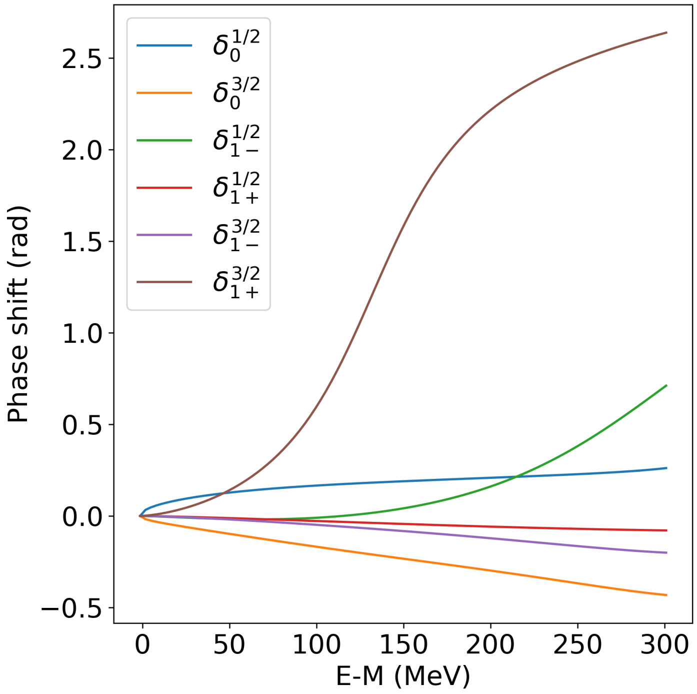

FIG. 8. Pion-nucleon phase shifts from the analysis presented in Ref. [55]

T (MeV)	15	30	45
$b_2^{n\pi^-}$ (fm^{-3})	2.14×10^{-4}	4.09×10^{-3}	1.87×10^{-2}
$b_2^{p\pi^-}$ (fm^{-3})	4.24×10^{-4}	4.68×10^{-3}	2.02×10^{-2}

TABLE II. The second-virial coefficients for the $N\pi^-$ system.

The virial expansion for nucleons fails at the higher density of interest here, and for this reason we use a simple mean-field model to include the effects of nucleon-nucleon interactions. While it is desirable to treat the nucleon-nucleon and nucleon-pion interactions consistently, and chiral perturbation theory provides in-principle a framework to do this, there remain technical challenges [56]. Further, the convergence of the chiral expansion for pion-nucleon interactions is poor and requires a large number of operators to capture the resonant nature of this interaction [57]. To circumvent these issues, as a first step in the study of the role of pions in hot dense matter, we advocate our hybrid approach. In the limit when $z_{\pi^-} \ll 1$, and $z_n, z_p \ll 1$ our approach is reliable. At higher density where the $z_{\pi^-} < 1/2$, and $z_n < 1$ or $z_p < 1$ we expect our results to capture the qualitative aspects, but corrections due to neglected terms proportional to $z_\pi z_n^2$ and $z_\pi z_p^2$ become important. These need to be assessed before one can draw quantitative conclusions. In this study, we also neglect pion-pion interactions because the pion-nucleon interaction, and the nucleon density, are both significantly larger.

The composition of matter at fixed temperature and baryon density is determined by requiring matter to be charge neutral and in beta-equilibrium, The chemical potentials μ_n, μ_p, and $\mu_e = \mu_{\mu^-} = \mu_{\pi^-} = \hat{\mu} = \mu_n - \mu_p$ are determined to ensure that $n_B = n_n + n_p$ and $n_{e^-} + n_{\mu^-} + n_{\pi^-} = n_p$. The effect of interactions is negligible for the leptons, and their number densities are obtained using the ideal Fermi gas result.

For nucleons and pions, interactions are important. The nucleon number densities are given by

$$n_i = \int \frac{dk}{\pi^2} k^2 (1 + \exp\left(\beta(\epsilon_i(k) - \mu_i)\right))^{-1} . \tag{3.22}$$

where the single nucleon energy

$$\epsilon_i(k) = m_i + \frac{k^2}{2m_i^*} + U_i(n_n, n_p, T) , \tag{3.23}$$

is obtained in mean field theory, m_i^* is the nucleon effective mass, and $U_i(n_n, n_p, T) = \partial \mathcal{E}_N(n_n, n_p, T)/\partial n_i$ is the mean field potential energy [30]. The effective mass is found by solving for the momentum-dependent part of the functional derivative of $\mathcal{E}_N(n_n, n_p, T)$ with respect to the nucleon distribution function. The momentum-independent part is equal to $U_i(n_n, n_p, T)$.

The number density of pions is obtained in the virial expansion, and is given by

$$n_{\pi^-} = \int \frac{dk}{2\pi^2} k^2 \exp\left(-\beta(\sqrt{k^2 + m_\pi^2} - \hat{\mu})\right) + n_{\pi^-}^{\text{int}} , \tag{3.24}$$

where

$$n_{\pi^-}^{\text{int}} = \sum_{N=n,p} z_N z_{\pi^-} b_2^{N\pi^-} , \tag{3.25}$$

is the contribution due to pion-nucleon interactions. Note that the reason we have used the Boltzmann distribution here for pions rather than the Bose-Einstein distribution is for consistency with the virial expansion. The difference this makes, however, is minimal with only a change of about 4 to 5 percent in the pion number density at nuclear density and $T = 30$ MeV. Eq. 3.22 only includes effects due to nucleon-nucleon interactions. The contributions due to pion-nucleon interactions, given by the virial expansion, are $\delta n_n =$

$z_n z_{\pi^-} b_2^{n\pi^-}$, and $\delta n_p = z_p z_{\pi^-} b_2^{p\pi^-}$, respectively. In our hybrid model, these contributions are added to Eq. 3.22 to obtain the total neutron and proton densities.

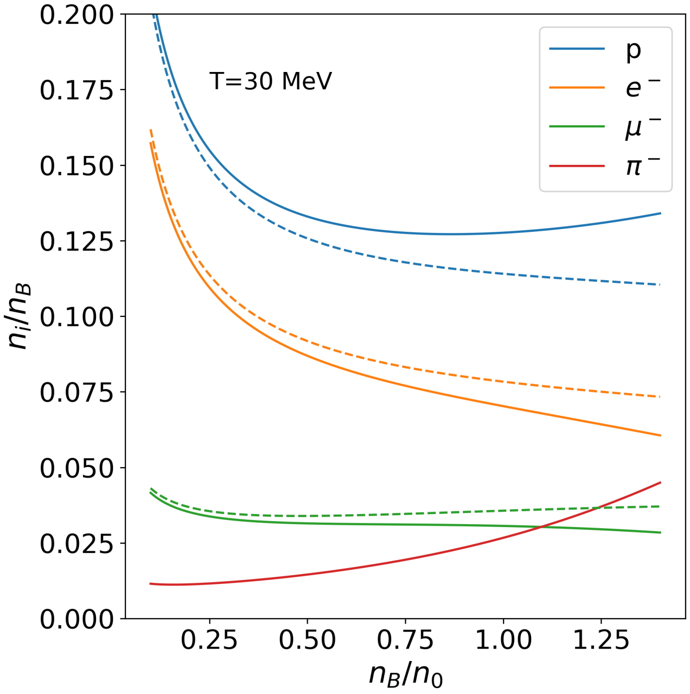

FIG. 9. Number fraction of charged particles at $T = 30$ MeV in β-equilibrium. Solid curves include pions and dashed curves only contain nucleons and leptons.

For a given value of the baryon density, n_B and temperature, T, we guess a value for proton number density, n_p, and use this to define the single particle nucleon energies defined in Eq. 3.23. Then, we use Eq. 3.22 to obtain the nucleon chemical potentials μ_n and μ_p. The beta equilibrium condition allows us to obtain the charge chemical potential μ_e and we use it to obtain the number densities of n_e, n_μ, n_π. The lepton number densities are obtained using the ideal Fermi-Dirac distribution, and the pion number density is obtained using Eq. 3.24. The charge neutrality condition $n_p = n_e + n_\mu + n_\pi$ allows us to update the guess n_p and find the true value. The above method is augmented slightly to include the change in the nucleon number densities due to the interactions between nucleons and pions. In this case we define two new variables

$$\eta_n = \frac{\mu_n - m_n - U_n}{T}\,, \quad \eta_p = \frac{\mu_p - m_p - U_p}{T}\,, \tag{3.26}$$

which we solve for in addition to n_p. These three variables are determined as a solution the system of three equations, given by $n_n = \tilde{n}_n + \delta n_n$, $n_p = \tilde{n}_p + \delta n_p$ and $n_p = n_e + n_\mu + n_\pi$, where $\tilde{n}_n$ and $\tilde{n}_p$ are given by Eq. 3.22.

The densities of charged particles with and without the inclusion of pions are shown in Fig. 9. From the figure it is evident that pions enhance the proton fraction and suppress the lepton fraction in the hot dense matter as they furnish additional negative charge. This effect is strong enough that at higher densities the proton fraction begins increasing with density due to the large number of pions. Although $m_\pi > m_\mu$, strong attractive p-wave interactions with nucleons enhance the pion number density, at $n_B = n_0$ and $T = 30$ MeV, $n_{\pi^-} \approx n_{\mu^-}$. A naive extrapolation suggests n_{π^-} increases rapidly with density, and $n_B = 1.4n_0$ and $T = 30$ MeV, $n_{\pi^-} \approx 2n_{\mu^-}$.

The fugacities of pions and nucleons at baryon density $n_B = n_0/2$ and $n_B = n_0$ as a function of the temperature are shown in Fig. 10. It is interesting to note that z_{π^-} and z_p

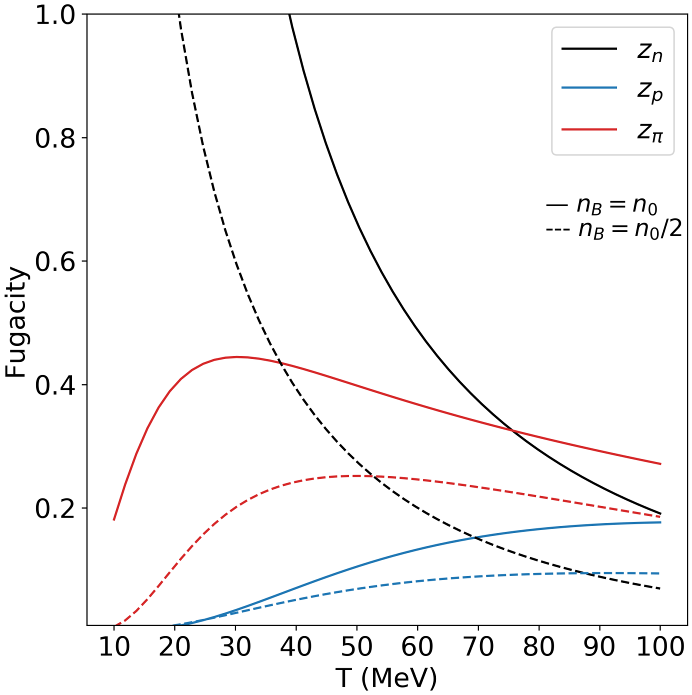

FIG. 10. Pion and nucleon fugacities in charge-neutral dense matter in β-equilibrium at $n_B = n_0$ (solid-curves) and $n_B = n_0/2$ (dashed-curves) are shown as function of temperature.

remain small over a wide range of temperatures. As expected in neutron-rich matter, the fugacity of neutrons is large, and the virial expansion for pion-neutron interactions is reliable only at high temperature. In the work that follows, we consider matter at $n_B < 1.5\ n_0$ and

$T > 25$ MeV and calculate the EOS and weak interaction rates using the hybrid model in which pion-nucleon interactions are accounted for through the second virial coefficient, and nuclear interactions are treated in mean field theory.

3.3. Pseudo-potential and pion self-energy

The dispersion relation for pions in dense matter is poorly understood due to nuclear many body effects; however, some general features are understood. Negative pions have a repulsive s-wave interaction with nucleons and a strong p-wave attraction due to the delta resonance. We can expect these features to manifest in the negative pions' dispersion relation: low momentum pions will obtain slightly higher energies than for equal momentum pions in vacuum, and high momentum pions will have much lower energy than their vacuum equivalent. Even though the pion dispersion relation is poorly understood we can use a simple model to calculate the real part of the pion self-energy using the one-loop approximation. [26]

The dispersion relation in this model is given by

$$E_{\pi^-}(p) = \sqrt{p^2 + m_\pi^2} + \Sigma_{\pi^-}(p)\,, \tag{3.27}$$

where $\Sigma_{\pi^-}(p)$ is the self-energy. Our model for the real part of $\Sigma_{\pi^-}(p)$ using the one-loop approximation is given by

$$\Sigma_{\pi^-}(p) = \int \frac{d^3k}{(2\pi)^3} \sum_{N=n,p} f_N(E_N(k))\; V^{ps}_{N\pi^-}(p_{cm})\,, \tag{3.28}$$

where the pion-nucleon interaction is directly proportional to the phase shifts

$$V^{(ps)}_{N\pi^-}(p_{\rm cm}) = -\sum_{I,l,\nu} \alpha_l (2l+1) \frac{2\pi \delta^I_{l,\nu}}{\bar{m}\; p_{\rm cm}}\,. \tag{3.29}$$

Here, $p_{\rm cm} = \bar{m}\sqrt{\frac{p^2}{m_\pi^2} + \frac{k^2}{m_N^2} - \frac{2pk}{m_\pi m_N}\cos\theta}$ is the center of mass momentum, and $\bar{m} = m_\pi m_N/(m_N + m_\pi)$ is the reduced mass. The sum is over allowed values of the isospin (I), angular momentum values (l), and nucleon spin-projections ($\nu = +, -$). Note that the pseudo-potential is proportional to $\delta^I_{l,\nu}$ and differs from the other choices such as the $T-$matrix, which is proportional to $\sin \delta^I_{l,\nu}$, or the $R-$ matrix that is proportional to $\tan \delta^I_{l,\nu}$.

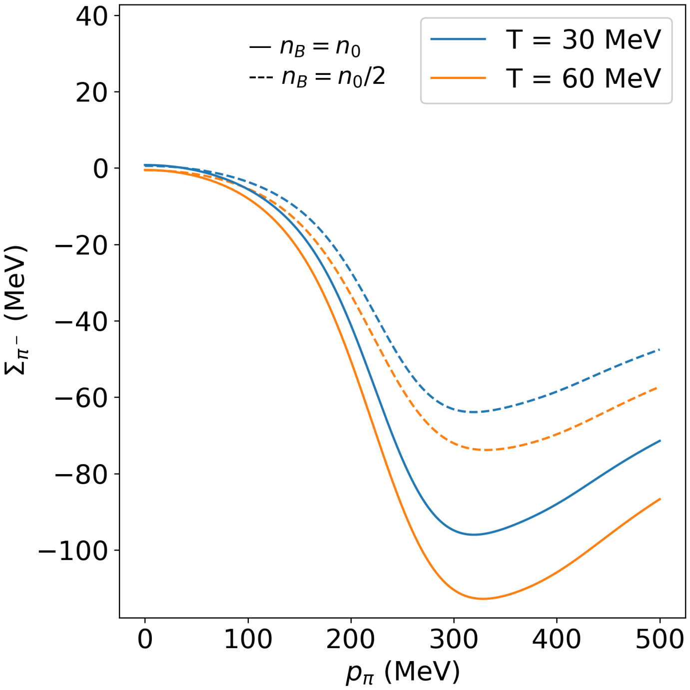

FIG. 11. Pion self-energy predicted by our model at a few representative temperatures and baryon densities.

This choice for the pseudo-potential is motivated by the observation that the second virial coefficient is also proportional to $\delta^I_{l,\nu}$. In addition, Fumi's theorem, a well-known result in condensed matter physics, shows that the calculation of the ground state energy shift due to interactions between particles in a gas and an impurity can be obtained if the pseudo-potential of the form in Eq. 3.29 is used as an effective interaction [58].

This model is consistent with pion-nucleon interactions we expect and is constructed to be consistent with predictions from the virial expansion via the fitting parameters α_l. The separate fitting parameters for s-wave, α_0, and p-wave, α_1, phase shifts are useful due to the much larger p-wave attraction between nucleons and pions. Without this separation, the s-wave phase shifts are overly suppressed. In the work that follows, I present our original analysis where $\alpha = \alpha_0 = \alpha_1$.

We find that the π^- interaction with neutrons dominates the self-energy, which is expected due to the large number of neutrons. The self-energy obtained in this way, with a single fitting parameter α, is shown in Fig. 11. We employ the experimentally measured phase shifts up to $p_{\rm cm} \approx 350$ MeV and assume that they remain constant at higher momentum.

The values for the fudge factor α used to ensure consistency with the virial result are given in table III. It is interesting to note that the fudge factor $\alpha \simeq 1/(2\pi)$ but we do not have an explanation for why this is the case.

α	T=30 MeV	T=60 MeV
$n_B = 0.5n_0$	0.183	0.216
$n_B = 1.0n_0$	0.139	0.171

TABLE III. Values of the fudge factor α needed to obtain consistency.

Although our model for $\Sigma_{\pi^-}(p)$ is admittedly very crude, the modest variation of α over a broad range of densities and temperatures is reassuring. It suggests that our ansatz for the pseudo-potential provides a fair description of the momentum dependence of pion-nucleon interactions. We have explicitly checked that other choices such as the $T-$matrix, which is proportional to $\sin{(\delta^I_{l,\nu})}$, would produce a larger variation of α with temperature and density. We have examined the general behavior of the pion dispersion relation we obtain and find that it is physically plausible. The substantial reduction in the pion energy seen in Fig. 11 at $p_\pi \simeq 300$ MeV is due to the strong p-wave attractive interaction, and the small increase at $p = 0$ arises from weak and repulsive s-wave interaction. The group velocity of the pions is also roughly consistent with general expectations: it is small at low momentum and approaches c (speed of light) at large momenta. At intermediate values $\simeq 350$ MeV we find that the model predicts a group velocity that can exceed c by a few percent - a mild deficiency given the approximations of our model. First, the pseudo-potential in Eq. 3.29 was employed in the Born approximation to calculate Σ_{π^-} and it provided a direct relationship between the self-energy and the phase shifts in Eq. 3.28. This relationship is exact only in the limit when one can neglect correlations between nucleons and nucleon recoils [58]. Second, our approximation that the phase shift remains constant for $p_{\rm cm} \gtrsim 350$ MeV has an effect on the behavior of the pion self-energy at these large momenta. Third, we have neglected the imaginary part of the pion self-energy in the matter. The imaginary part arises due to two-loop contributions involving two nucleons in the medium. For these reasons, we view our model as the first step towards more realistic calculations.

4. TRANSPORT AND BULK VISCOSITY

Neutrino transport and other weak-scale interactions play an important role in supernova, proto-neutron star cooling, and neutron star mergers. During a supernova, the recouping of neutrino energy into the outer layers of the supernova is an important factor in the supernova explosion [6]. For about a minute after the formation of a proto-neutron star, neutrinos are trapped and must diffuse out. After a minute the remnant becomes transparent to neutrinos, marking the change from proto-neutron star to neutron star [9]. In neutron star mergers, oscillations in the density after the violent collision are damped via weak-scale interactions which also often include neutrinos.

The precise way in which the neutrinos couple to matter affects each of these phenomena. Some of the most important reactions for neutrino and anti-neutrino production are the Urca processes, in which thermally excited particles undergo beta and inverse-beta decays [5]. The most efficient Urca process is the direct Urca process involving nucleons:

$$\begin{aligned} n &\rightarrow p + e^- + \bar{\nu}_e, \\ p &\rightarrow n + e^+ + \nu_e \end{aligned} \tag{4.1}$$

which are limited to matter with a proton fraction that exceeds 1/9, $Y_p \geq 1/9$. In matter where this is not satisfied, the modified Urca process, which proceeds with the help of an observer nucleon, is still possible [5].

$$\begin{aligned} n + (n,p) &\rightarrow p + (n,p) + e^- + \bar{\nu}_e, \\ p + (n,p) &\rightarrow n + (n,p) + e^+ + \nu_e \end{aligned} \tag{4.2}$$

The modified Urca rate is suppressed relative to the direct Urca by a factor of $(T/\mu_n)^2 \lesssim 10^{-4}$ to 10^{-5} [5].

4.1. Neutrinos mean free path in dense matter

The mean free path of neutrinos and anti-neutrinos in hot dense matter influences aspects of supernovae dynamics [6], the observable signatures of neutrinos from proto-neutron stars [9, 59, 60], and is expected to play a role in neutron star mergers [19, 61]. At the densities and temperatures encountered in these environments, all three flavors of neutrinos are produced and contribute to the transport of energy, momentum, and lepton number. In matter containing nucleons and leptons, ν_e and $\bar{\nu}_e$ interact most strongly as they encounter both charged-current and neutral-current interactions with nucleons and leptons. The μ and τ neutrinos are coupled to matter only through their neutral-current interactions, as their energies are not adequate to create the heavy charged leptons in the final state. In [26] we have shown that the presence of pions allows for new charged-current reactions for muon neutrinos. We find that these reactions significantly reduce the ν_μ and $\bar{\nu}_\mu$ mean free paths. Further discussion of the effects of pions on neutrino propagation is contained within section 4.2.

In dense nuclear matter, the most important reactions affecting the neutrino mean free path are the Urca reactions, $n + \nu_e \rightarrow p + e^-$ and $p + e^- + \bar{\nu}_e \rightarrow n$, due in large part to the much larger number of nucleons within systems like neutron stars. These are the direct Urca processes, which cannot proceed below some threshold temperature. When the direct Urca process is forbidden, it is believed that similar processes with a spectator nucleon, called the modified Urca processes, are dominant [62, 63].

4.2. Neutrino-pion interactions

The most important reactions for pion effects on neutrino propagation are $\nu_\mu + \pi^- \rightarrow \mu^-$ and $\bar{\nu}_\mu + \mu^- \rightarrow \pi^-$ [26]. The low-energy effective Lagrangian that describes these weak processes is

$$\mathcal{L} = -\frac{G_F \cos\theta_C}{\sqrt{2}} f_\pi \, \partial^\alpha \pi^- \, \bar{\psi}_{\nu_\mu} (\gamma_\alpha (1 - \gamma_5)) \psi_\mu \, , \tag{4.3}$$

where $f_\pi = 130.4$ MeV is the pion decay constant [64]. The amplitude-squared for the process $\bar{\nu}_\mu + \mu^- \rightarrow \pi^-$ is obtained by summing over spin states of the muon in the initial state, and is given by

$$|A|^2_{\bar{\nu}_\mu} = 2(G_F \cos\theta_C f_\pi)^2 m_\mu^2 (E_\pi^2 - p_\pi^2 - m_\mu^2) \, , \tag{4.4}$$

where E_π and p_π are the pion energy and momentum, respectively, and m_μ is the mass of the muon. In the vacuum, energy and momentum conservation forbids the process $\nu_\mu + \pi^- \rightarrow \mu^-$.

However, in dense matter the modification of the pion dispersion relation, which we discuss in detail below, allows for this process when the pion momenta and energy satisfy $E_\pi^2 - p_\pi^2 < m_\mu^2$. In this case, the amplitude-squared is obtained by summing over spin states of the muon in the final state and is given by

$$|A|^2_{\nu_\mu} = 2(G_F \cos\theta_C f_\pi)^2 m_\mu^2 (m_\mu^2 - (E_\pi^2 - p_\pi^2))\,. \tag{4.5}$$

We note that the amplitude-squared is proportional to the square of the lepton mass — a well-known fact that suppresses the decay of pions to electrons. It is for this reason that we focus on interactions involving only muon neutrinos in this work.

Using Fermi's Golden rule, the mean free path of $\bar{\nu}_\mu$ due to the inverse decay reaction is given by

$$\begin{aligned}\frac{1}{\lambda_{\bar{\nu}_\mu}(E_{\bar{\nu}_\mu})} &= \int \frac{d^3\vec{p}_\mu}{(2\pi)^3 2E_\mu} \int \frac{d^3\vec{p}_\pi}{(2\pi)^3 2E_\pi} f_\mu(1+g_\pi) \\ &\quad \times (2\pi)^4 \delta^4(P_\mu + P_{\bar{\nu}_\mu} - P_\pi)|A|^2_{\bar{\nu}_\mu}\end{aligned} \tag{4.6}$$

where g_π and f_μ are the Bose-Einstein distribution for pions and Fermi-Dirac distribution for muons, respectively. When kinematically allowed, the mean free path of ν_μ due to the charged-current reaction is

$$\begin{aligned}\frac{1}{\lambda_{\nu_\mu}(E_{\nu_\mu})} &= \int \frac{d^3\vec{p}_\mu}{(2\pi)^3 2E_\mu} \int \frac{d^3\vec{p}_\pi}{(2\pi)^3 2E_\pi} g_\pi(1-f_\mu) \\ &\quad \times (2\pi)^4 \delta^4(P_\pi + P_{\nu_\mu} - P_\mu)|A|^2_{\nu_\mu}\,.\end{aligned} \tag{4.7}$$

The integrals appearing in Eqs. 4.6 and 4.7 can be further simplified and we find that

$$\frac{1}{\lambda_{\bar{\nu}_\mu}(E_{\bar{\nu}_\mu})} = \frac{1}{16\pi E_\nu^2} \int_{p_l}^{p_h} dp_\pi \frac{p_\pi}{E_\pi} f_\mu(1+g_\pi)|A|^2_{\bar{\nu}_\mu}\,, \tag{4.8}$$

$$\frac{1}{\lambda_{\nu_\mu}(E_{\nu_\mu})} = \frac{1}{16\pi E_\nu^2} \int_{p_l}^{p_h} dp_\pi \frac{p_\pi}{E_\pi} g_\pi(1-f_\mu)|A|^2_{\nu_\mu}\,. \tag{4.9}$$

The limits of the pion momentum integral, p_l and p_h, arise due to energy conservation. For the $\bar{\nu}_\mu + \mu^- \to \pi^-$ reaction, the limits are determined to ensure that

$$-1 \leq \frac{E_\pi}{p_\pi} - \frac{E_\pi^2 - p_\pi^2 - m_\mu^2}{2p_\pi E_\nu} \leq 1\,, \tag{4.10}$$

and for the $\nu_\mu + \pi^- \rightarrow \mu^-$ reaction, they are obtained to ensure that

$$-1 \leq \frac{E_\pi}{p_\pi} + \frac{E_\pi^2 - p_\pi^2 - m_\mu^2}{2p_\pi E_\nu} \leq 1\,. \tag{4.11}$$

When $E_\pi > p_\pi$, Eq. 4.10 can be satisfied when $E_\pi^2 - p_\pi^2 \geq m_\mu^2$ and Eq. 4.11 can be satisfied when $E_\pi^2 - p_\pi^2 \leq m_\mu^2$. For example, at $p_\pi = 125$ MeV, which is near the typical momentum for a pion, nuclear density, and $T = 30$ MeV the inverse pion decay reaction is allowed for neutrinos with energies approximately between 8 MeV and 45 MeV. At high momenta, $p_\pi \gtrsim 200$ MeV, we find that our dispersion relation allows for $E_\pi < p_\pi$ and in this case both reactions are allowed; the range of allowed neutrino energies is only bounded from below. For the inverse pion decay reaction, this lower bound is at very high neutrino energies, but for the $\nu_\mu + \pi^- \rightarrow \mu^-$ reaction the lower bound is around 20-40 MeV in matter at nuclear density and $T = 30$ MeV.

Using the pseudo-potential definition from section 3.3 to define the energy momentum relation of pions in hot and dense matter, we are able to complete the calculation of neutrino mean free paths.

The inverse mean free path due to the reaction $\bar{\nu}_\mu + \mu^- \rightarrow \pi^-$ in matter containing pions at $n_B = 0.5\ n_0$ and $T = 30$ MeV is shown in Fig. 12. The dashed-green curve is calculated using the vacuum dispersion relation for the pions. Since pions only appear in the final state, this curve depends only weakly on the model for pion-nucleon interactions. The solid-red curve is obtained using the dispersion relation in Eq. 3.27, and the self-energy depicted in Fig. 11. Here we see the strong influence of the in-medium dispersion relation, especially at large neutrino energy. The reduction in the pion energy due to its large and attractive p-wave interaction with nucleons implies that a large-momentum pion in the final state is unable to satisfy energy and momentum conservation in the medium. The rapid decrease in the inverse mean free path depicted by the solid-red curve reflects these severe kinematic constraints. At lower neutrino energy, the in-medium dispersion relation leads to a significant reduction of the $\bar{\nu}_\mu$ mean free path. It is remarkable that at these low energies, neutrino processes involving a sparse population of muons and pions are significantly more important than processes involving nucleons and electrons. Neutral-current reactions $\bar{\nu}_\mu + X \rightarrow \bar{\nu}_\mu + X$ where $X = n, p, e^-$ have been studied extensively in earlier work [65, 66] and we use the open-source computer codes from the neutrino opacity library, nuOpac [67], to calculate

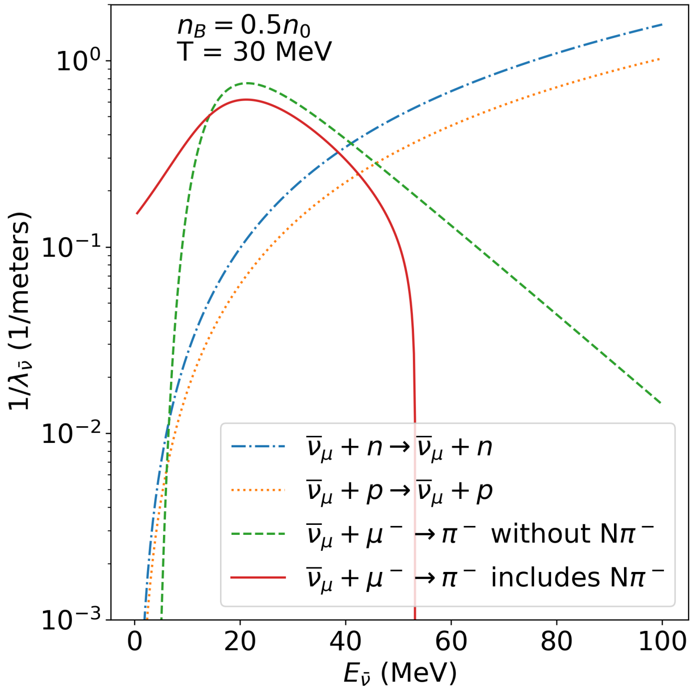

FIG. 12. Antineutrino inverse mean free paths due to the inverse pion decay reaction, with and without $N\pi^-$ interactions included, are compared to the neutral-current reactions involving nucleons.

the neutrino mean free paths. The contributions from the reactions $\bar{\nu}_\mu + n \to \bar{\nu}_\mu + n$, and $\bar{\nu}_\mu + p \to \bar{\nu}_\mu + p$ are shown as the blue dot-dashed and orange dotted curves in Fig. 12. Neutral reactions involving electrons, not shown in the figure, are smaller than those due to the nucleons.

The mean free path of muon neutrinos in matter containing pions at $n_B = 0.5\ n_0$ and $T = 30$ MeV is shown in Fig. 13. This process, which is forbidden in the vacuum, is sensitive to the pion dispersion relation and their abundance. Again, the result, depicted by the solid-red curve, shows some remarkable features. At low energy, the process involving pions is dominant. It remains more important than the charged-current reactions involving nucleons shown as the dashed-green curve, even at higher energies. Neutral-current scattering off nucleons, shown by the blue dot-dashed and orange dotted curves, continues to be the dominant reaction for thermal neutrinos under these specific conditions. The sharp feature in the solid-red curve at $E_\nu \simeq 30$ MeV is due to the non-monotonic behavior of the kinematic constraint in Eq. 4.11.

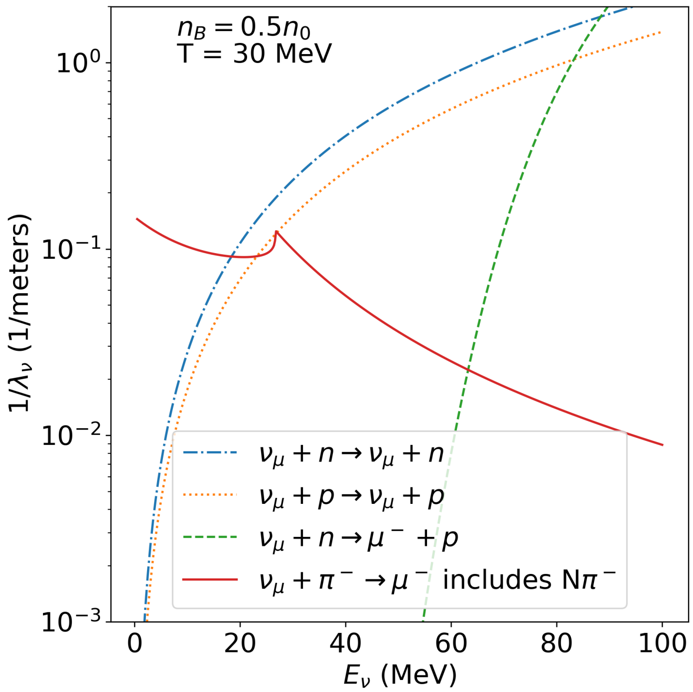

FIG. 13. Neutrino inverse mean free path due to the inverse muon decay reaction is compared with the mean free path due to neutral- and charged-current reactions involving nucleons.

4.3. Bulk viscosity

Bulk viscosity offers a mechanism to damp density oscillations in matter and plays a role in neutron star dynamics [68]. For example, dissipative effects in neutron star mergers influence the lifetime of the hot, dense, hyper-massive neutron star, as well as the post-merger gravitational-wave emission [69]. Bulk viscosity arises due to non-equilibrium reactions that convert chemical energy into thermal energy. This conversion happens because the equilibrium chemical composition of matter changes with density; therefore, the density perturbations induce inelastic reactions.

Since the speed of sound within a neutron star is a large fraction of the speed of light and neutron stars have radii on the order of 10s of km, the characteristic timescale for density oscillations is on the order of milliseconds

$$\frac{R_{\rm NS}}{c_s} = 0.1({\rm ms})\frac{R_{\rm NS}}{10({\rm km})}\frac{c}{3c_s} \tag{4.12}$$

This means that weak reactions play the dominant role in determining the bulk viscosity

[70]. In order to derive an expression for the bulk viscosity, following the same strategy as in reference [71], we begin with an expression for the baryon density in terms of the small density oscillations of interest. We assume that the oscillations are small enough amplitude such that the departure from beta equilibrium $\delta\mu \ll T$.

$$\begin{aligned} n_B(t) &= n_B + \Re(\delta n_B e^{i\omega t}) && (4.13)\\ &= n_B + \delta n_B \cos(\omega t) && (4.14) \end{aligned}$$

where $\delta n_B/n_B \ll 1$. We will assume that the thermal conductivity due to trapped neutrinos [69, 72, 73] is high enough to keep the matter at constant temperature throughout an oscillation. Such an oscillation in baryon density pushes particle fractions away from their values in chemical equilibrium. Weak interactions push the particle fractions back into chemical equilibrium, which takes a certain amount of time. The pressure of nuclear matter, which is a function of the particle fractions, tracks the beta equilibration, and is out of phase with the baryon density oscillation due to the finite rate of the weak interactions. The pressure can be written as

$$\begin{aligned} P(t) &= P_0 + \Re(\delta P e^{i\omega t}) && (4.15)\\ &= P_0 + \Re(\delta P)\cos(\omega t) - \Im(\delta P)\sin(\omega t) && (4.16) \end{aligned}$$

It is the $\Im(\delta P)$ term that represents the phase lag between the pressure $P(t)$ and the baryon density $n_B(t)$ (or volume, as baryon number is conserved) which will give rise to bulk viscous energy dissipation.

The bulk viscosity is defined as the coefficient of a term contributing to energy dissipation

$$\frac{d\varepsilon}{dt} = -\zeta(\nabla\cdot\mathbf{v})^2 \tag{4.17}$$

By rearranging the continuity equation to find an expression for the divergence term in terms of the baryon density

$$\frac{\partial n_B}{\partial t} + n_B\nabla\cdot\mathbf{v} = 0 \tag{4.18}$$

and then averaging over one oscillation period, we can find an expression for the average energy dissipated over an oscillation in terms of the bulk viscosity, frequency, baryon density, and oscillation amplitude.

$$\left\langle \frac{d\varepsilon}{dt} \right\rangle = -\frac{1}{2}\left(\frac{\delta n_B}{n_B}\right)^2 \omega^2 \zeta \tag{4.19}$$

Another expression for the average dissipated energy can be reached from

$$d\varepsilon = \frac{P}{V}\,dV = -\frac{P}{n_B}\,dn_B \tag{4.20}$$

Averaging this expression over one oscillation and using our previous expression for the pressure, we can find

$$\begin{aligned}
\left\langle \frac{d\varepsilon}{dt} \right\rangle &= -\frac{\omega}{2\pi}\int_0^{2\pi/\omega} dt\, P(t)\frac{dn_B(t)\,/\,dt}{n_B(t)} \\
&= -\frac{\omega^2}{2\pi}\left(\frac{\delta n_B}{n_B}\right)\Im(\delta P)\int_0^{2\pi/\omega} dt\sin^2\omega t \\
&= -\frac{\omega}{2}\left(\frac{\delta n_B}{n_B}\right)\Im(\delta P)
\end{aligned} \tag{4.21}$$

Equating 4.19 and 4.21, we find

$$\zeta = \left(\frac{n_B}{\delta n_B}\right)\frac{\Im(\delta P)}{\omega}. \tag{4.22}$$

As expected, the bulk viscosity is related to the imaginary part of the pressure oscillation, which must be determined. This will be done for matter with neutrons, protons, electrons, muons, and negative pions in the following section.

4.4. Pion contribution to the bulk viscosity of neutrino-trapped nuclear matter

In dense nuclear matter, the reaction $e^- + p \leftrightarrow n + \nu_e$, often referred to as the Urca reactions in astrophysics, and the modified Urca reactions $e^- + p + n \leftrightarrow n + n + \nu_e$ change the proton fraction when perturbed and are generally considered to be the main source of bulk viscosity. Recent work has investigated the role of these weak reactions involving nucleons in dense matter with and without neutrino trapping at high temperatures [74, 75].

At $n_B = 0.5n_0$ and $T = 30$ MeV the results in Ref. [75] indicate that the beta equilibrium relaxation time for these reactions is about 10^{-7} s for the neutrino-free case, and about 10^{-9} s when neutrinos are trapped. However, it's possible that under similar conditions reactions involving pions and nucleons would proceed on much faster timescales due to the strong interaction, allowing for faster equilibration of the proton fraction.

Consider a density perturbation in which the final equilibrium state contains a larger neutron fraction. In the absence of reactions involving pions, electron capture reactions $e^- + p \to n + \nu_e$ and $e^- + p + n \to n + n + \nu_e$ generate the needed neutrons. When these reactions are out of equilibrium, they generate heat and dissipation. In the presence of pions and muons there are additional reaction channels that can play a role. These include

$$\pi^- + p + n \leftrightarrow n + n\,, \tag{4.23}$$

$$\mu^- \leftrightarrow \pi^- + \nu_\mu\,, \tag{4.24}$$

$$\mu^- \leftrightarrow e^- + \bar{\nu}_e + \nu_\mu\,, \tag{4.25}$$

$$\pi^- \leftrightarrow \mu^- + \bar{\nu}_\mu\,. \tag{4.26}$$

The non-leptonic reactions mediated by the strong interaction proceed on a timescale that is much faster than the weak reactions involving leptons. We note that although the modification to the pion dispersion relation allows for the process $\pi^- + p \to n$ which is forbidden in the vacuum, in practice we find that these reactions can occur only when the nucleon momentum is very large. At $T = 30$ MeV and $n_B = n_0$ the minimum nucleon momentum needed for this process is $\simeq 730$ MeV. Since this is much larger than the momentum of thermal nucleons, $p_{\text{nuc}} \simeq \sqrt{3MT} \simeq 290$ MeV, we expect that its contribution will be negligible.

In the rest of this section, we will complete our calculation of the bulk viscosity in matter which contains neutrons, protons, electrons, muons, and negative pions and in which neutrinos are trapped. The goal is to outline an investigation of the effects of pions on the bulk viscosity in nuclear matter. The results of this investigation will appear in our forthcoming paper [76].

4.4.1. Particle fractions and weak interactions

Following from equation 4.22, we need to calculate the imaginary part of the pressure. In order to do this calculation we will need to write out the particle fractions x_p, x_μ, and x_π in a form which includes their oscillations caused by the density oscillations. Note that since the neutralization of excess charge occurs on a much faster timescale than our oscillations, we are still able to assume charge neutrality for the neutron star which sets the value of the electron particle fraction once the others are given. The neutron and neutrino particle fractions are determined from the desired independent set by the baryon density input and the input of the conserved lepton fractions $Y_{Li} \equiv (n_i + n_{\nu_i})/n_B$, respectively.

$$\begin{aligned} x_i(t) &= x_i^0 + \Re(\delta x_i e^{i\omega t}) \\ &= x_i^0 + \Re(\delta x_i)\cos(\omega t) - \Im(\delta x_i)\sin(\omega t). \end{aligned} \tag{4.27}$$

Now, the pressure can be expanded around its beta equilibrium value (keeping T fixed throughout the oscillation)

$$\begin{aligned} P = P_0 &+ \left.\frac{\partial P}{\partial n_B}\right|_{T,x_p,x_\mu,x_\pi} \Re(\delta n_B e^{i\omega t}) \\ &+ \left.\frac{\partial P}{\partial x_p}\right|_{T,n_B,x_\mu,x_\pi} \Re(\delta x_p e^{i\omega t}) + \left.\frac{\partial P}{\partial x_\mu}\right|_{T,n_B,x_p,x_\pi} \Re(\delta x_\mu e^{i\omega t}) \\ &+ \left.\frac{\partial P}{\partial x_\pi}\right|_{T,n_B,x_p,x_\mu} \Re(\delta x_\pi e^{i\omega t}). \end{aligned} \tag{4.28}$$

Evidently (from Eqs. 4.27 and 4.28)

$$\begin{aligned} \Im(\delta P) = &\left.\frac{\partial P}{\partial x_p}\right|_{T,n_B,x_\mu,x_\pi} \Im(\delta x_p) \\ &+ \left.\frac{\partial P}{\partial x_\mu}\right|_{T,n_B,x_p,x_\pi} \Im(\delta x_\mu) + \left.\frac{\partial P}{\partial x_\pi}\right|_{T,n_B,x_p,x_\mu} \Im(\delta x_\pi), \end{aligned} \tag{4.29}$$

indicating that to calculate the bulk viscosity (Eq. 4.22), we need the imaginary parts of the particle fractions.

In the matter that we study, all constituent particle species are in thermal equilibrium. This is in contrast to the often-studied case where the matter is neutrino-transparent and therefore reactions that produce neutrinos can only proceed in the forwards direction. In that case, the neutrinos are not in statistical equilibrium [77, 78]. However, in the neutrino-trapped case we study in this work, all weak processes proceed in both directions. The processes proceed in a manner that would balance the chemical potentials on each side of the reaction,

$$\sum_{\text{i in LHS}} \mu_i = \sum_{\text{i in RHS}} \mu_i, \tag{4.30}$$

indicating chemical equilibrium [2, 79].

There are six classes of weak reactions that can occur in the nuclear matter we study, and therefore six chemical potentials $\delta\mu_i$ that are zero in chemical equilibrium. However, three of them are redundant and can be written in terms of three independent equilibrating chemical potentials $\{\delta\mu_1, \delta\mu_2, \delta\mu_3\}$. We assume in this analysis that particles are chemically equilibrated with their respective antiparticles, $\mu_X = -\mu_{\bar{X}}$. This is clearly true for the hadrons and charged leptons, though for neutrinos it is merely a simplifying assumption. Given this, the six classes of reactions are listed below

1. $\delta\mu_1 \equiv \mu_n + \mu_{\nu_e} - \mu_p - \mu_e$
    (a) $n \leftrightarrow p + e^- + \bar{\nu}_e \qquad \overrightarrow{\Gamma} - \overleftarrow{\Gamma} \approx \lambda_a \delta\mu_1$
    (b) $n + \nu_e \leftrightarrow e^- + p \qquad \overrightarrow{\Gamma} - \overleftarrow{\Gamma} \approx \lambda_b \delta\mu_1$
2. $\delta\mu_2 \equiv \mu_n + \mu_{\nu_\mu} - \mu_p - \mu_\mu$
    (a) $n \leftrightarrow p + \mu^- + \bar{\nu}_\mu \qquad \overrightarrow{\Gamma} - \overleftarrow{\Gamma} \approx \lambda_c \delta\mu_2$
    (b) $n + \nu_\mu \leftrightarrow \mu^- + p \qquad \overrightarrow{\Gamma} - \overleftarrow{\Gamma} \approx \lambda_d \delta\mu_2$
3. $\delta\mu_3 \equiv \mu_n - \mu_p - \mu_\pi$
    (a) $n \leftrightarrow p + \pi^- \qquad \overrightarrow{\Gamma} - \overleftarrow{\Gamma} \approx \lambda_3 \delta\mu_3$
4. $\delta\mu_4 \equiv \mu_\pi + \mu_{\nu_e} - \mu_e = \delta\mu_1 - \delta\mu_3$
    (a) $\pi^- \leftrightarrow e^- + \bar{\nu}_e \qquad \overrightarrow{\Gamma} - \overleftarrow{\Gamma} \approx \lambda_e(\delta\mu_1 - \delta\mu_3)$

(b) $\pi^- + \nu_e \leftrightarrow e^-$ $\qquad \overrightarrow{\Gamma} - \overleftarrow{\Gamma} \approx \lambda_f(\delta\mu_1 - \delta\mu_3)$

5. $\delta\mu_5 \equiv \mu_\pi + \mu_{\nu_\mu} - \mu_\mu = \delta\mu_2 - \delta\mu_3$

   (a) $\pi^- \leftrightarrow \mu^- + \bar{\nu}_\mu$ $\qquad \overrightarrow{\Gamma} - \overleftarrow{\Gamma} \approx \lambda_g(\delta\mu_2 - \delta\mu_3)$

   (b) $\pi^- + \nu_\mu \leftrightarrow \mu^-$ $\qquad \overrightarrow{\Gamma} - \overleftarrow{\Gamma} \approx \lambda_h(\delta\mu_2 - \delta\mu_3)$

6. $\delta\mu_6 = \mu_\mu + \mu_{\nu_e} - \mu_e - \mu_{\nu_\mu} = \delta\mu_1 - \delta\mu_2$

   (a) $\mu^- \leftrightarrow e^- + \bar{\nu}_e + \nu_\mu$ $\qquad \overrightarrow{\Gamma} - \overleftarrow{\Gamma} \approx \lambda_i(\delta\mu_1 - \delta\mu_2)$

   (b) $\mu^- + \bar{\nu}_\mu \leftrightarrow e^- + \bar{\nu}_e$ $\qquad \overrightarrow{\Gamma} - \overleftarrow{\Gamma} \approx \lambda_j(\delta\mu_1 - \delta\mu_2)$

   (c) $\mu^- + \nu_e \leftrightarrow e^- + \nu_\mu$ $\qquad \overrightarrow{\Gamma} - \overleftarrow{\Gamma} \approx \lambda_k(\delta\mu_1 - \delta\mu_2)$

   (d) $\mu^- + \nu_e + \bar{\nu}_\mu \leftrightarrow e^-$ $\qquad \overrightarrow{\Gamma} - \overleftarrow{\Gamma} \approx \lambda_l(\delta\mu_1 - \delta\mu_2).$

The total λ of each class of processes is given by

$$\begin{aligned}
\lambda_1 &= \lambda_a + \lambda_b \\
\lambda_2 &= \lambda_c + \lambda_d \\
\lambda_4 &= \lambda_e + \lambda_f \\
\lambda_5 &= \lambda_g + \lambda_h \\
\lambda_6 &= \lambda_i + \lambda_j + \lambda_k + \lambda_l.
\end{aligned} \tag{4.31}$$

The processes shown above can also occur in the presence of spectator particles, but at our level of approximation we will not need to consider them. They either occur in processes we are not calculating, such as for λ_3 which we assume is infinite, or other processes dominate, such as for λ_6.

We neglect processes containing antiparticle counterparts to the particles in the above reactions (except for the neutrinos), as they are subdominant at the temperatures we consider due to the high baryon density.

4.4.2. Weak interaction rates

We calculate the weak interaction rates described in the previous section with Fermi's golden rule, where the rate is determined by a multidimensional phase space integral of the product of a matrix element and the Fermi-Dirac or Bose-Einstein distributions of the involved particles. We perform the full phase space integration and do not make any approximation with respect to the degeneracy of any particle species. The rate calculations are described in Appendix D.

In beta equilibrium, the net rate $\overrightarrow{\Gamma} - \overleftarrow{\Gamma}$ of any particular weak interaction is zero. When the system is pushed out of beta equilibrium by amount $\delta\mu$ ($\delta\mu$ measures the degree of violation of Eq. 4.30), the net rate $\overrightarrow{\Gamma} - \overleftarrow{\Gamma}$ becomes nonzero. The net rate can be calculated for $\delta\mu$ of arbitrary size (see analytic calculations for the direct and modified Urca processes in strongly degenerate npe^- matter in [80]), we consider only subthermal bulk viscosity where $\delta\mu \ll T$. In this regime, the net rate is proportional to the size of the departure from beta equilibrium $\overrightarrow{\Gamma} - \overleftarrow{\Gamma} = \lambda\delta\mu$. In matter where all particles are in statistical equilibrium (like the case we study here), there is a simple relationship between the rate of the process and λ [75, 81]

$$\overrightarrow{\Gamma}(\delta\mu = 0) = \overleftarrow{\Gamma}(\delta\mu = 0) = \lambda T. \tag{4.32}$$

This equation does not hold in neutrino-transparent matter, complicating the calculation of λ [77, 78]. But, for this calculation in neutrino-trapped matter, to calculate λ we only have to calculate the rate of each weak interaction process in beta equilibrium, which is determined by equating the sum of the chemical potentials on each side of the reaction (Eq. 4.30).

At fixed baryon density, the particle fractions evolve according to

$$n_B \frac{dx_p}{dt} = \lambda_1\delta\mu_1 + \lambda_2\delta\mu_2 + \lambda_3\delta\mu_3, \tag{4.33}$$

$$n_B \frac{dx_\mu}{dt} = -\lambda_6\delta\mu_1 + (\lambda_2 + \lambda_5 + \lambda_6)\delta\mu_2 - \lambda_5\delta\mu_3, \tag{4.34}$$

$$n_B \frac{dx_\pi}{dt} = -\lambda_4\delta\mu_1 - \lambda_5\delta\mu_2 + (\lambda_3 + \lambda_4 + \lambda_5)\delta\mu_3 \tag{4.35}$$

4.4.3. Susceptibilities

We introduce the susceptibilities

$$A_i \equiv n_B \frac{\partial \delta\mu_i}{\partial n_B}\bigg|_{T,x_p,x_\mu,x_\pi}, \tag{4.36}$$

$$B_i \equiv \frac{1}{n_B}\frac{\partial \delta\mu_i}{\partial x_p}\bigg|_{T,n_B,x_\mu,x_\pi}, \tag{4.37}$$

$$C_i \equiv \frac{1}{n_B}\frac{\partial \delta\mu_i}{\partial x_\mu}\bigg|_{T,n_B,x_p,x_\pi}, \tag{4.38}$$

$$D_i \equiv \frac{1}{n_B}\frac{\partial \delta\mu_i}{\partial x_\pi}\bigg|_{T,n_B,x_p,x_\mu}, \tag{4.39}$$

where i ranges from 1 to 3. These susceptibilities are properties of the nuclear matter EOS.

We can write the deviations from beta equilibrium $\delta\mu_i$ in terms of deviations of the particle fractions from their beta equilibrium values

$$\begin{aligned}\delta\mu_i = A_i\frac{\delta n_B}{n_B}\cos(\omega t) + n_B\big[B_i\Re(\delta x_p e^{i\omega t})\\ + C_i\Re(\delta x_\mu e^{i\omega t}) + D_i\Re(\delta x_\pi e^{i\omega t})\big],\end{aligned} \tag{4.40}$$

with i again taking values from 1 to 3.

The susceptibilities A_i are plotted in figure 14 and the susceptibilities B_i, C_i, and D_i are plotted in Fig 15.

Finally, we note that the derivatives of the pressure in Eq. 4.28 can be written in terms of susceptibilities by using Maxwell relations. The process is described in Appendix C, and yields

$$\frac{\partial P}{\partial x_p}\bigg|_{T,n_B,x_\mu,x_\pi} = -n_B A_1 \tag{4.41}$$

$$\frac{\partial P}{\partial x_\mu}\bigg|_{T,n_B,x_p,x_\pi} = n_B(A_1 - A_2) \tag{4.42}$$

$$\frac{\partial P}{\partial x_\pi}\bigg|_{T,n_B,x_p,x_\mu} = n_B(A_1 - A_3). \tag{4.43}$$

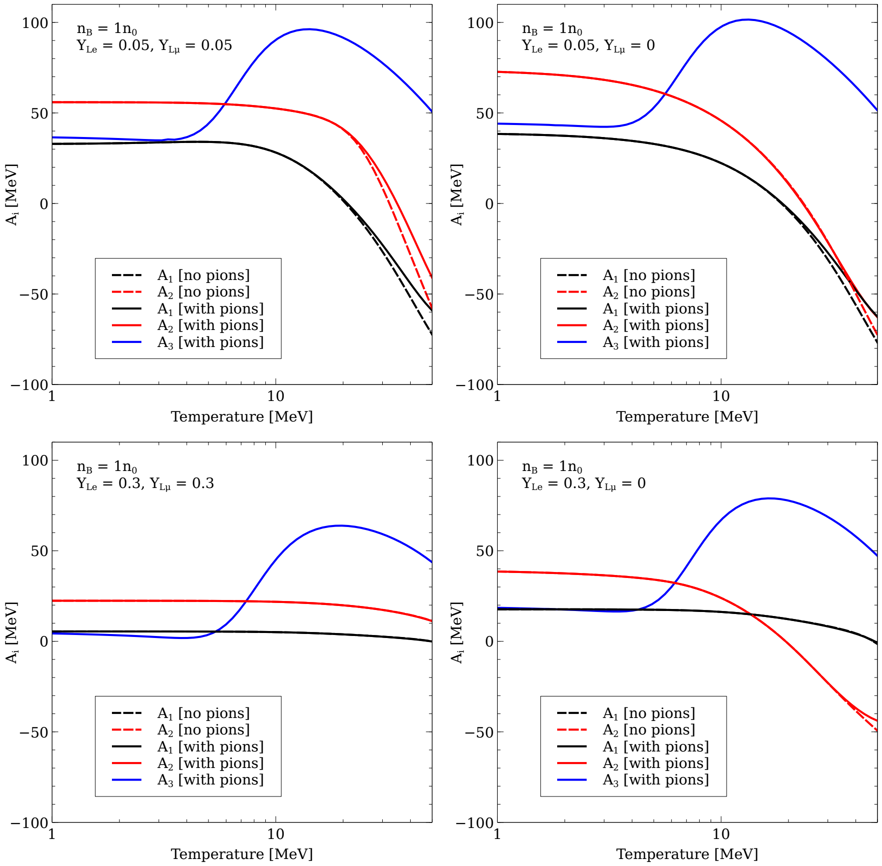

FIG. 14. Susceptibilities of the A type.

4.4.4. Bulk viscosity at finite λ_3

Combining Eqns. 4.22, 4.29, and 4.36, we find the bulk viscosity is given by

$$\zeta = \frac{1}{\omega}\frac{n_B^2}{\delta n_B}\big[-A_1\Im(\delta x_p) + (A_1 - A_2)\Im(\delta x_\mu) + (A_1 - A_3)\Im(\delta x_\pi)\big]. \tag{4.44}$$

To obtain $\Im(\delta x_i)$, we plug Eq. 4.27 and 4.40 into Eqs. 4.33, 4.34, and 4.35 and match the sine terms and the cosine terms. This yields six equations with six variables ($\Re(\delta x_i)$ and $\Im(\delta x_i)$ for $i = p, \mu, \pi$). The three real-part variables can be eliminated, yielding a set of 3 equations to be solved to obtain $\Im(\delta x_p), \Im(\delta x_\mu), \Im(\delta x_\pi)$. Solving the system results in the expression for the bulk viscosity

$$\zeta = \frac{P + Q\omega^2 + R\omega^4}{S + T\omega^2 + U\omega^4 + \omega^6}. \tag{4.45}$$

The expressions for P, Q, R, S, T, U are complex, and are given in Appendix E.

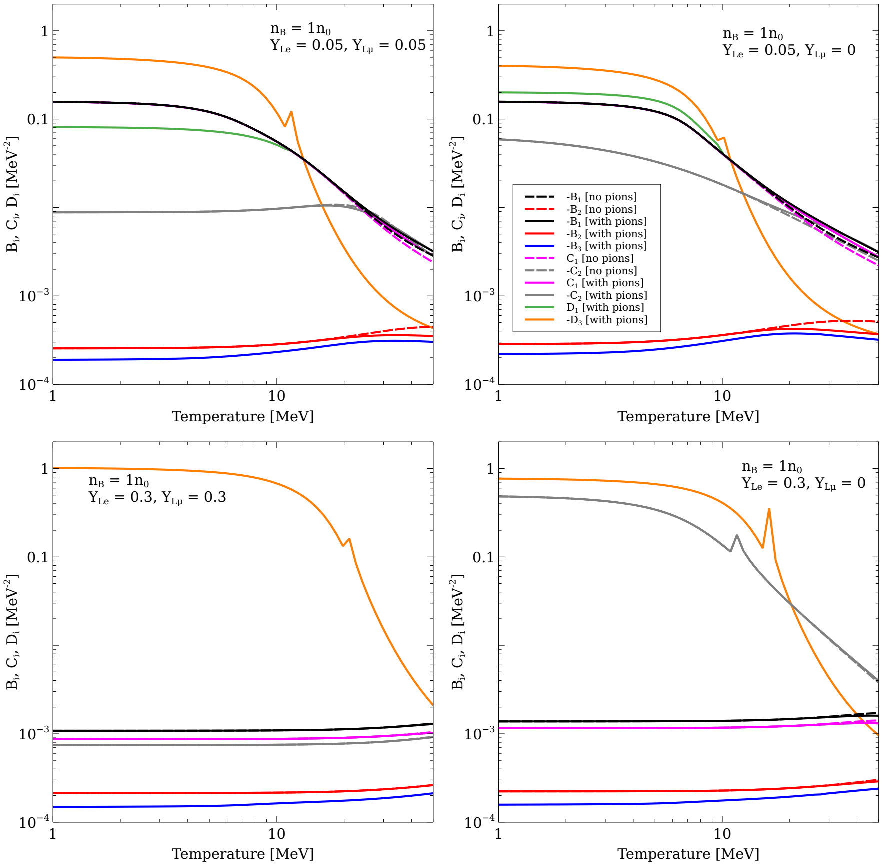

FIG. 15. Susceptibilities of the B, C, and D types.

4.4.5. Bulk viscosity in the limit $\lambda_3 \to \infty$

The reaction $n \leftrightarrow p + \pi^-$ (mediated by a spectator nucleon) is a strong interaction and therefore occurs on a much faster timescale than the weak interactions ($\lambda_1, \lambda_2, \lambda_4, \lambda_5, \lambda_6$) and the timescale of density oscillations in a merger. Therefore, we take $\lambda_3 \to \infty$ in Eq. 4.45.

The limit where $n \leftrightarrow p + \pi^-$ occurs infinitely quickly is subtle. One might assume that $\delta\mu_3$ could simply be set to zero in Eq. 4.33, 4.34, and 4.35. However, it is the product $\lambda_3\delta\mu_3$ that appears on the right-hand side of those equations, and even for very tiny deviations of $\delta\mu_3$ from zero, the product $\lambda_3\delta\mu_3$ could still be sizeable since λ_3 is very large. One must keep λ_3 finite throughout the calculation (up until Eq. 4.45) and then take the limit $\lambda_3 \to \infty$. This was pointed out by [82, 83], and was applied to the case of hyperon bulk viscosity in [84].

The $\lambda_3 \to \infty$ limit of Eq. 4.45 yields

$$\zeta = \frac{\alpha + \beta\omega^2}{\gamma + \varepsilon\omega^2 + \omega^4}. \tag{4.46}$$

The coefficients $\alpha, \beta, \gamma, \varepsilon$ are given in Appendix F. In these expressions, we have set $C_3 = 0$, consistent with the EOS described in an earlier section.

4.4.6. Bulk viscosity without pions

We can obtain the bulk viscosity if pions are not present in the system by setting $\lambda_3 = \lambda_4 = \lambda_5 = 0$ in Eq. 4.45. The EOS would also have to be recomputed without pions. The expression for bulk viscosity in $npe^-\mu^-\nu_e\nu_\mu$ matter which undergoes the reactions corresponding to λ_1, λ_2, and λ_6 is given by

$$\zeta = \frac{\tilde{\alpha} + \tilde{\beta}\omega^2}{\tilde{\gamma} + \tilde{\varepsilon}\omega^2 + \omega^4}. \tag{4.47}$$

where the expressions for $\tilde{\alpha}$, $\tilde{\beta}$, $\tilde{\gamma}$, and $\tilde{\varepsilon}$ are given in Appendix G. As a check, we can see that the susceptibilities A_3, B_3, and C_3 along with all the D_i do not appear in the expression.

4.4.7. Results

The values of λ for the EOS with and without pions are plotted in Fig. 16. The bulk viscosity is plotted in Fig. 17.

Typical bulk viscosity calculations have λ that depend strongly on temperature and susceptibilities that do not depend on temperature. The resonant structure becomes complicated if the susceptibilities become strongly temperature-dependent. For example, conformal points appear when the A susceptibility crosses zero [75].

There are many interesting features of the bulk viscosity curves we find in Fig. 17. Here we will attempt to describe most of the more salient features. Starting with the top left bulk viscosity plot which is made with small values, equal values of the lepton fractions, we note that λ_4 and λ_5 are too slow to contribute to any equilibration process so they create only a very negligible change to the bulk viscosity. This is also true of λ_6, except for at the lowest temperatures on the plot. Any process which λ_4, λ_5, or λ_6 would try to equilibrate

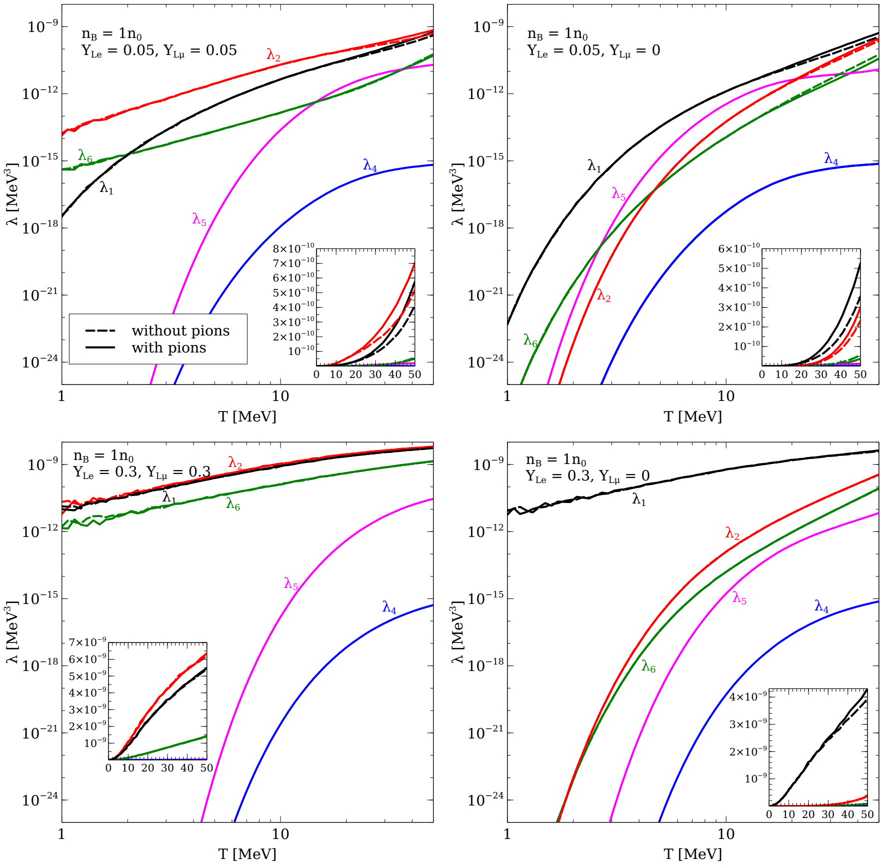

FIG. 16. λ with and without pions

is already equilibrated by the faster λ_1, λ_2, and λ_3. At low temperatures, λ_2 dominates and the bulk viscosity curve is just as if λ_2 was the only process participating in equilibration. The entire behavior of this bulk viscosity curve for $T < 20$ MeV is just the downhill side of the resonance which occurs when the equilibration rate λ_2 matches ω. As T rises to 20 MeV, the susceptibilities A_1 and A_2 begin to drop. At the temperature at which, for example, A_1 is zero, the system becomes partially conformal. When the density is changed slightly, there is not change in the quantity $\delta\mu_1$. If the system was entirely described by $\delta\mu_1$, the bulk viscosity would be zero as the system would be completely conformal with respect to its chemical interactions (like when only direct Urca is considered in $npe\nu_e$ matter in [75]). But the system we study is described by three $\delta\mu_i$, only one of which is conformal at a time, so the bulk viscosity does not drop to zero, but some finite value. The presence of pions shifts the temperature of the conformal points (see Fig. 14), both though modifications of A_1 and A_2, but through the presence of susceptibilities $A_3, B_3, C_3, D_1, D_2, D_3$ which are not present in the pionless case. It is interesting to note that for a wide range of temperatures,

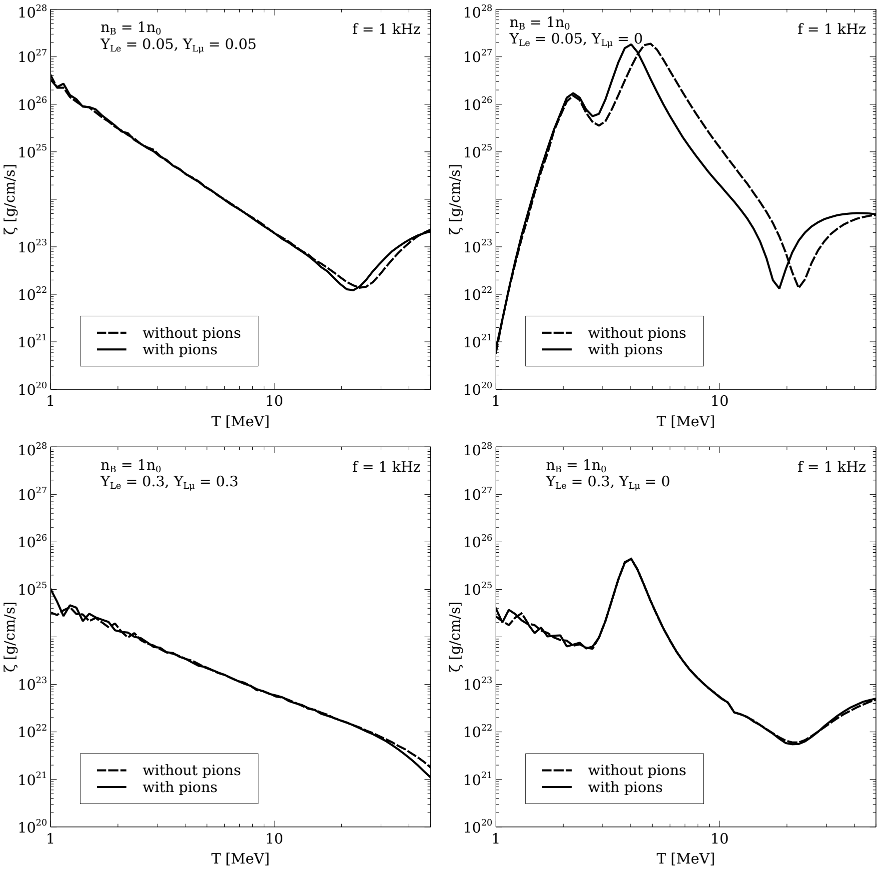

FIG. 17. Bulk viscosity in the EOS with and without pions, for a harmonic density oscillation with frequency 1 kHz.

this bulk viscosity behaves a lot like $\zeta(\lambda_1) + \zeta(\lambda_2)$. This decomposition begins to fail as T rises above ≈ 30 MeV. For all temperatures shown in the plot, we are in the zero-frequency limit, meaning that all beta equilibration occurs much faster than the density oscillation. Additionally, the peak at 20-30 MeV is due to A susceptibilities crossing through zero, not a new resonance.

The top right plot, which corresponds to small electron fraction and zero muon fraction, has a different structure. The peak at $T \approx 2$ MeV is when λ_1 (the fastest process at low temperature) is resonant with 1 kHz density oscillation. Without pions, the next resonance would have been λ_2 matching 1 kHz at $T \approx 5$ MeV. But, when pions are included in the EOS, λ_5 replaces λ_2 as the dominant process, and the resonant peak at $T \approx 4$ MeV is when λ_5 matches the 1 kHz density oscillation. So, pions move the resonant peak temperature lower by 1 MeV. The dip at $T \approx 20$ MeV is again due to the susceptibilities A_1 and A_2 being modified in the presence of pions, plus the entrance of the other “3” susceptibilities into the position of the pseudoconformal points. The bulk viscosity at these high temperatures is controlled by λ_1 and λ_2.

The bottom left plot describes matter with equal lepton fractions which are much larger corresponding to values potentially found in neutron star mergers. Similar to the top left plot, the bulk viscosity here is in the zero-frequency limit. λ_2 dominates the bulk viscosity, with λ_1 becoming slightly important at 40-50 MeV.

The final plot, in the bottom right, corresponds to large electron fraction and zero muon fraction. Again, $\lambda_4 and \lambda_5$ have negligible contributions. λ_6 is mostly negligible, but it has slight effect at $T > 30$ MeV. For $T < 2$ MeV, λ_1 dominates bulk viscosity with a resonant peak which is at lower temperature than the smallest temperature in this plot. The peak at $T \approx 4$ MeV is caused by λ_2 matching 1 kHz. Finally, the bulk viscosity at higher temperatures is dominated by λ_1, λ_2 and to a small extent, λ_6. The crossing of A_2 through 0 causes the minimum at $T \approx 20$ MeV.

5. AXIONS

Axions are a prediction of the most promising solution of the *strong CP-problem*, which is related to the absence of the expected CP violation in the strong interactions [85–88]. The axion phenomenology is widely discussed in the literature (for recent reviews, see Refs. [89–91]). It is essential to remark that axions are expected to couple to photons, electrons, and nucleons, with model dependent couplings [92, 93]. These can be constrained through laboratory experiments [94, 95] and astrophysical considerations [96–98]. In particular, core-collapse SN have long been used to constrain the axion couplings to nucleons [99], photons [100, 101] and recently to muons [102]. In the present work, we are particularly interested in axions coupled to nucleons. In addition to this, the axion is a well-motivated dark matter (DM) candidate [103–105]. Axions produced during inflation would account for the totality of the dark matter in the Universe if their mass is in the range from a few μeV to a few tens of μeV [106, 107], the exact value depending on unknown initial conditions. While this observation has motivated on going experimental searches for axions in the mass range $2 \lesssim m_a \lesssim 25\mu$eV [108, 109], there is interest in axions with higher masses and experimental proposals to discover them [94, 95, 110] for two main reasons. First, recent work shows that if DM axions are produced after inflation, their mass needs to be considerably larger to account for DM. When the contribution of topological defects to the axion production is properly accounted for in post inflationary scenarios, studies find that $m_a \gtrsim 25\mu\text{eV}$ (see, e.g., [89] and references therein). Recent investigations suggest masses as high as 0.5-3.5 meV [111, 112], or even 15 meV [113], depending on the specific axion model. Second, axion masses $m_a \gtrsim 1 - 10\text{meV}$ are particularly interesting for astrophysics, since these axions can have a noticeable impact on stellar evolution, supernovae, and the cooling of white dwarfs and neutron stars [10, 97, 98, 114–117].

Some regions of axion coupling and mass parameter space can be ruled out by measurements we know they would have affected. For example, axions that couple to matter strongly enough to be produced in large numbers, but not strongly enough to become trapped, during a supernova would affect the neutrino production rate. The observed neutrinos from Supernova 1987A provide stringent bounds on the axion nucleon couplings. In all previous studies, the nucleon-nucleon bremsstrahlung reaction, $NN \to NNa$, was assumed to be the dominant channel for the axion production in the supernova. The role of pion induced axion production has been considered, but initial estimates of the thermal pion population were too small for the pion reaction to be competitive. In our paper [118] we reassess the axion emissivity due to the pion reaction, $\pi^- p \to na$, using the new estimates for the thermal pion population coming from the virial approximation described in Sec. 3.2 and [26]. In our second paper on the topic [119] we incorporate the new axion emissivity calculations into general relativistic one-dimensional supernova simulations.

5.1. Axion production by nucleon bremsstrahlung

First calculations of the bremsstrahlung rate were based on a simple model in which the nuclear interaction was described by the exchange of a virtual pion, often referred to as the one-pion-exchange (OPE) approximation [120–122]. Furthermore, these studies neglected to properly account for the pion mass. In subsequent studies, a better treatment of the nuclear interaction beyond the OPE, which was consistent with nucleon-nucleon scattering data[123] and many-body corrections to the nucleon dispersion relations in the medium and its finite lifetime due to multiple scattering [124–126], was shown to reduce the axion emissivity. The consistent inclusion of these effects led to an order of magnitude reduction in the axion emissivity relative to that obtained using the OPE prescription and implied a weaker bound on the axion mass [99]. In later sections calculations of axion emissivity using both the OPE approximation and the updated calculations are implemented within a supernova simulation.

5.2. Axion production by pions

The role of the pion-induced reaction, $\pi^- p \to na$ was first discussed in Refs. [127, 128], and in Ref. [129] it was found to make the dominant contribution for a sufficiently high pion abundance. However, initial estimates suggested that the thermal pion population was too small for the pion reaction to be competitive [10]. For this reason, pions and reactions involving pions in SNe have been largely ignored.

Dense matter in the SN core is charge neutral, close to equilibrium with respect to weak interactions, and characterized by a large isospin asymmetry. The difference between the neutron and proton chemical potentials, denoted by $\hat{\mu} = \mu_n - \mu_p$, increases with density and becomes comparable to the pion mass $m_\pi \simeq 139$ MeV when the baryon density $n_B \geq n_0$, where n_0 is the nuclear saturation density. In the SN core, where neutrinos are trapped and weak equilibrium is quickly obtained, the pion chemical potential $\mu_{\pi^-} = \hat{\mu} = \mu_e - \mu_{\nu_e}$. When $\mu_{\pi^-} \simeq m_\pi$ number density of negatively charged pions is greatly enhanced even when the ambient temperature realized in SNe, which is in the range of few MeV to few tens of MeV, is small compared to m_π. When $\mu_{\pi^-} > m_\pi$ Bose-Einstein condensate of pions is favored, but whether or not this can be achieved at the densities encountered in SN matter is unclear [40]. In what follows, we will only consider matter at densities where $\mu_{\pi^-} < m_\pi$. Under these conditions, the energy cost of introducing pions in dense matter is lowered by attractive p-wave interactions between nucleons and thermal pions (with typical momentum $p_\pi \simeq \sqrt{6 m_\pi T} \simeq 160\sqrt{T/30\text{MeV}}$ MeV).

Using the model independent calculation of thermal pion number including pion-nucleon interactions from section 3.2 and the pion self-energy model from section 3.3 we will be able to determine the number of axions emitted by the pion-axion reactions. For these calculations we have used the self-energy model with equal free parameter for s-waves and p-waves.

The number of axions emitted per unit volume and per unit of time and energy is given by [130]

$$\frac{d\dot{n}_a}{d\omega_a} = \int \frac{2d^3\mathbf{p}_p}{(2\pi)^3 2m_N} \frac{d^3\mathbf{p}_\pi}{(2\pi)^3 2E_\pi} \frac{2d^3\mathbf{p}_n}{(2\pi)^3 2m_N} \frac{4\pi\omega_a^2}{(2\pi)^3 2\omega_a} \\ \times (2\pi)^4 \delta^4(p_f - p_i) |\overline{\mathcal{M}}|^2 f_p f_\pi (1 - f_n) \ . \tag{5.1}$$

The squared transition matrix element in Eq. (5.1) is averaged over both initial and final nucleon spins and given by

$$|\overline{\mathcal{M}}|^2 = 4\bar{g}_{aN}^2 \gamma_{\rm sf}(\omega_a) \left(\frac{g_A}{2F_\pi}\right)^2 |\mathbf{p}_\pi|^2 \,, \tag{5.2}$$

where $\mathbf{p}_\pi$ is the pion momentum, $g_A = 1.26$ is the axial coupling, and $F_\pi = 92.4$ MeV is the pion decay constant. The effective axion-nucleon coupling $\bar{g}_{aN}$ is defined as

$$\bar{g}_{aN}^2 = g_a^2 \left[\frac{1}{2}(C_{ap}^2 + C_{an}^2) + \frac{1}{3} C_{an} C_{ap}\right] \,, \tag{5.3}$$

where $g_a = m_N/f_a$, m_N being the nucleon mass and f_a the Peccei-Quinn scale. We note a discrepancy in Eq. (5.3) with respect to the result [127, 129], i.e., a minus sign in front of the $1/3 C_{an} C_{ap}$ term. This difference arises because the mixed term in the matrix element is $-\frac{1}{2} C_{an} C_{ap} \left[2\langle(\hat{\mathbf{p}}_a \cdot \hat{\mathbf{p}}_2)^2\rangle - 1\right]$ and the average over the directions gives $\langle(\hat{\mathbf{p}}_a \cdot \hat{\mathbf{p}}_2)^2\rangle = 1/6$. Depending on the axion couplings, this correction gives, at most, a difference of a factor 2 compared to previous literature.

The C_{ai} are the model-dependent $\mathcal{O}(1)$ dimensionless axion-fermion couplings. The couplings have been recently calculated for the KSVZ [131, 132] and the DFSZ [133, 134] models in Ref. [92] (see [90] for a discussion of these parameters in a large class of axion models). The function $\gamma_{\rm sf}(\omega_a) = \omega_a^2/[\omega_a^2 + (\Gamma/2)^2]$ in Eq. (5.2) is a simple ansatz suggested in Refs. [125, 128] to account for the finite lifetime of the nucleon spin due to scattering in the dense medium, and Γ is the nucleon spin fluctuation rate. At a fiducial temperature $T = 30\,\mathrm{MeV}$ and mass density $\rho = 10^{14}\,\mathrm{g/cm^3}$, the calculations in [99, 135] indicate that $\Gamma \simeq 35\,\mathrm{MeV}$.

The distribution functions of the different interacting species are the usual Fermi-Dirac or Bose-Einstein distribution,

$$f_i(E) = \frac{1}{e^{[E_i(p_i)-\mu_i]/T} \mp 1} \ , \tag{5.4}$$

where the $+$ sign applies to fermions, while the $-$ is for bosons, and μ_i are the chemical potentials for $i = p, n, \pi$. Corrections to the dispersion relations $E_i(p_i)$ of nucleons are incorporated through the equation

$$E_i = m_N + \frac{|\mathbf{p}_i|^2}{2m_N^*} + U_i \ \ , \tag{5.5}$$

where the nucleon effective mass m_N^* and single-particle potentials U_i are obtained from Ref. [26]. The modification to the pion dispersion relation due to its interactions with nucleons is incorporated through Eq. (3.27) with $\Sigma(p)$ obtained consistently as described in my paper Ref. [26] as well as Sec. 3.3.

The differential axion number luminosity, which is defined to be the total number of axions emitted in a specified energy range per unit time from the SN is obtained by integrating Eq. (5.1) over the SN volume and is given by

$$\frac{d\mathcal{N}_a}{d\omega_a} = \int d^3r \, \frac{d\dot{n}_a}{d\omega_a} \ . \tag{5.6}$$

The energy radiated in axions per unit volume and time, called the axion emissivity, can be calculated directly from Eq. (5.1) as

$$Q_a = \int d\omega_a \omega_a \frac{d\dot{n}_a}{d\omega_a} \, , \tag{5.7}$$

where the phase-space integrals can be performed to obtain a simpler expression for pionic processes

$$\begin{aligned} Q_a^\pi = \frac{\bar{g}_{aN}^2 T^{7.5}}{\sqrt{2\,m_N}\,\pi^5} \left(\frac{g_A}{2F_\pi}\right)^2 \frac{z_\pi\, z_p}{1+z_n} \left[\int dx_p \frac{x_p^2}{e^{x_p^2}+z_p}\right] \\ \int dx_\pi \frac{x_\pi^3 \epsilon_\pi^2}{(e^{\epsilon_\pi - y_\pi} - z_\pi)} \frac{\epsilon_\pi^2}{[\epsilon_\pi^2 + (\Gamma/2T)^2]} \, , \end{aligned} \tag{5.8}$$

with $x_p = |\mathbf{p}_p|/\sqrt{2m_N T}$, $x_\pi = |\mathbf{p}_\pi|/T$, $y_\pi = m_\pi/T$, and $\epsilon_\pi = E_\pi/T$. The fugacities z_π and

TABLE IV. Axion emissivities Q_a in units of $10^{32}\,\mathrm{erg\,cm^{-3}\,s^{-1}}$ and luminosities L_a in units $10^{51}\,\mathrm{erg\,s^{-1}}$ for KSVZ model ($C_{ap} = -0.47\ ; C_{an} = 0$) and $g_a = m_N/f_a = 10^{-9}$, for different post-bounce times.

$t_{\rm pb}$ (s)	ρ (10^{14}g/cm^3)	T (MeV)	Y_π	Q_a^{NN} (10^{32} erg / cm^3 s)	Q_a^{π} (10^{32} erg / cm^3 s)	$Q_a^{\rm tot}/Q_a^{NN}$	L_a (10^{51} erg / s)
1	1.45	37.07	0.011	1.37	4.63	4.38	4.0
2	2.08	38.93	0.016	3.28	8.87	3.70	8.10
4	3.10	40.56	0.027	9.08	15.87	2.75	16.63
6	3.65	39.91	0.034	12.92	14.99	2.16	18.61

TABLE V. Bound on the effective axion-nucleon coupling $\bar{g}_{aN}$ obtained using Eq. (5.10). The corresponding bound on m_a and f_a for KSVZ model with $C_{ap} = -0.47\,, C_{an} = 0$ are also shown.

ρ		$\bar{g}_{aN}$ ($\times 10^{-9}$)	m_a (meV)	f_a ($\times 10^8$ GeV)
ρ_0	only NN	0.81	21.02	2.71
	$\pi N + NN$	0.46	11.99	4.75
$\rho_0/2$	only NN	0.93	24.11	2.36
	$\pi N + NN$	0.42	10.96	5.20

z_p were defined earlier. Finally, the total axion energy luminosity is given by

$$L_a = \int d^3r\, Q_a(r) \ . \tag{5.9}$$

The enhancement of the axion emission rate due to the pion reaction relative to the bremsstrahlung calculated in [99] can be gauged from Table IV, where we compare the πN and NN axion emissivity at different post-bounce times using ambient conditions taken from the SN model described in [99] at a specific radial location $r = 10\,\mathrm{km}$. We estimate the total axion emissivity L_a by assuming average values for T and ρ within the region $r < 12$ km. This is shown in the last column of the Table. We realize that the axion emissivity is increased by factor of about 4 due to pionic reactions at $t_{\rm pb} = 1$ s. At later times, the pion contribution is less important: the total emissivity is only a factor 2 larger than the one from NN process for $t_{\rm pb} = 6$ s.

The more stringent bound on the axion mass implied by the larger emissivity can be estimated using an observation made by Raffelt [96] who found that, for

$$\frac{Q_a}{\rho} > 10^{19}\,\mathrm{erg\,g^{-1}\,s^{-1}}\ , \tag{5.10}$$

simulations predicted a significant shortening of the SN 1987A neutrino signal. The axion emissivity is typically calculated at a fiducial density $\rho = \rho_{\rm sat}$, $T = 30\,\mathrm{MeV}$, and proton fraction $Y_p = 0.3$. In Table V we show the bounds derived for the KSVZ axion obtained using the fiducial densities $\rho = \rho_{\rm sat}$ and $\rho = \rho_{\rm sat}/2$ at temperature $T = 30\,\mathrm{MeV}$ and proton fraction $Y_p = 0.3$. Since the rates are $\propto m_a^2$, the factor of 4 enhancement in the rate strengthens the axion mass bound by a factor 2.

In the DFSZ model, the axion-nucleon couplings are expressed as a function of $\tan\beta \equiv v_u/v_d$, which represents the ratio of the two Higgs bosons in the model and is constrained in the range $0.25 < \tan\beta < 170$ [90]. Correspondingly, in this case for $\rho = \rho_{\rm sat}$ when including pions, the axion mass bound is shifted from $9.3\,\mathrm{meV} < m_a < 17.7\,\mathrm{meV}$ to $5.8\,\mathrm{meV} < m_a < 10.9\,\mathrm{meV}$.

We caution the reader that, while this simple estimate captures that trend and the relative importance of the pion reaction, detailed SN simulations with pions will be needed to derive a robust bound.

We also remark that in the mass range of interest axions are not trapped in the SN core. This can be shown by calculating the mean free path for this process. Following [10], we obtain

$$l_\pi^{-1} = \frac{\bar{g}_{aN}^2 \pi}{4 m_N^4}\left(\frac{g_A}{2F_\pi}\right)^2 \frac{\rho^2 Y_p Y_\pi}{T} \tag{5.11}$$

in the non-degenerate limit for nucleons and pions, neglecting the pion mass and the multiple nucleon scattering effect. The first approximation is reasonable in the region around the SN core; the other two approximations are conservative since that would only reduce the mean free path. For typical SN conditions, the mean free path results $l_\pi \sim (\bar{g}_{aN}/10^{-9})^{-2}\,10^5\,\mathrm{km}$. This finding confirms that axions are in the free-streaming regime for $\bar{g}_{aN} < 10^{-7}$.

In addition to increasing the total axion emissivity, the reaction involving pions produces axions with a harder energy spectrum. This is to be expected as these reactions harness the rest mass energy of the pion in the initial state. Fig. 18 compares the axion number luminosity obtained from pionic reactions (solid curve) to those from nucleon bremsstrahlung

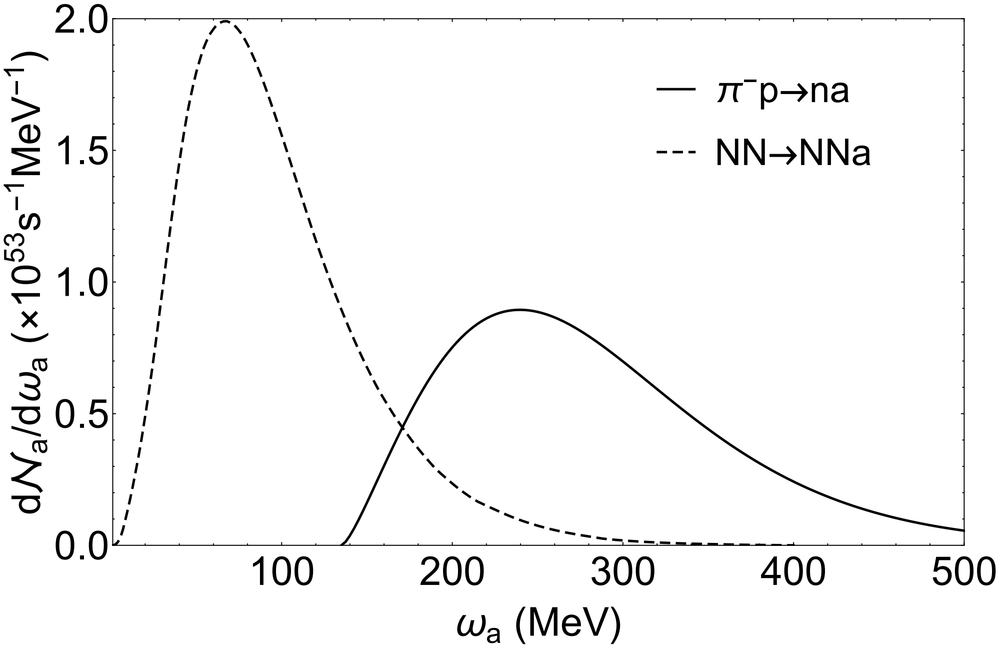

FIG. 18. The number spectra of axions for πN (solid curve) and NN (dashed curve) processes for our benchmark axion model at a post-bounce time $t_{\rm pb} = 1\,{\rm s}$.

(dashed curve) for our benchmark axion model at a post-bounce time $t_{\rm pb} = 1\,{\rm s}$.

The larger axion energies, especially axions in the range $200 - 300\,{\rm MeV}$ are particularly interesting for detection in neutrino underground experiments. This is because at these energies we expect a resonant enhancement of the axion-nucleon cross section due to the Δ intermediate state. These high energy axions can produce neutral and charged pions in water Cherenkov detectors due to the reactions $a+p \rightarrow p+\pi^0$, $a+p \rightarrow n+\pi^+$, and $a+n \rightarrow p+\pi^-$. The operator structure that describes axion coupling to nucleons is nearly identical to the pion-nucleon coupling, but with f_π replaced by f_a. This observation has been used earlier to suggest that the cross section for the reaction $a+p \rightarrow N+\pi$, $\sigma_{aN} \simeq (F_\pi/f_a)^2\sigma_{\pi N}$ where $\sigma_{\pi N}$ is the cross section for $\pi^0+p \rightarrow p+\pi^0$ [114]. In the resonance region, which can be accessed when the axion energy $E_a \simeq 200 - 300\,{\rm MeV}$, the cross-section $\sigma_{\pi N} \approx 100$ mb. For $f_a = 10^9\,{\rm GeV}$ ($m_a = 5.7\,{\rm meV}$), an order of magnitude estimate obtained using the axion luminosity in Table IV suggests that about 1000 pions will be produced in a megaton water Cherenkov detector for a SN at $1\,{\rm kpc}$.

5.3. Axion production in supernova simulations

With the recent advances in the modelling of core-collapse SN, which now allow the inclusion of muons as degree of freedom and to treat 6-species Boltzmann neutrino transport schemes [1, 136], it becomes possible to study novel high-energy astro-particle physics phenomena. Besides muons the next heavier degrees of freedom to consider are the pions. These bosons exist as charge neutral π^0 and as charged $\pi^\pm$. Pions are one of the key messengers in the context of heavy-ion collisions (for a recent comprehensive review see Ref. [137]), which makes them one of the best studied particle degrees of freedom. The role of pions in neutron stars has been studied for a long time, particularly in relation to the emergence of a pion condensate. However, in the context of core-collapse SN, only the core-collapse SN simulations of Ref. [138] included pions in the equation of state (EOS). Recently, the *classical* neutron star EOS of Akmal, Pandharipande and Ravenhall, denoted as APR [41, 139], was extended to finite temperatures and arbitrary isospin asymmetry applying a Skyrme functional model, prepared for astrophysical applications [140]. Pions are included through the phase transition to a neutral pion condensate at supersaturation density. This results in a softening of the EOS. As was pointed out in Ref. [26], an even greater impact on the high-density EOS emerges already below saturation density when considering the contributions from strongly-interacting pions, giving rise to the pion self-energy. The resulting pion yields can be comparable to those of muons, depending on the nuclear EOS. In this article we employ this formalism, based on the virial EOS featuring pion-nucleon scattering phase shifts, and study the appearance of pions in simulations of the PNS deleptonization.

The inclusion of pions in the EOS allows us to describe, for the first time, the full impact of axions on the SN evolution in a self-consistent way. For axions coupling to nucleons, the most widely studied mechanism for axion production in a SN core is the nucleon-nucleon bremsstrahlung, $N + N \to N + N + a$ [99, 121, 141–144]. Due to the efficient energy loss through axions, the above process contributes to the shortening of the neutrino emission from a core-collapse SN. Quantitatively, this time reduction is parameterized by axion-nucleon coupling [145]. The current bound on the axion-nucleon coupling has been revisited [99], with improved nucleon-nucleon bremsstrahlung rates for the axion emissivity taking into account leading-order medium modifications. Furthermore, in the context of core-collapse SN, there is a second competing process for the emission of axions, which has long been omitted, namely the emission of axions from Compton pionic processes, $\pi^- + p \rightarrow n + a$ [120, 128, 146]. This process has been reviewed recently in the context of strongly-interacting pions under the conditions of hot neutron stars [118]. It leads to the conclusion that the previous assumption of the dominating axion emission from nucleon-nucleon bremsstrahlung over those from pions must be relaxed.

In order to quantify the impact of axion losses originating from pions, the present study implements the associated axion emissivities [118] in simulations of the PNS deleptonization phase of a core-collapse SN explosion, together with the updated axion emissivities from nucleon-nucleon bremsstrahlung [99]. Particular emphasis is devoted to the impact of the shortening of the neutrino emission due to the associated enhanced cooling, and the potentially observable signature at the future-planned Hyper-Kamiokande and presently operating Super-Kamiokande water-Cherenkov detectors.

5.3.1. Supernova model with pions

The spherically symmetric core-collapse SN model employed in this study, `AGILE-BOLTZTRAN`, is based on general relativistic neutrino radiation hydrodynamics [147–150]. It includes an adaptive baryon mass mesh refinement [151, 152], where for the present study we use 207 radial mass shell grid points. `AGILE-BOLTZTRAN` has been extended to handle six-species Boltzmann neutrino transport [136] with the inclusion of the muon abundance, Y_μ, as additional degree of freedom, together with a comprehensive set of muonic weak interactions in the collision integral of the Boltzmann transport equation [136, 153]). The list of standard, non-muonic weak processes used here can be found in Table I of Ref. [154], with the charged-current weak rates, including the (inverse) neutron decay channel, in the full-kinematics treatment as well as including self-consistently contributions from weak magnetism. The latter two are particularly important for the PNS deleptonization phase, as was discussed in Ref. [154]. The neutrino distributions and transport is discretized with 6 momentum angles, $\cos\vartheta \in [-1, 1]$, and 36 neutrino energy bins, $E_\nu \in [0.5, 300]$ MeV, following the setup of S. Bruenn [155].

`AGILE-BOLTZTRAN` has a flexible EOS module which can handle a variety of different nuclear matter EOS [156–160]. In the present work the DD2 relativistic mean-field EOS with density-dependent nucleon-meson coupling is employed [161–163], together with the modified nuclear statistical equilibrium EOS of Ref. [158] for the description of medium nuclear clusters, henceforth denoted as HS(DD2). It provides a good description of nuclear saturation properties as well as neutron star configurations, consistent with current maximum mass constraints from the observations of massive pulsars of about 2 $M_\odot$ [164, 165]. Furthermore, electrons, positrons and photons are treated following Ref. [166], while the muon EOS is based on a tabulation [136].

The present work extends previous studies of axion emission in core-collapse SN [145], which exclusively focused on nucleon-nucleon bremstrahlung. Here we add a novel process of axion emission involving pions [118]. To study self consistently the effects of this process in the SN evolution, pions have to be included in the SN simulation. Pions have a mass of $m_{\pi^{0,\pm}} = 135(140)$ MeV and are hence only slightly more massive than muons. Unlike muons, which are not in chemical equilibrium and hence are exclusively produced from weak processes under SN conditions, pions are in chemical equilibrium through strong interactions. Hence, it is not required to solve an evolution equation for the pion abundances, as it is the case of muons [1, 136]. Instead, their abundances can be calculated from the corresponding local thermal and chemical equilibrium conditions for a gas of massive and relativistic bosons. This implies that the pions have a chemical potential, $\mu_{\pi^\pm} = \mp\hat{\mu}$, where $\hat{\mu} \equiv \mu_n - \mu_p$ is the chemical potential for negative charge, and $\mu_{\pi^0} = 0$.

Furthermore, pions are subject to strong interactions. At low-density and high temperature, the virial expansion provides an efficient and model independent approach to include pion-nucleon interactions. Under these conditions, when the pion and nucleon fugacities are small, the modification of the pion density and thermodynamics due to their interactions with neutrons and protons is adequately incorporated through the second virial coefficients, $b_2^{n\pi}$ and $b_2^{p\pi}$, respectively. We employ the methods described in Ref. [26] to calculate these coefficients using measured pion-nucleon scattering phase-shifts.

To describe reactions involving pions and nucleons, we will need in addition a model for the pion dispersion relation in the hot and dense medium. We adopt the simple pseudopotential model described in Ref. [26] and write the pion energy as

$$E_{\pi^-} = \sqrt{p^2 + m_{\pi^-}^2} + \Sigma_{\pi^-}(p_\pi) \ , \tag{5.12}$$

where $\Sigma_{\pi^-}(p_\pi)$, is the momentum $p_p i$ dependent real part of the pion self-energy. The

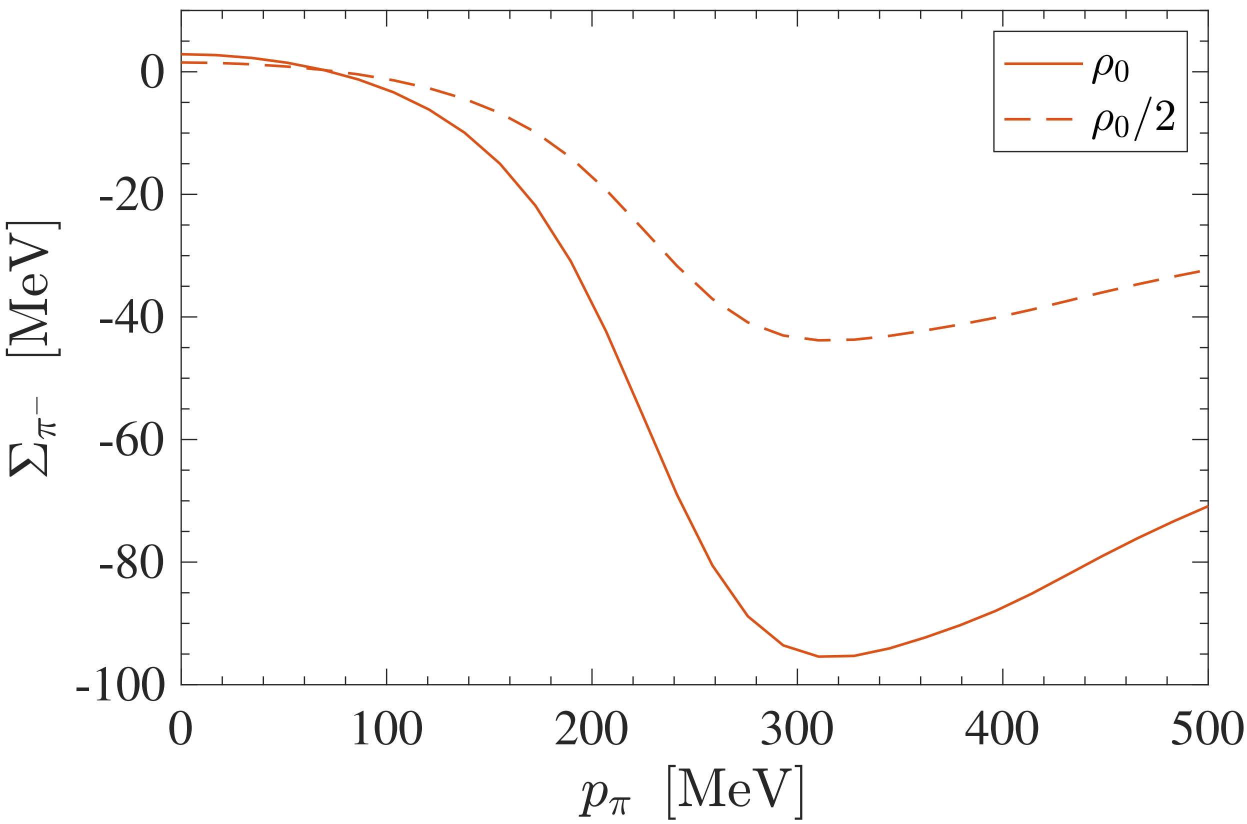

FIG. 19. Momentum p_π dependent pion self-energy for π^-, Σ_{π^-}, calculated based on the nucleon-nucleon potential, Eqs. (21)–(22) in Ref. [26], evaluated at a temperature of $T = 20$ MeV and at fixed electron and muon abundances of $Y_e = 0.15$ and $Y_\mu = 0.04$, as well as two different baryon densities, at saturation density (solid line) and at one half of saturation density (dashed line).

strength of the pseudo-potential is tuned to ensures that the number densities obtained are consistent with the virial expansion[26]. The model includes the weakly repulsive s-wave interaction and the strongly attractive p-wave interactions between pions and nucleons. The latter has the effect of enhancing the π^- and proton abundances (see Fig. 2 in Ref. [26] and make a substantial contribution to the EOS. Since the pion self-energy, Σ_{π^-}, use the knowledge of the nucleon's equilibrium Fermi-Dirac distribution functions, with the associated nucleon chemical potentials, together with the pion-nucleon potential—see expressions (21) and (22) in Ref. [26]—it becomes evident that interaction contributions have to be consistent with the underlying nuclear HS(DD2) EOS. The pion self-energies are shown in Fig. 19 for selected conditions relevant for the PNS deleptonization. It becomes clear that their contributions are indeed significant and cannot be neglected, neither for the calculation of the pion contributions to the EOS nor for the emission of axions stemming from pions, as

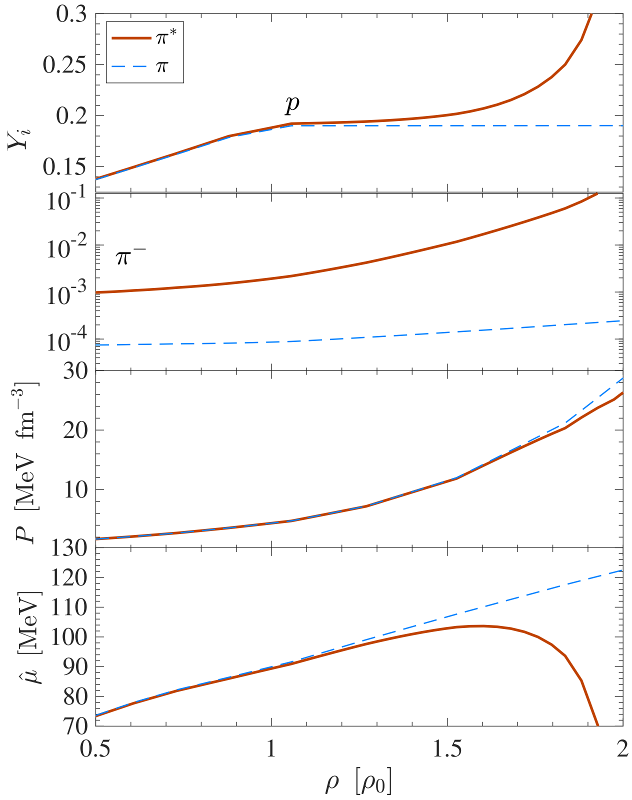

FIG. 20. EOS comparison, showing the particle yields, Y_i, of protons (p) and pions (π^-), the total pressure, P, and the charged chemical potential, $\hat{\mu}$, as a function of the baryon density, ρ, in units of the saturation density, ρ_0, comparing the model with only thermal pions (blue dashed lines) and with interacting pions (brown solid lines), for the nucleon-nucleon potential (Eqs. (21)–(22) in Ref. [26]), evaluated at a temperature of $T = 20$ MeV and fixed electron and muon abundances of $Y_e = 0.15$ and $Y_\mu = 0.04$.

will be discussed further below.

Note that the yields of π^+ are strongly suppressed due to the contributions of the Boltzmann suppression term, $Y_{\pi^+} \propto \exp\{-\hat{\mu}/T\}$, in comparison to $Y_{\pi^-} \propto \exp\{\hat{\mu}/T\}$. A similar suppression is found for π^0, in comparison to π^-. Furthermore, we have calculated the self-energies for π^+ which are found to be similar to those of π^-, and hence we find that at all conditions, the abundances of π^+ and π^0 are indeed negligible.

With the inclusion of pions, the charge neutrality condition is modified. It results in the following definition of the proton abundance, $Y_p = Y_e + Y_\mu + Y_{\pi^-} - Y_{\pi^+}$, which is one of the three independent nuclear EOS variables, in addition to temperature and baryon (or restmass) density. This results in a feedback to the baryon EOS, which is illustrated in Fig. 20 for a selected temperature of $T = 20$ MeV, an electron fraction and a muon fraction of $Y_e = 0.15$ and $Y_\mu = 0.04$, lowering the abundance of neutrons and increasing the abundance of protons. For the calculation of the pion pressure and energy density, we used expressions (9) and (10) of Ref. [26].

The question about weak interactions involving pions, i.e. the π^- decay and its inverse, $\bar{\nu}_\mu + \mu^- \leftrightarrows \pi^-$, and $\nu_\mu + \pi^- \leftrightarrows \mu^-$, has already been addressed in Ref. [26]. Note that the latter is only possible in the presence of interacting pions, i.e. when Σ_{π^-} is large and negative to ensure energy and momentum conservation. These reactions are competing not only with the neutral-current scattering processes, as was discussed in Ref. [26], but also with the muonic charged-current reactions as well as the purely leptonic reaction channels [136, 153], giving additional contributions to the ν_μ and $\bar{\nu}_\mu$ opacity accordingly.

The conditions for these weak processes requires a finite abundance of π^-. This is the case at densities in excess of about $\rho \simeq 10^{13}$ g cm^{-3}. This, in turn, corresponds to temperatures fairly above $T > 10$ MeV during the SN evolution, where the muon-(anti)neutrinos are trapped entirely [167]. As was found in Ref. [26], these weak processes would contribute mostly to low muon-(anti)neutrino energies. Hence, it may leave an imprint on the long-term muon neutrino signal during the later PNS cooling phase, i.e. when the temperature drops at the PNS surface and the neutrinospheres shifts to higher densities continuously. Here, for the study of the early PNS deleptonization phase for no more than about 10 s, the inclusion of weak reactions with pions has a negligible impact on the neutrino emission.

Results from SN simulations which include muons and pions, the latter both non-interacting and interacting, are presented in section 5.3.3, investigating the impact of muons and pions on the early PNS deleptonization phase. In comparison with the reference case without muons and pions, no significant deviation could be found for the models including muons and pions for the first 20 s of the PNS deleptonization, independent on the treatment of pions.

The implementation of the axion losses in `AGILE-BOLTZTRAN` as sink term in the evolution equation for the internal energy, corresponding to the conservation of energy, is discussed in Ref. [145]. Here, the same approach is employed and we add to the previously included axion emission from nucleon-nucleon bremsstrahlung the updated rates as well as those from pions. Freely streaming axions are assumed. The axion emission rates will be introduced and discussed in the next section.

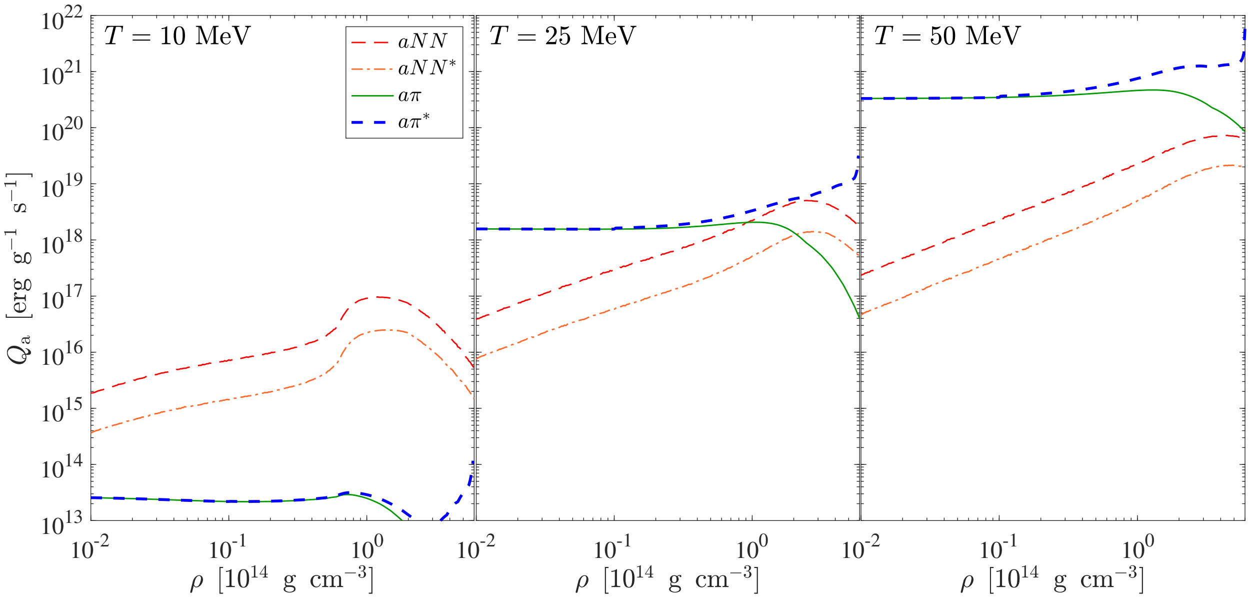

FIG. 21. Axion emissivities, Q_a, with respect to the restmass density for fixed electron and muon abundances of $Y_e = 0.3$ and $Y_\mu = 10^{-4}$ as well as for three selected temperatures of $T = 10$ MeV (left panel), 25 MeV (middle panel) and 50 MeV (right panel), comparing the bremsstrahlung rates aNN (thin red dashed lines) and aNN^* (thin orange dash-dotted lines) as well as axions stemming from pions $a\pi$ (thin green solid lines) and $a\pi^*$ (thick blue dashed lines).

5.3.2. Calculation of axion emission rates in simulation

At present, the process for axion emission in the context of core-collapse SN has long been the nucleon-nucleon bremstrahlung,

$$N + N \longrightarrow N + N + a \ . \tag{5.13}$$

The associated rate expression for the axion emissivity is a complicated high-dimensional momentum integral, involving the matrix elements with the yet incompletely known axion-nucleon coupling constant, g_{aN} (c.f. expression (2.2) and (2.6) in Ref. [99] and references therein). Previously employed simplifications, such as the vacuum one-pion exchange potential to describe the nuclear interactions and the assumption of massless pions, have lead to a simplified and semi-analytical expression for the axion emissivity [128, 168], henceforth denoted as aNN. This treatment was previously implemented in simulations of core-collapse SN [145]. It was found that aNN leads to an overestimation of the axion emission rate [99], which hence artificially enhances the axion losses in simulations of core-collapse SN. This caveat has been overcome with updated axion-emission rates derived in Ref. [99], henceforth
]

denoted as aNN^*. It includes a substantially improved description of the nuclear interactions, i.e. non-vanishing mass for the exchange pions, contributions from the two-pion exchange, effective in-medium nucleon masses and multiple nucleon scatterings effects, as well as the proper phase-space contributions including final-state Pauli blocking terms. The latter are realized numerically via a 64-point Gauss-quadrature integration. Note that the same nuclear model has been the foundation for the updated neutrino-pair emission and absorption rates from N–N bremsstrahlung [169]. Globally, they provide a substantial reduction of the axion emissivity with increasing density and temperature. Reference [119] implements the aNN^* treatment into the SN model `AGILE-BOLTZTRAN`, which is reproduced here. Together with the previously employed simplistic axion emissivity, aNN, this will allow us to quantify the impact of the medium modifications from the associated axion cooling contributions.

Another very efficient axion production mechanism is the pion Compton scattering,

$$\pi^- + p \longrightarrow n + a \ . \tag{5.14}$$

Reactions involving π^+ and π^0 are also possible but they are strongly suppressed compared to π^- since the abundances of π^+ and π^0 are negligible, as was discussed in sec. 5.3.1. The caveat of previous studies of axion emission from pions was the generally too low pion abundance, also for π^-, to be compatible with axions from nucleon-nucleon bremsstrahlung [146]. However, the medium-modified suppression of the bremsstrahlung rates lead to the revision of this argument [118]. The subsequent microscopic axion emission rate allows us to further support this argument, taking into account the treatment of interacting pions [26]. It results not only in the substantial enhancement of the pion abundances at high density but also in an axion emissivity which is compatible to those of the bremsstrahlung processes. The axion emissivities of Ref. [118] are included into `AGILE-BOLTZTRAN`, complementary to the bremsstrahlung rates.

Important here is the treatment of the interacting contributions to the pions consistently with the underlying HS(DD2) EOS used in the simulations. Therefore, the computation of the axion emissivity for the process (5.14) implements the pion dispersion relation (5.12), including the momentum dependent pion selfenergies (see Eq. (5.12) and Fig. 19). The axion emissivity through pion processes is henceforth denoted as $a\pi$, in the case of vanishing pion

TABLE VI. Summary of the different supernova simulations including the references to the various treatments for the calculation of the axion emissivity.

Label	$N + N \to N + N + a$	$\pi^- + p \to n + a$
ref. run (section 5.3.3)	—	—
aNN	vacuum one-π exchange, $m_\pi = 0$ [128, 145, 168]	—
aNN^*	improvements according to Ref. [99]	—
$aNN^* + a\pi$	“ ”	rates according to Ref. [118] with $\Sigma_\pi = 0$
$aNN^* + a\pi^*$	“ ”	“ ” with Σ_π according to Ref. [26]

interactions where we set $\Sigma_{\pi^-} = 0$, and as $a\pi^*$ in the general case of interacting pions.

Figure 21 compares the axion emissivity, denoted as Q_a, which is the rate devided by the restmass density and hence reflects the asymptotic behavior at low density which is proportional to the number density of targets, i.e. the abundance of π^- for the axions stemming from process (5.14) and NN pairs for the bremsstrahlung processes (5.13). The latter is similar as the low-density behavior of the neutrino pair production from nucleon-nucleon bremsstrahlung processes (see Fig. 3 in Ref. [170]). Guided by the previously revisited constraints for the axion-nucleon coupling constant [99], we choose here $g_{ap} = 1.2 \times 10^{-9}$ and $g_{an} = 0$ for the calculations of the axion emissivities for the reactions (5.13) and (5.14), since the same axion-nucleon coupling gives rise to the axion emission for the bremsstrahlung processes and the pion conversion. We will employ the same values for the coupling constants in the SN simulations, which will be discussed below in Sec. 5.3.4. Here, we compare the different treatments aNN and aNN^* for several temperatures, $T = 10$ MeV (left panel), 25 MeV (middle panel) and 50 MeV (right panel). From this analysis it becomes evident not only the strong temperature dependence of this axion emission process but also the substantial overestimation of the axion emissivity for the simplified treatment aNN. It is important to note that the different axion emissivities depend on the nuclear EOS, for which we use for the HS(DD2) EOS for all calculations and SN simulations.

Fig. 21 compares the bremsstrahlung rates with the axion emissivity from Compton pionic processes, for $a\pi$ (thin solid green lines) and $a\pi^*$ (thick blue dashed lines). There are several observations: (i) at low temperatures there is no significant axion emission, neither from bremsstrahlung nor stemming from pions, (ii) the overall low-density behavior reflects the

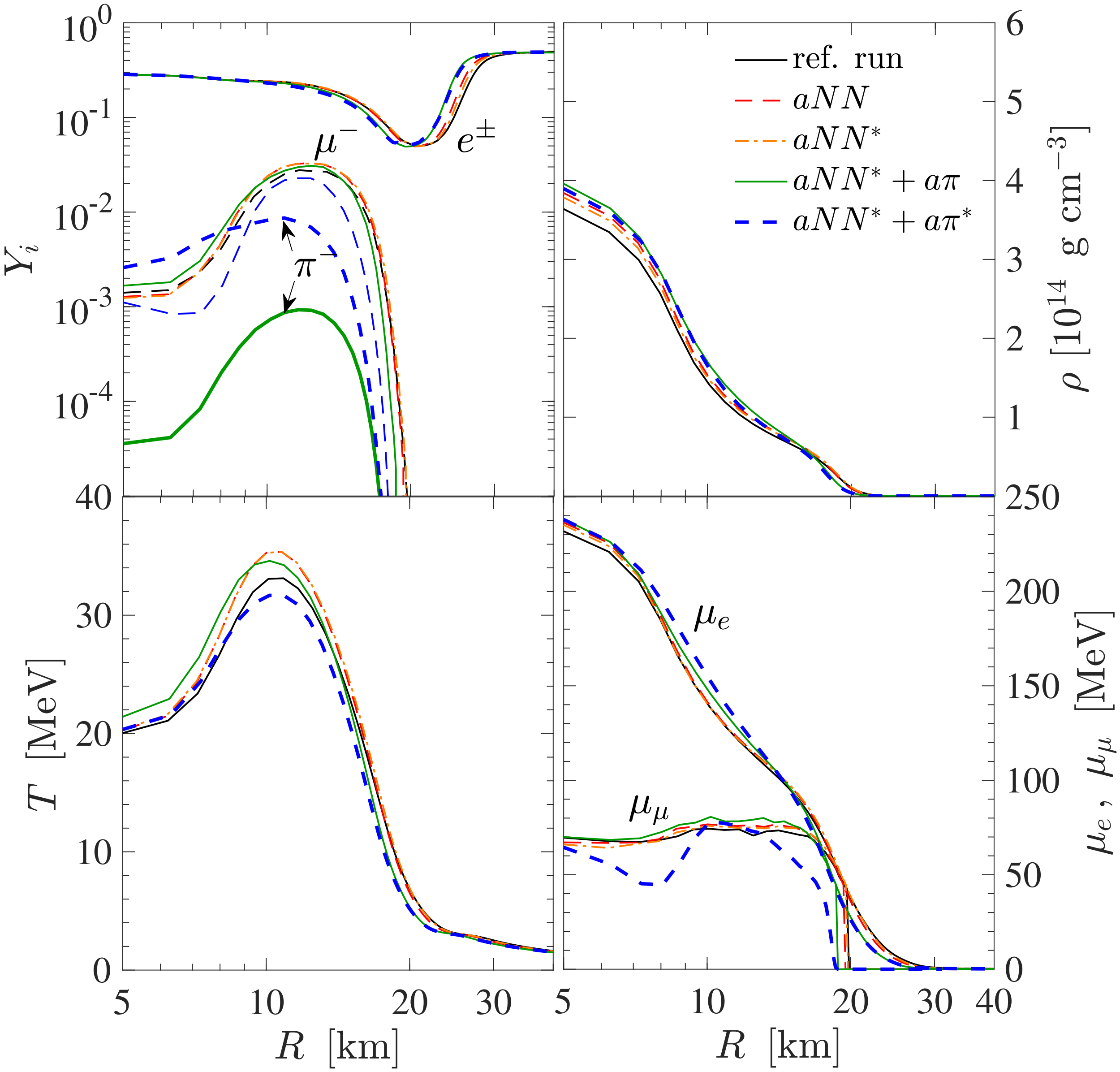

FIG. 22. Radial profiles of selected quantities, fractions of electrons (Y_e), muons (Y_μ) and pions (Y_{π^-}), temperature (T), restmass density (ρ) and the chemical potentials of electrons (μ_e) and muons (μ_μ) as well as the nuclear charge chemical potential ($\hat{\mu}$) at about 1 s post bounce during the early PNS deleptonization phase.

limiting dependence on temperature of the pion abundance, (iii) the match between $a\pi$ and $a\pi^*$ at low density as strongly interacting pions divert into non-interacting pions, and (iv) the substantial enhancement of the emissivity for $a\pi^*$ in comparison to $a\pi$ at a density in excess of $\rho \simeq 10^{14}$ g cm^{-3}, dominating the axion emission from pions over those of bremsstrahlung, however, only at high temperatures.

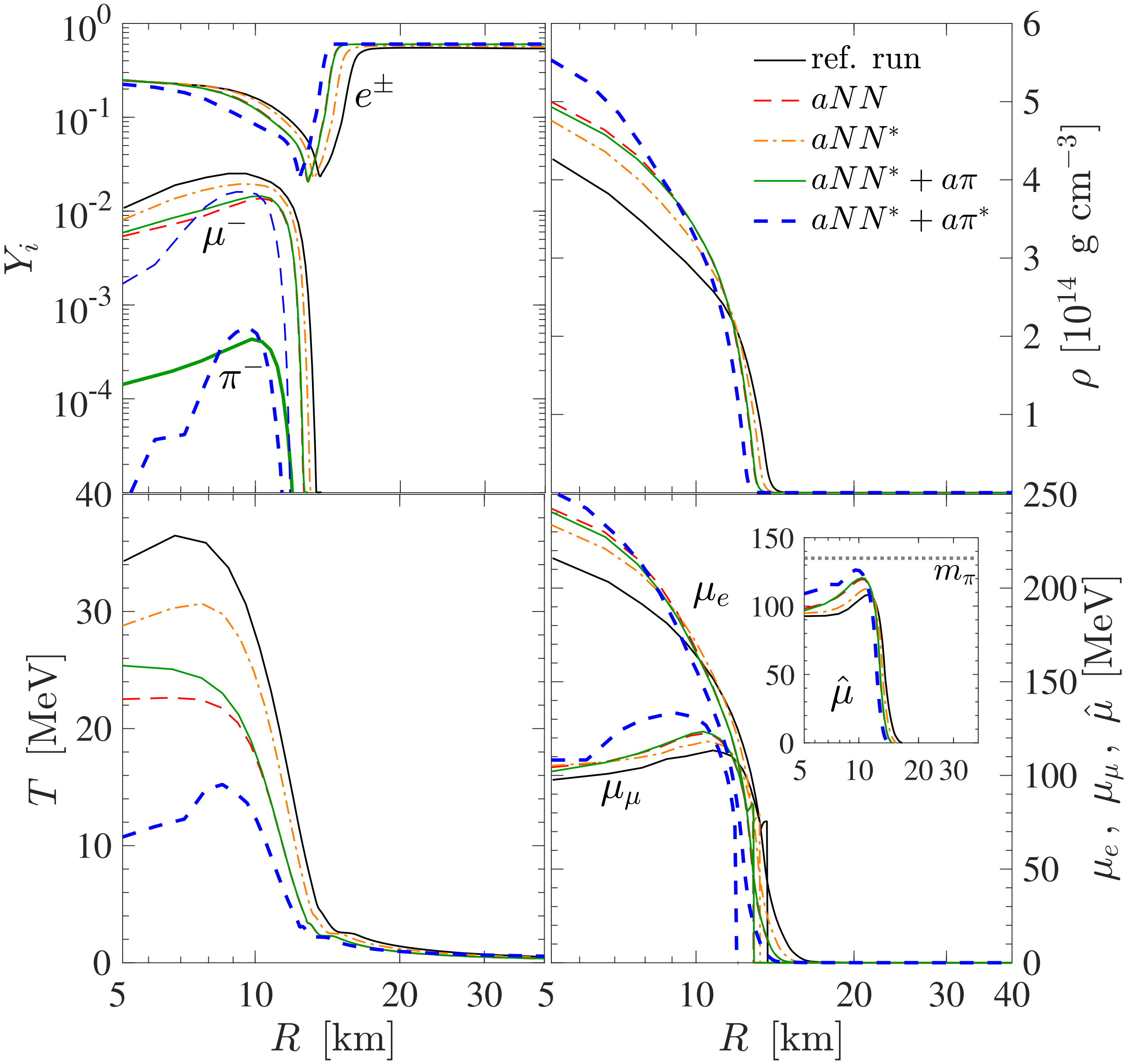

FIG. 23. The same as Fig. 22 but at about 7 s post bounce.

5.3.3. PNS deleptonization with muons and pions

A comparison is presented here for the simulations of the PNS deleptonization phase, comparing the following four different setups: *(i)* without muons and without pions, henceforth denoted as (no μ, no π), *(ii)* including muons and associated muonic weak processes but without pions, (μ, no π), *(iii)* with muons and non-interacting pions (no μ and π), and *(iv)* with muons and interacting pions following Ref. [26] (μ and π^*). The discussion about the implementation of the pions is given in Sec. 5.3.1, concerning both treatment for interacting and non-interacting pions. All simulations are based on the six-species Boltzmann neutrino

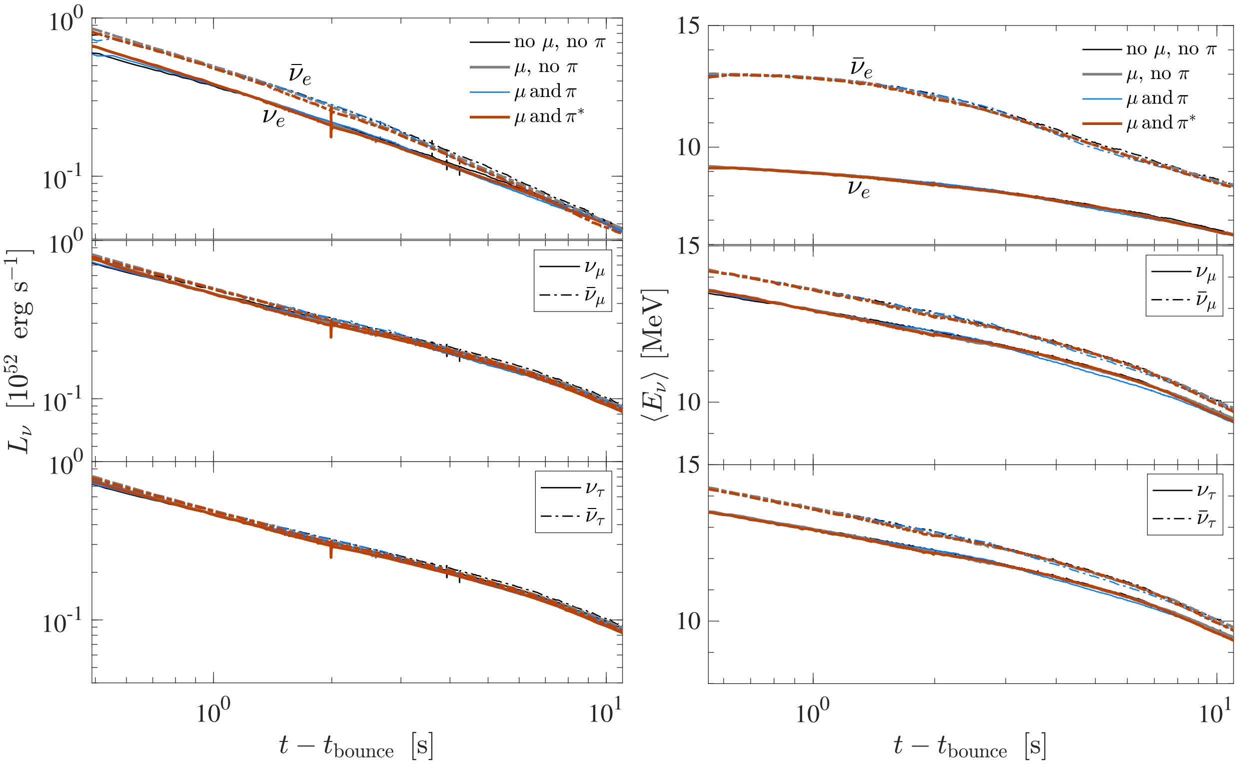

(a)

(b)

FIG. 24. Evolution of the neutrino luminosities and average energies sampled in the co-moving frame of reference at 500 km, comparing the simulations without muons and without pions (black lines) and including muons but no pions (grey lines), muons and non-interacting pions (blue lines) as well as muons and interacting pions (brown lines). All simulations employ the six-species neutrino transport scheme.

transport scheme of `AGILE-BOLTZTRAN` [136]. The standard set of weak reactions used here is listed in Table I of Ref. [154], including the corresponding references. Furthermore, we use the fully inelastic charged-current electronic and muonic rates of Ref. [153]. The latter include self consistent contributions of weak magnetism.

The SN simulations are launched from the 18 $M_\odot$ progenitor from the stellar evolution series of Ref. [171]. It has been evolved through all SN phases self consistently. Since the present focus is on the PNS deleptonization, and since neutrino-driven SN explosions cannot be obtained in spherical symmetry for this class of iron-core progenitors, we enhance the charged-current electronic weak reaction rates in the gain layer, applying the procedure introduced in the Refs. [152, 167]. It results in an explosion onset at about 350 ms post bounce, defined when the SN bounce shock reaches a radius of about 1000 km. Note that at that stage the enhancement of the charged-current weak rates is turned off and the standard

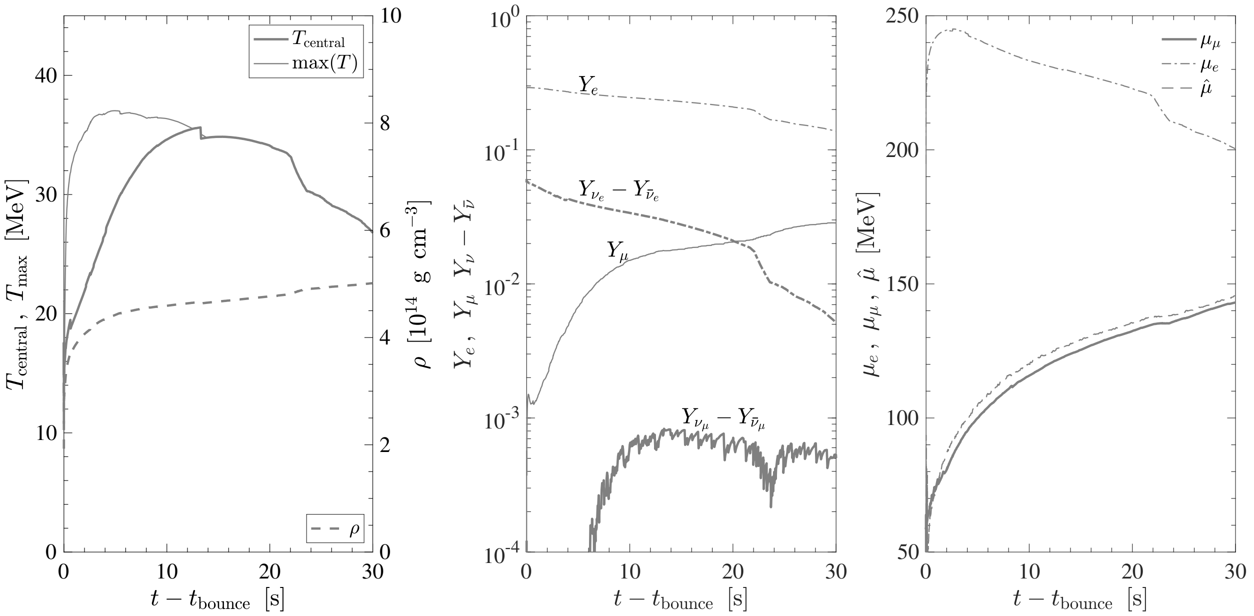

FIG. 25. Evolution of selected central quantities during the PNS deleptonization of the reference simulation including muons and associated muonic weak processes. *Left panel:* central temperature, T_{central} (thick solid line), in comparison to the maximum temperature, max(T) (thin solid line), and central density, ρ (dashed line). *Middle panel:* electron and muon abundances, Y_e (thin dash-dotted line) and Y_μ (thin solid line), and the net neutrino abundances for ν_e (thick dash dotted line) and ν_μ (thick solid line). *Right panel:* chemical potentials for muons, μ_μ (thick solid line), electrons, μ_e (thin dash-dotted line), and $\hat{\mu}$ (thin dashed lin).

weak rates setup is used again. The remnant PNS contain about 1.54 $\mathrm{M}_\odot$ of baryonic mass.

Figure 24(a) shows the resulting evolution of the neutrino luminosities and Fig. 24(b) shows the average energies, sampled in the co-moving frame of reference at a radius of 500 km. The simulations of the early PNS deleptonization phase, up to about 10 s post bounce, which include muons and associated muonic weak reactions [136, 153], show a negligible deviation from the reference setup without muons. This is attributed to two facts: (i) the early PNS deleptonization phase is governed by neutrino losses at the PNS surface where the neutrinospheres for all flavors are located, still at moderately low densities on the order of $< 10^{13}$ g cm-3, while muons are abundant at higher densities, and *(ii)* the abundance of muons is generally too low to leave a notable impact on the softening of the high-density EOS. We report that only at later times, $>$ 10 s post bounce, muons start to impact the PNS deleptonization and cooling, by means of an accelerated PNS compression.

A second set of simulations focuses on the role of pions. The latter are in thermal and chemical equilibrium. Note that only π^- are considered; π^+ and π^0 are strongly suppressed.

Here we consider non-interacting pions, which obey the standard thermal bosonic distribution, and interacting pions following Ref. [26]. The latter gives rise to a non-trivial pion dispersion relation featuring the pion selfenergy. The inclusion of non-interacting pions leaves a negligible impact on the early PNS deleptonization phase, for the same reasons *(a)* and *(b)* for muons aforementioned, and moreover, because the abundance of non-interacting pions is lower, by more than one order of magnitude, than the abundance of muons. The situation changes only marginally when considering interacting pions, whose abundance reaches, and even exceeds, those of the muons at the center of the PNS. However, their overall impact on the PNS structure and evolution during the early, about 1–10 s, PNS deleptonization remains negligible. An impact on the neutrino fluxes and spectra could not be found.

It is interesting to note that towards later times during the PNS deleptonization, on the order of 20–30 s, when the central temperature starts to decrease the simulation enters the cooling phase (see the left panel in Fig. 25). Relatedly, the central net neutrino abundance of the electron flavors starts to decrease. Furthermore, not that only after that, the chemical potentials of muons approaches the one of the electrons (see the right panel of Fig. 25), i.e. weak equilibrium will only be established at post bounce times greater than 30 s when $\mu_\mu \simeq \mu_e$.

5.3.4. PNS deleptonization with axions

The previous section contained a comparison of the PNS deleptonization with muons alone and in addition with pions with an overall negligible impact on the PNS structure and evolution of the neutrino luminosities and average energies. Here, we report about simulations of the PNS deleptonization including axions. We distinguish five different SN simulation setups: *(i)* the reference model without axions, *(ii)* including axion emission from only nucleon-nucleon bremsstrahlung at the vacuum one-pion exchange level employing the axion rates of Ref. [145], denoted as aNN and including all the improvements of Ref. [99] denoted as aNN^*, then further *(iii)* aNN^* plus axions stemming from non-interacting and *(iv)* interacting pions, henceforth denoted as $a\pi$ and $a\pi^*$, respectively. Table VI summarizes these different setups, including the labels used throughout the manuscript and the references for the different treatments concerning the calculations of the axion emissivity. Note that all simulations include muons and the associated muonic weak interactions, according to

Ref. [136].

Furthermore, having evolved our SN simulations consistently through all SN phases, we were able to assess that the axion losses do not have a significant impact prior to the SN explosion onset. Though axions are begin produced already slightly after core bounce from both channels (5.13) and (5.14), mainly because the material is shock heated as the bounce shock propagates outwards reaching temperatures on the order of 10 MeV, the axion luminosities remain negligible, on the order of at most $1 - 2 \times 10^{50}$ erg s^{-1} for the bremsstrahlung (depending only slightly on the treatment of the rates, aNN or aNN^*) and $1-10\times10^{49}$ erg s^{-1} for axions from pions, and are thus significantly below those of the neutrinos. During the post-bounce evolution, the continuous increase of the central density and temperature, due to the mass accretion onto the bounce shock from the still infalling material of the stellar progenitor, leads to the continuous rise of the axion luminosity. However, the axion luminosities never reach values compatible to those of the neutrinos and remain below 10^{51} erg s^{-1} for both bremsstrahlung and pion rates. Furthermore, the axion losses are dominated by bremsstrahlung processes during the post-bounce evolution. This is associated with the still generally low abundance of pions obtained during the entire post-bounce evolution, similar to those of muons. The finding that axion losses are negligible during the SN post-bounce evolution prior to the SN explosion onset is consistent with previous studies (cf. Ref. [145] and references therein).

The situation changes after the SN explosion onset, i.e. when the SN shock is accelerating to increasingly larger radii and when the central PNS enters the deleptonization and later Helmholtz cooling phase.

First, we consider the role of axion losses from bremsstrahlung processes (5.13). With the axion treatment aNN, at about 1 s post bounce differences are small compared to the reference simulation without axions (see Fig. 22). However, already at about 5 s post bounce the axion emission causes the PNS deleptonization evolution to accelerate in comparison to the reference case. The result is an enhanced deleptonization and hence compression of the PNS, featuring lower peak temperatures and a higher central density. However, the comparison of these results with the updated axion emissivity, aNN^*, clearly states a strong overestimation of the axion losses with respect to the simplified bremsstrahlung rates, aNN. The improved rates, aNN^*, leave a substantially weaker impact on the PNS deleptonization, as illustrated in Fig. 22 and 23 at two selected times during the PNS deleptnoization. Note

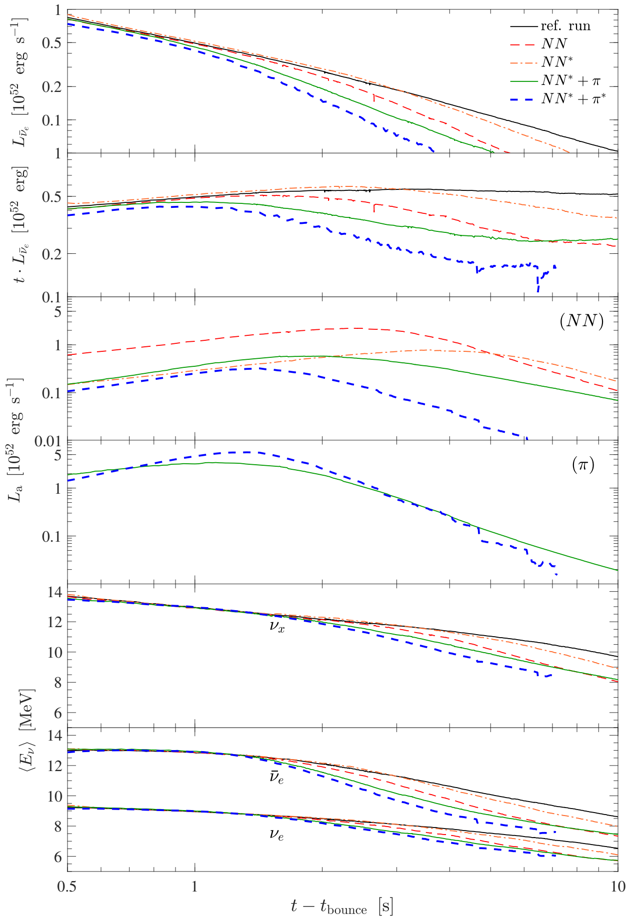

FIG. 26. Evolution of the $\bar{\nu}_e$ and axion luminosities, $L_{\bar{\nu}_e}$ and L_{a}, as well as the average neutrino energies $\langle E_\nu \rangle$ for all neutrino species (here we represent the heavy neutrino flavors collectively as $\nu_x = \nu_\mu$), sampled in the co-moving frame of reference at 500 km. For the axion luminosities we distinguish axions from nucleon-nucleon bremsstrahlung (5.13) (NN) and axions stemming from pion (π) processes (5.14).

the substantially slower deleptonization, given by a slower temperature drop, for aNN^* in comparison to aNN.

Consequently, the axion luminosity for aNN is substantially higher than for aNN^* by nearly one order of magnitude, as illustrated in Fig. 26. The associated accelerated PNS compression and cooling results in a shortening of the neutrino emission timescale. In turn, the neutrino luminosities and average energies of all flavors are reduced as soon as axion losses become significant. For the sake of simplicity, in Fig. 26 we show only the neutrino luminosity for $\bar{\nu}_e$, as those are the most relevant ones for possible detection prospects through the inverse β-decay, e.g., at the Super-Kamiokande detector [172]. The magnitude of the reduced neutrino emission timescale depends on the magnitdue of the axion emissivity; high rates, aNN, result in a more sever shortening which is substantially less pronounced for the updated and reduced rates, aNN^*. Note that the latter neutrino fluxes and average energies are nearly indistinguishable to the reference case without any axion losses, during the early PNS evolution.

Note further that since the nucleon-nucleon bremsstrahlung rates have a strong temperature dependence, their impact starts to decrease as the PNS interior cools (here, after about 5–10 s), the axion luminosity from bremsstrahlung drops and its impact on the enhanced cooling becomes negligible. After that, the PNS evolution is entirely governed by neutrino losses.

The inclusion of axion losses stemming from pions accelerates further the cooling of the PNS interior. Since shortly after the SN explosion onset the abundance of pions increases rapidly, the associated axion luminosity rises too. This is illustrated in Figs. 22 and 26 for the non-interacting pions (solid green lines), for which we set the pion selfenergy to zero. Since the axion luminosity from bremsstrahlung processes remains similar as for the simulation without pions included, also the impact on the PNS structure remains comparable (c.f. the central density at 7 s post bounce in Fig. 23). Only the central temperature is somewhat lower, indicating the additional impact from axion losses at the PNS interior from pions. Consequently, also the impact on the neutrino luminosities and average energies is comparable to the setup without axion losses stemming from non-interacting pions (see Fig. 26). The situation changes substantially when considering interacting pions (blue dashed lines in Figs. 22 and 23). The significantly higher abundance of π^- results in an enhanced axion luminosity, which, in turn, leads to an accelerated PNS cooling. This is illustrated via the significantly lower temperatures at the PNS interior already at about 7 s in Fig. 23. Correspondingly, the faster PNS compression leads to higher central densities. However, the faster temperature drop feeds back to a faster drop of the pion abundance, which still exhibits a strong temperature dependence. Hence, also the axion luminosities drop faster as illustrated in Fig. 26 (blue dashed lines), and the impact from axion losses on the neutrino emission terminates earlier than for the case with non-interacting pions (solid green lines). Nevertheless, the lower neutrino luminosities obtained together with the reduced average neutrino energies, in particular during the early PNS deleptonization phase, at about 2–5 s, may leave interesting prospects for the neutrino detection. In particular we find that the luminosity power law, $L \propto t^{-1} \exp\{-(t/\tau)^{\alpha}\}$ [173] with characteristic cooling timescale τ and parameter $\alpha \simeq 2.5$, changes substantially. This is illustrated when considering the quantity $t \cdot L_\nu$ in Fig. 26, which indicates that when considering additional losses, the neutrino losses cannot be considered constant. The latter is the case only for the standard reference setup, during the early PNS deleptonization phase up to about 10 s post bounce.

5.3.5. Observable signatures

In this Section we discuss the possible observable signatures of axion emission in SN, especially focusing on the case of pionic processes. A first study considering only bremsstrahlung processes was presented in Ref. [100], which we follow closely. In the following, we will show how the modification of the SN neutrino signal, due to the emission of axions, would affect the observable neutrino signal in large underground detectors. For definiteness we focus on the future-generation Hyper-Kamiokande water Cherenkov detector, planned in Japan with a fiducial mass of 260 kton [174]. When needed, we will also show, for comparison, results from the current Super-Kamiokande neutrino detector, for which we assume a mass of 32 kton.

The neutrino event rate, N_e, at Earth can be expressed symbolically as follows [175],

$$N_e = F_\nu \otimes \sigma_e \otimes R_e \otimes \varepsilon \ , \tag{5.15}$$

where the neutrino flux at Earth is convoluted with the interaction cross section, σ_e, in the detector for the production of an electron or a positron, as well as the energy-resolution function, R_e, of the detector and the detection efficiency, ε. The threshold of the experiment is $E_{\text{th}} = 5$ MeV. For simplicity, in the following we will neglect the effect of energy-dependent features. Moreover we assume $\varepsilon = 1$ above the threshold.

Concerning the detected neutrino fluxes, notably they are affected by peculiar flavor conversion effects. Their characterization is far from being settled due to peculiar effects in the SN interior, associated with neutrino–neutrino interactions and with matter turbulence (for a review about SN neutrino oscillation effects, see Ref. [176]). Furthermore, we are mostly interested in the PNS deleptonization phase ($t \gtrsim 1$ s) after which the spectra of all neutrino flavors become increasingly similar [167], which in turn reduced the impact of flavor conversions on the observable signal. Therefore, for simplicity, we will neglect also

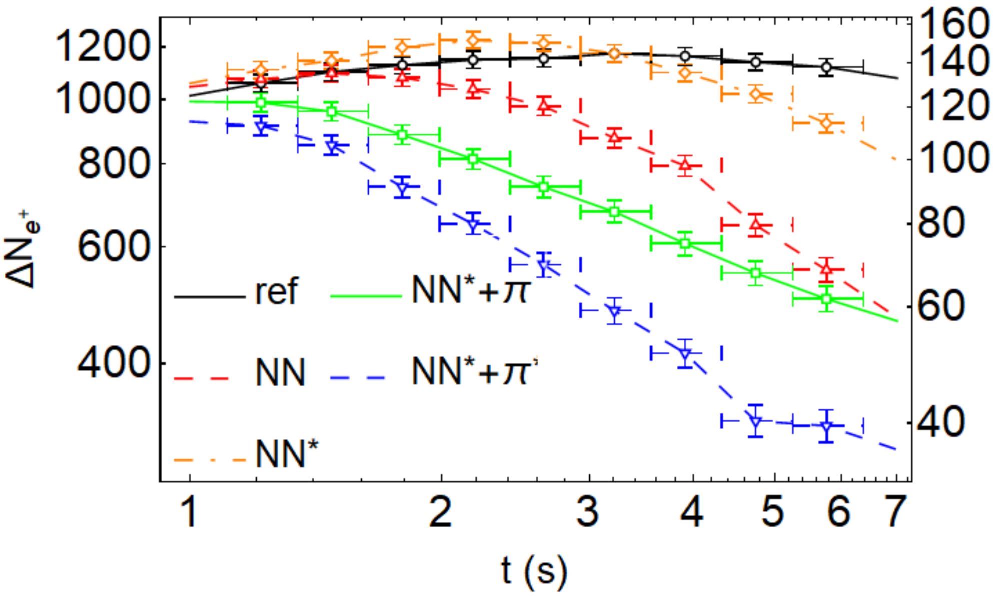

FIG. 27. Count rate in each log-time bin for $\bar{\nu}_e$ in the Hyper-Kamiokande (left scale) and Super-Kamiokande detectors (right scale) due to the inverse-beta interaction for the different scenarios discussed in sec. 5.3.4. The vertical error bars show the Poisson uncertainties on the counts in Hyper-Kamiokande and the horizontal error bars show the bin widths.

these effects, assuming un-oscillated neutrino spectra at Earth.

Water-Cherenkov detectors are mostly sensitive to SN electron antineutrinos through the inverse beta decay process, $\bar{\nu}_e + p \to n + e^+$, which we characterize from Ref. [177]. In the following, we assume a fiducial SN at a distance $d = 10$ kpc.

In Fig. 27 we show the $\bar{\nu}_e$ event rate in the Hyper-Kamiokande detector (left scale) due to the inverse-beta interaction for the different scenarios discussed in sec. 5.3.4 (see Fig. 26). For comparison, the right scale refers to the events rate in the Super-Kamiokande detector. In particular, following [173] we adopt a log scale for the time-axis, choosing 10 equal-width bins per factor of ten in time. Indeed, using a logarithmic time-axis, one can use the following algebraic relation, $dA/dt = dA/d\,\mathrm{ln}t = (2.3)^{-1} dA/d\log_{10} t$. Therefore, Fig. 27 shows $\Delta N = (2.3)^{-1} dN/d\log_{10} t$. We see that in the reference run without axion emission (black line), the behavior of ΔN is rather constant with time, for the interval considered here. Including axion emission from bremsstrahung process in the aNN treatment, would cause a fast drop already at $t \gtrsim 2$ s, leading to a reduction by a factor of about two of the signal at $t \sim 7$ s. The updated bremsstrahlung rate aNN^* has a considerably reduced impact and the complete run becomes nearly indistinguishable from the reference one. Differences become visible only at $t \gtrsim 4$ s, reducing the signal by a factor of about 1.2 with respect to

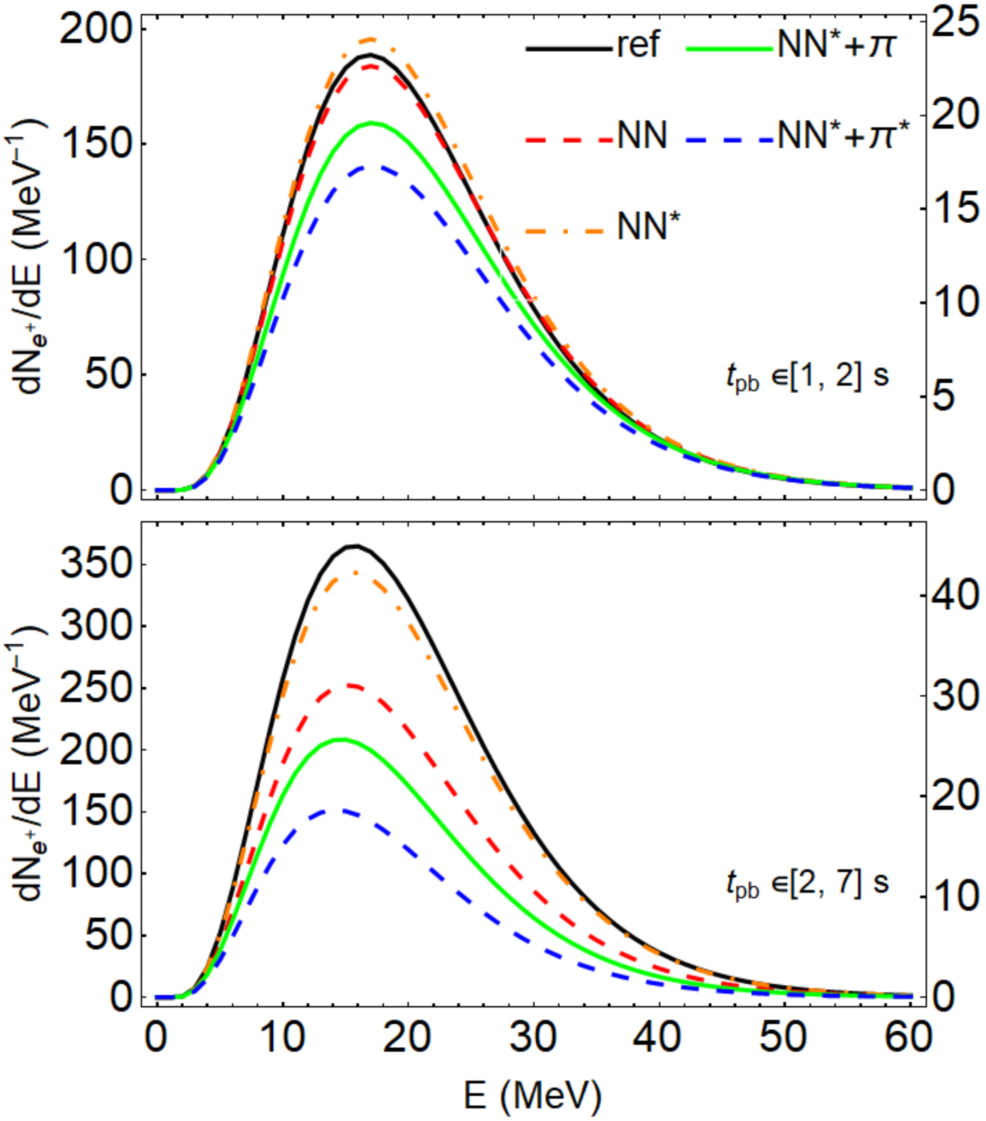

FIG. 28. Positron spectra in the Hyper-Kamiokande (left scale) and Super-Kamiokande detectors (right scale) in selected time ranges, between $1-2$ s (upper panel) and $2-7$ s (bottom panel) for the models discussed in sec. 5.3.4.

the reference case. If we now include the pionic process, the drop of the neutrino event rate becomes dramatic, being evident with respect to the reference case already at about $t \gtrsim 1$ s. In the case of non-interacting pions $a\pi$ the final reduction of the signal is comparable to what is obtained with aNN bremsstrahlung process. However, the drop of the signal is faster at early times. Including interacting pions, $a\pi^*$, features an even more dramatic drop of the event rate at early times, resulting in a reduction by a factor of 3 at $t \sim 7$ s with respect to the reference case.

Figure 28 shows the detectable positron spectra for the different models considered, integrating the signal in two time-windows, namely $t \in [1;2]$ s (upper panel) and $t \in [2;7]$ s (lower panel), respectively. We see that at early times the effect of axion emission is marginal in the case of only bremsstrahung processes, regardless of weather the rate is corrected (aNN^*) or not (aNN). On the other hand, in the presence of pionic processes the suppression of the positron spectrum already shows a reduction of a factor about 1.6 at the peak with respect to the reference case, for the interacting pion scenario $a\pi^*$. In the second, later time window the effect of the suppression of the positron spectrum is more remarkable, except in the case of aNN^*, which remains nearly indistinguishable in comparison to the reference case. On the other hand, we find a reduction of the peak of the spectrum of a factor of about 3 in the case of interacting pions $a\pi^*$.

A further signature of the axion emission would be the impact on the SN binding energy, E_B, carried by neutrinos. Note that the axion emission would lead to a reduction of the SN binding energy. This effect is illustrated in Fig. 29, where we show the evolution of the energy carried away to infinity by neutrinos of all flavors (top panel) and axions, distinguishing bremsstrahlung processes (middle panels) and pionic processes (bottom panel), for the different scenarios discussed above. Note that the early and sudden rise of the energy carried by neutrinos is due to the contributions from the stellar core collapse, bounce and early post-bounce phases prior to the SN explosion onset, during which all simulations are identical and during which we did not find any impact from the inclusion of axions.

We realize that in the case of bremsstrahlung processes the energy carried by axions rises continuously, as indicated by the slowly increasing temperature at the PNS centre where most axions are being produced from bremsstrahlung processes. When the temperature starts to decrease, the axion emissivity decreases simultaneously, which is the case at around 5 s for aNN and only at around 10 s for aNN^*. The total energy carried away is similar for aNN and aNN^*, however, both of their magnitudes, 8×10^{52} erg and 4×10^{52} erg respectively, are much lower than that of neutrinos, i.e. neutrinos dominate the losses during the PNS deleptonization phase. In particular, the weak feedback for aNN^* leaves nearly no difference notable in the energy carried away by neutrinos, in comparison to the reference case.

Contrarily, in the case of pionic processes a substantially larger fraction of the binding energy, comparable to the energy carried by neutrinos, is carried by axions already at early times. However, the associated rapid cooling contributions lead to a fast reduction of the PNS interior temperature, which in turn result in a faster drop of the axion emissivity.

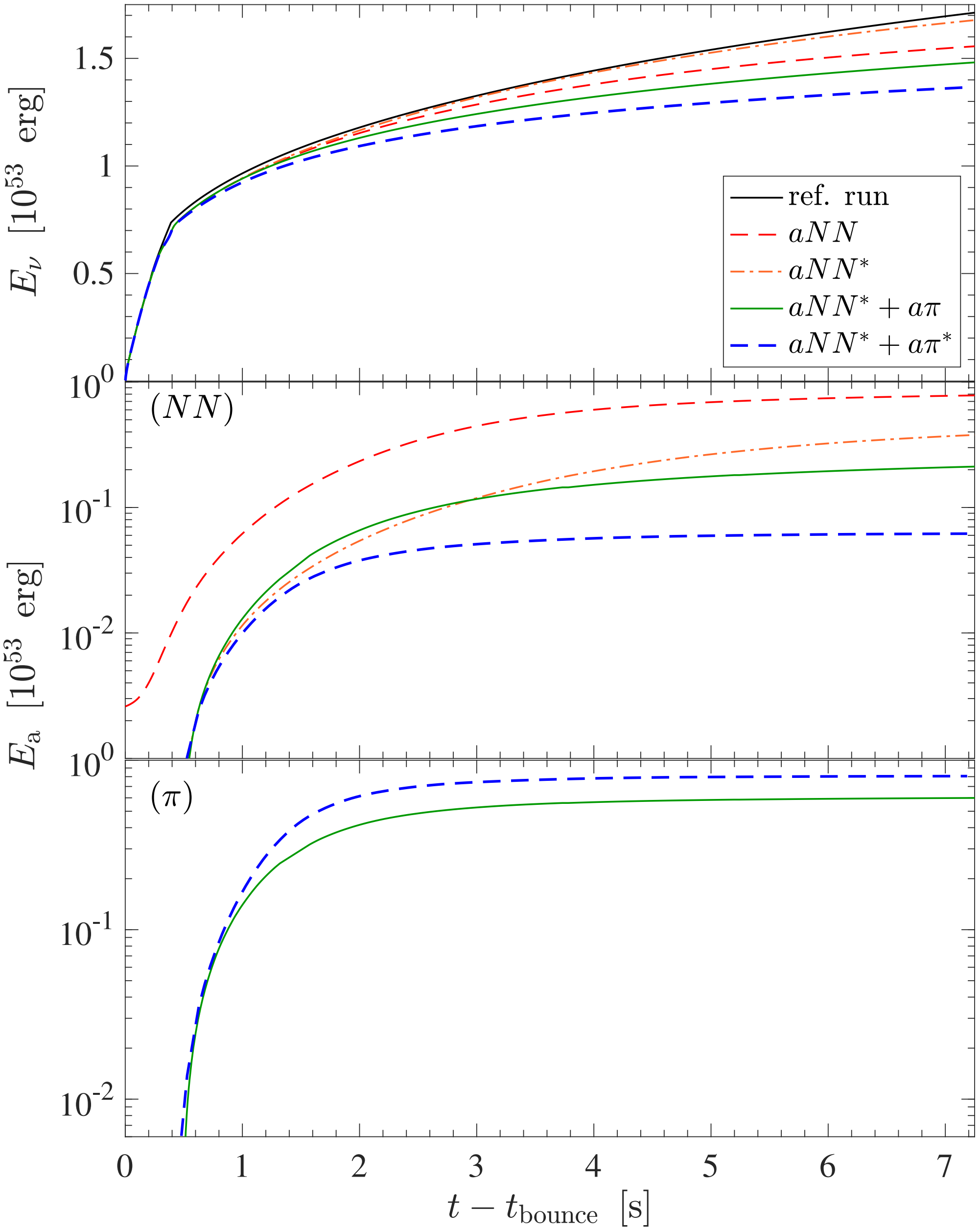

FIG. 29. Evolution of the SN binding energy carried by neutrinos (upper panel) and axions due to nucleon-nucleon bremsstrahlungs processes (middle panel) and stemming form pions (lower panel), for the scenarios discussed in Sec. 5.3.4.

Hence, the process of energy loss through axions stemming from pionic processes ceases much earlier compared to the case of from bremsstrahlung processes. Consequently, the impact on the total energy carried by neutrinos is small, a factor of about 1.3 at 7 s. The total energy carried away by neutrinos and axions is listed in Table VII, evaluated at about 20 s post bounce for the different simulations. While for the axion losses the asymptotic values have been reached within the first 7 s after bounce, for the neutrino losses we extrapolate

TABLE VII. Total energy carried away by neutrinos, L_ν, and axions, $L_{\rm a}$, evaluated at a post-bounce time of 20 s.

Model	E_ν [10^{53} erg]	$E_{\rm a}^{NN}$ [10^{53} erg]	$E_{\rm a}^{\pi}$ [10^{53} erg]
ref.	2.2	—	—
aNN	1.8	0.88	—
aNN^*	2.0	0.58	—
$aNN^* + a\pi$	1.7	0.29	0.79
$aNN^* + a\pi^*$	$1.5^\dagger$	0.06	0.81

†: asymptotic values extrapolated assuming monotonously decreasing neutrino luminosities for all flavors beyond 7 s post bounce evolution

assuming monotonously decreasing neutrino luminosities of all flavors.

What is described above are all indirect signatures of the axion effects in a SN. However, a direct detection of SN axions is perhaps also possible. To explore this intriguing possibility, in Fig. 30 we show the axion spectrum, integrated over the entire PNS profile, for the bremsstrahlung and pionic processes, distinguishing non-interacting pions and strongly interacting pions, evaluated at different post-bounce times. Two features are clearly visible in the pion-induced axion spectrum: *i)* the energy threshold at the pion mass and *ii)* the energy peak at $\sim$ 150–200 MeV. Both features can be understood from the kinematics of the process (5.14). Assuming equal mass of protons and neutrons, it is evident that the minimal axion energy corresponds to the minimal pion energy, hence with its mass. This is true also when the pion interactions are turned on, and the pion dispersion relation is corrected with Σ_{π^-} (cf. Eq. (5.12) and Fig. 19). The higher threshold moves also the peak energy to higher values with respect to the bremsstrahlung process.

Notice also that the modified dispersion relation (5.12), with Σ_{π^-} becoming increasingly more negative at large momenta, which in turn makes it more expensive to increase the pion energy. Since the axion energy in the reaction (5.14) is controlled by the pion energy (the nucleons are much heavier), this reflects in a narrower axion spectrum when the pion interactions are turned on ($\Sigma_{\pi^-} \neq 0$). This feature is clearly evident in the spectra in Fig. 30 (cf. the green line, which shows the axion spectrum for non-interacting pions, with the blue dashed line, for which the interactions are turned on).

It is also apparent that at early times, when the PNS is still hot and rather dilute with large radii, the axion spectra can have extended tails up to 1 GeV. It was estimated in Ref. [118] that for a close-by SN, i.e. $d \lesssim 1$ kpc, and a Mton-class water Cherenkov

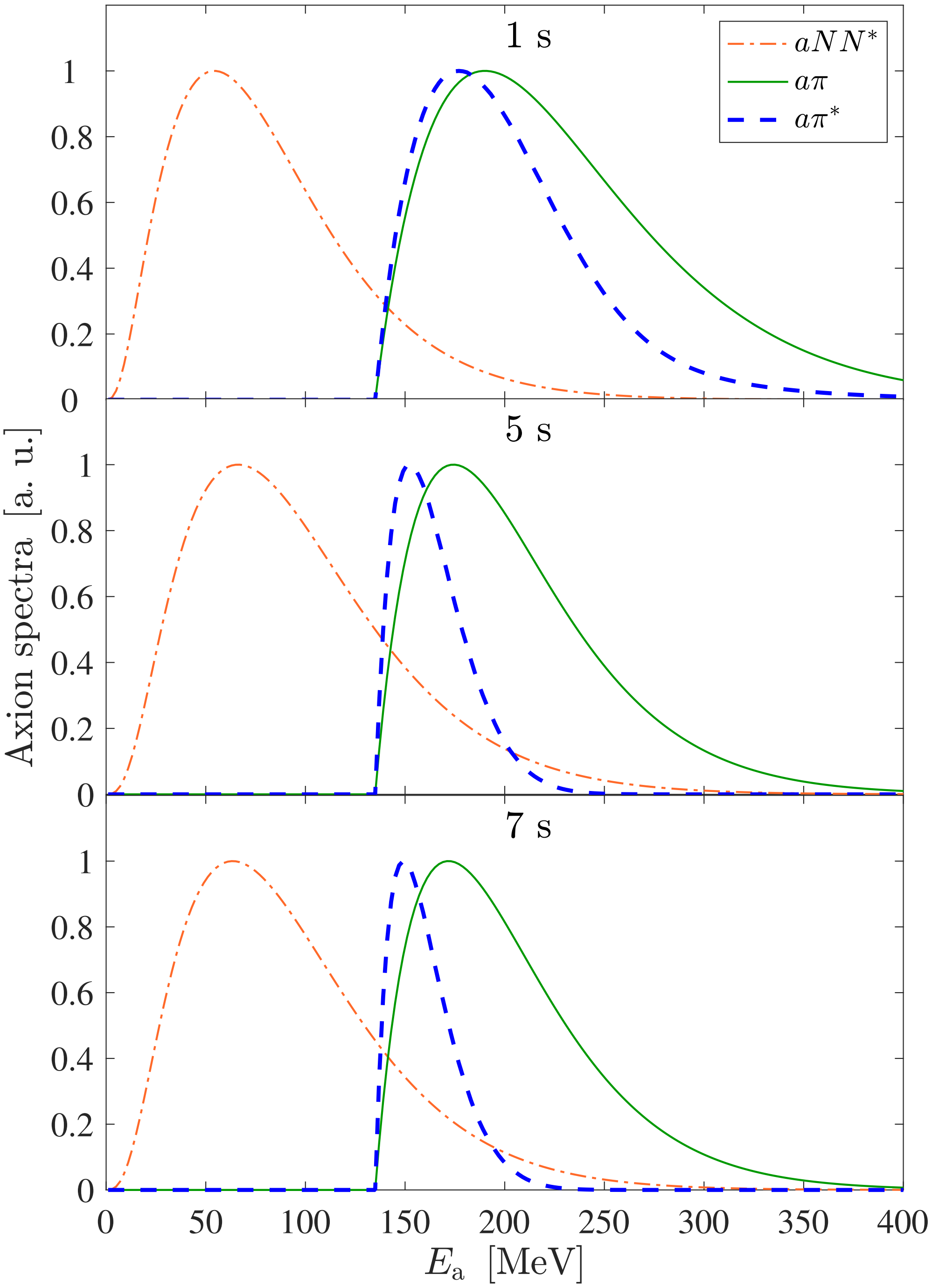

FIG. 30. Normalized axion emission spectra for nucleon-nucleon bremsstrahlung processes (light red dash-dotted lines) and for axions stemming from non-interacting pions (solid green lines) and interacting pions (thick blue dached lines), at different post-bounce times 1 s (top panel), at 5 s (middle panel) and at 7 s (bottom panel), corresponding to the SN simulations discussed in sec. 5.3.4.

underground detector, this axion burst would be detectable through the processes, $a + N \to N + \pi$, giving an unexpected signal of $\mathcal{O}(10^3)$ pions during a SN emission. The detection of this pionic signal, together with a rapid drop of the neutrino signal, would be a strong evidence for the axion emission via pionic processes.

5.3.6. Summary of results from supernova simulation with updated axion emission

Results are reported from simulations of the PNS deleptonization phase of core-collapse SN, launched from a progenitor of 18 $M_\odot$ [171], where in addition to the neutrinos, axions and the associated energy losses are considered. The SN simulations are based general relativistic neutrino radiation hydrodynamics in spherical symmetry, employing six-species Boltzmann neutrino transport. The restriction to spherical symmetry is justified for the PNS deleptonization phase of a core-collapse SN, since the compact central remnant PNS obeys spherical symmetry. The description of approximate convection can be implemented in such spherically symmetric models [178]. All present simulations include muons as additional degree of freedom, and the associated muonic weak processes [136, 153].

In a first step, updated nucleon-nucleon bremsstrahlung rates for the axion emissivity are considered [99]. These yield a substantial reduction of the previously reported shortening of the neutrino emission timescale [145], which adopted the simplified bremsstrahlung vacuum rate expressions based on the one-pion exchange approximation. In a second step, the inclusion of pions enables us to extend the previous studies including axions stemming from pions. This novel channel has long been omitted, due to the shortcoming of a generally negligible pion abundance. Considering interacting pions, however, relaxes this argument. Then, the inclusion of axion cooling from this channel significantly shortens the timescale of neutrino emission as a direct feedback, in comparison to the case when only bremsstrahlung processes are considered.

The resulting SN simulation neutrino signals are then further analysed with respect to the detection prospects at the future-planned Hyper-Kamiokande and presently operating Super-Kamiokande water-Cherenkov detectors. We find that the sudden drop of the count rate implies the presence of additional, non-standard energy losses, that could be related with axions originating from pions due to Compton processes, if occurring during the early phase of detection.

Furthermore, according to the recent study of Ref. [179], a measurement of the binding energy of less than 1.5×10^{53} erg carried by neutrinos, would be strong evidence for the presence of exotic energy-losses. It would be otherwise incompatible with SN models for different neutron star mass and EOS. An experiment like Hyper-Kamiokande has the potential to measure the total neutrino energy with an accuracy of few % [180], allowing us to diagnose with accuracy the presence of an additional energy-loss.

Note that the uncertainty due to the elastic approximation, i.e. zero nucleon recoil, implemented for the calculation of the emissivity of axions stemming from pions, is unlikely to alter the findings of the present work. Even though this gives rise to a sharp cut of the rate given by the pion rest mass, the high-energy tail of the axion spectrum dominates the phase space integrals and hence the axion emissivity.

It is important to note that all these results, as well as those reported in Ref. [136], with a negligible impact of muons and associated muonic weak processes during the SN bounce and early post-bounce evolution, are based on the HS(DD2) relativistic mean-field EOS. It represents a stiff nuclear model at densities in excess of saturation density.

These findings, e.g., the negligible impact from the inclusion of muons and pions reported here, may alter when adopting a softer nuclear EOS, i.e. when higher central densities are encountered (see Refs. [1, 102, 160] and the left panel of Fig. 25 in section 5.3.3). This yet-incompletely understood aspect remains to be explored in a more systematic fashion. Besides the uncertainty of the EOS in terms of bulk properties, there are other aspects that are likely to affect the signal proposed here, e.g., impact of the EOS on the neutrino opacity, PNS convection and fall back. All this remains to be explored in a systematic fashion.

We note further that magnetic fields are not considered here, due to the restriction to spherical symmetry. The magnetic field can be large at the interior of PNS [181, 182], which is usually associated with magneto-rotationally driven SN explosions [183, 184], giving rise to the formation of magnetars—an observationally known class of highly magnetized neutron stars with surface magnetic field on the order of 10^{15} Gauss. This is still an active subject of research, in particular regarding the development of jets in the context of core-collapse SNe [185, 186], especially the magnitude of the initial progenitor magnetic field strength and the possible amplification during the SN evolution. Furthermore, it is expected that strong magnetic field affect the emission of axions [187, 188]. An interesting possibility is the possible mixing of the axions with photons [189], for which it has been demonstrated recently that the axion mixing with the photon longitudinal mode is suppressed for light axions due to the electron degeneracy [190]. The only possibility is the mixing with the photon transverse mode which requires the photon mass to match the axion mass. Hence, in the present study we consider light axions for which the mean free path is large compared to the PNS radius, even in the presence of large magnetic fields. Revisiting the impact of magnetic fields in details would extend beyond the scopes of the present study, which identifies possibly observable signatures during the PNS deleptonization, that originate from enhanced cooling contributions associated with axion emission. We postpone the full study of magnetic fields impact on SN axions to a future work, which must include self-consistently the effect of magnetic fields not only on the axion emission but also on the PNS structure and the associated neutrino emission.

6. S-WAVE PION CONDENSATION IN NEUTRON STARS: A REAPPRAISAL

Bose-Einstein condensation of pions in dense nuclear matter was studied extensively in the 1970s. In pioneering work, Sawyer and Scalapino proposed the idea that pion condensation might lower the energy of dense nuclear matter at high density [36, 191, 192]. In subsequent years, several authors studied its manifestation and implications for nuclei and neutron stars in some detail using simple models for the pion-nucleon interaction [35, 38, 39, 193–197]. Pion condensation occurs at low temperatures when the energy to produce a pion is less than its associated chemical potential. Earlier work has addressed the possibility of condensation of negatively charged pions in neutron stars because the chemical potential for negative charge, which we denote throughout as $\hat{\mu}$, increases with density, and is typically in the range $100 - 300$ MeV in the neutron star core. In the absence of interactions, a pion condensate with zero momentum will occur when $\hat{\mu} \geq m_\pi$, where $m_\pi \simeq 140$ MeV is the mass of the pion. However, repulsive s-wave interactions between π^- and neutrons were shown to increase the pion energy in neutron stars and were believed to disfavor condensation of zero-momentum pions. Consequently, most early studies of the π^- condensation addressed the possibility of realizing a condensate at *finite* momentum. The strongly attractive p-wave interaction between pions and nucleons was shown to favor condensation of pions with momentum $k_\pi \simeq m_\pi$ and lead to a non-uniform ground state [195]. In the 1980s, more sophisticated model-dependent analyses including many-body corrections and correlations between nucleons at short-distances found that even p-wave condensation may not be robust at the densities encountered in neutron stars (for a comprehensive review see [198]).

In this article we revisit s-wave pion condensation in neutron star matter, and explore whether the s-wave repulsion is large enough to robustly preclude pion condensation. This study is primarily motivated by the fact that Chiral Perturbation Theory (χPT) now affords a more systematic approach to study pion-nucleon interactions than the methods used in the 1970s, and by the observation that pion condensation in the density interval $1-3$ $n_{\rm sat}$, where $n_{\rm sat}=0.16$ nucleons/fm^3 is the nuclear saturation density, can have important consequences for the neutron star structure and cooling. In particular, condensation's impact on the equation of state (EOS) can alter the radius of a canonical neutron star with mass $M\simeq 1.4\,{\rm M}_\odot$, and its impact on the proton fraction can influence neutron star cooling (for a recent review see [199]).

In this section, we explore the possibility of s-wave π^- condensation in neutron stars by adopting and improving upon the systematic calculations of the pion self-energy in dense asymmetric nuclear matter using χPT outlined in Refs. [45, 200]. We focus on s-wave condensation and defer a study of p-wave condensation for several reasons. First, the p-wave interaction between pions and nucleons is stronger and more complex because of the $\Delta-$resonance, and the perturbation theory we employ here will be inadequate. Second, measurements of energy levels of pionic atoms constrain the predictions of χPT for the s-wave pion self-energy at baryon density $n_B\lesssim n_{\rm sat}$ and finite isospin asymmetry [200].

The material in this section is organized as follows. In Section 6.1 we describe our two-loop χPT calculation of the pion self-energy in asymmetric dense matter. In Section 6.2 we present a parametric model adequate to account for the strong interactions of nucleons and study the model's effect on the pion self-energy. We also calculate in Section 6.2 the critical density for s-wave condensation and determine its sensitivity to model parameters. In Section 6.3 we calculate the equation of state of dense nuclear matter containing a pion condensate and study its implications for neutron stars. Finally, in Section 6.4 we provide a brief summary of our findings and discuss some of its limitations.

6.1. π^- self-energy in neutron-rich matter

The energy of a negatively charged pion at rest in dense nuclear matter, denoted by ω_{π^-}, is obtained by solving

$$\omega_{\pi^-}=\sqrt{m_\pi^2+\Pi(\omega_{\pi^-})}\,, \tag{6.1}$$

where $\Pi(\omega_{\pi^-})$ is the self-energy of a zero-momentum pion due to its strong interactions. To calculate $\Pi(\omega_{\pi^-})$ we will need a description of pion-nucleon, pion-pion, and nucleon-nucleon interactions. Chiral Perturbation Theory offers a systematic framework to describe pion-pion and pion-nucleon interactions at low energies. This effective field theory organizes all operators consistent with chiral symmetry as a derivative expansion, and is expected to be reliable when the pion and nucleon momenta and energies are much smaller than $\Lambda \simeq 4\pi f_\pi \simeq 1$ GeV, where $f_\pi = 92.4$ MeV is the pion decay constant.

The energy and momentum scales relevant to our calculation are set by the pion energy $\omega = \hat{\mu} \simeq m_\pi$, and the nucleon momentum $k_\mathrm{F} \simeq (3\pi^2 n_B)^{1/3} \simeq 330(n_B/n_\mathrm{sat})^{1/3}$ MeV, respectively. When these are small compared to Λ, χPT can be used to calculate the pion self-energy. In what follows we calculate $\Pi(\omega_{\pi^-})$ by retaining terms up to order k_F^5 and $\omega_{\pi^-}^2$. For this purpose, it is adequate to work with the following heavy-baryon Lagrangian [34, 201]

$$\mathcal{L}_\pi = \mathcal{L}_{\pi\pi}^{(0)} + \mathcal{L}_{\pi N}^{(0)} + \mathcal{L}_{\pi N}^{(1)} + \mathcal{L}_{\pi NN}^{(1)} \,, \tag{6.2}$$

where the superscript denotes the Chiral dimension $\Delta = d + \frac{1}{2}n - 2$; here d is the number derivatives and/or insertions of the pion mass, n is the number of nucleon field operators, and the subscript specifies the particle fields involved.

Interactions between pions at leading order are given by

$$\mathcal{L}_{\pi\pi}^{(0)} = \frac{f_\pi^2}{4} \langle \partial_\mu U \partial^\mu U^\dagger + \chi_+ \rangle \,. \tag{6.3}$$

Here, the pion fields are contained in

$$U = \exp\left(\frac{i}{f} \begin{bmatrix} \pi^0 & \sqrt{2}\pi^+ \\ \sqrt{2}\pi^- & -\pi_0 \end{bmatrix} \right) ,$$

$\chi_+ = m_\pi^2(U + U^\dagger)$, and the symbol $\langle\cdot\rangle$ denotes a trace over flavor degrees of freedom. Interactions between pions and nucleons at leading order are given by

$$\mathcal{L}_{\pi N}^{(0)} = \bar{N}\big(iv\cdot D + g_A u \cdot S\big) N \,, \tag{6.4}$$

where v_μ is the four-velocity of the nucleon field, $g_A = 1.267$ is the axial-vector coupling constant, and where the following symbols are defined:

$$\begin{aligned}
\xi^2 &= U \\
D_\mu &= \partial_\mu + \frac{1}{2}[\xi^\dagger, \partial_\mu \xi] \\
u_\mu &= i(\xi^\dagger \partial_\mu \xi - \xi \partial_\mu \xi^\dagger) \\
S^\mu &= \frac{i}{2}\gamma_5 \sigma^{\mu\nu} v_\nu \\
\sigma^{\mu\nu} &= \frac{i}{2}[\gamma^\mu, \gamma^\nu] \,.
\end{aligned}$$

Seven operators contribute to the Lagrangian at next-to-leading order (NLO) [201], however we display here only those operators contributing to the self-energy of a zero-momentum pion in the absence of external fields:

$$\mathcal{L}^{(1)}_{\pi N} = \bar{N}\left(c_1\langle\chi_+\rangle - \frac{c_2}{8M^2}\Big(\langle u_\mu u_\nu\rangle\{D_\mu, D_\nu\} + h.c.\Big) + \frac{c_3}{2}\langle u^2\rangle\right) N \,. \tag{6.5}$$

Here the c_i's are low-energy constants (LEC's). Pions also couple to a two-nucleon current at NLO. This interaction is described by

$$\mathcal{L}^{(1)}_{\pi NN} = \frac{D}{2}\left(\bar{N}N\right)\ \left(\bar{N}\ u\cdot S\ N\right) \,. \tag{6.6}$$

The LEC D is typically decomposed as

$$D = \frac{c_D}{f_\pi^2 \Lambda_\chi} \,, \tag{6.7}$$

where $\Lambda_\chi \simeq 700$ MeV is the chiral symmetry breaking scale. The interaction in Eq. 6.6 contributes to the three-nucleon force, and the c_D has been determined using the triton binding energy and the neutron-deuteron doublet scattering length [202]. Its value is sensitive to the regularization scheme and the choice of the momentum cut-off. For momentum-space cut-offs between $500 - 600$ MeV, c_D falls in the range $-1 - 4$ [202].

The Feynman diagrams contributing to the pion self-energy at two-loop order are shown in Fig. 31. Kaiser & Weise [45], and Kolomeitsev, Kaiser & Weise [200] have calculated the contributions due to the diagrams labelled (ld), $(\tilde{ds})$, (ph), and (cr). The diagram labelled

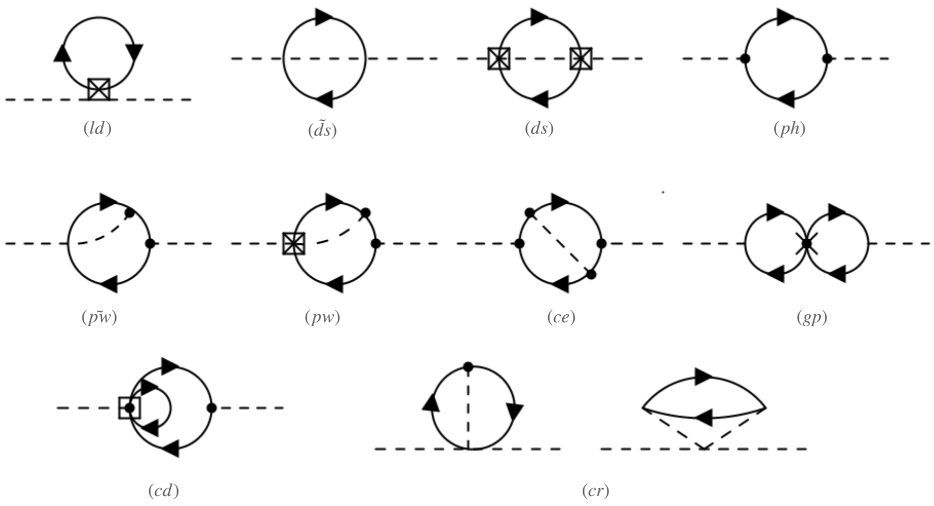

FIG. 31. Feynman diagrams that contribute to the pion self-energy. Solid-lines represent nucleons, dashed-lines represent pions. There are several types of vertices: the Weinberg-Tomozawa interaction vertex is un-decorated, the dot represents the pion-nucleon axial vertex, the hatched-box represents T-matrix insertions, the open-box is the pion coupling to two nucleons, and the cross-dot indicates a short-distance nucleon-nucleon interaction.

(ld) includes contributions linear in the nucleon density, and is given by

$$\Pi_{ld}(\omega_{\pi^-}) =$$

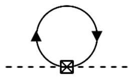

$$= T^-(\omega_{\pi^-})\ \frac{(k_{\rm Fn}^3 - k_{\rm Fp}^3)}{3\pi^2} - T^+(\omega_{\pi^-})\ \frac{(k_{\rm Fn}^3 + k_{\rm Fp}^3)}{3\pi^2}\ , \tag{6.8}$$

where $k_{\rm Fn}$ and $k_{\rm Fp}$ are the neutron and proton Fermi momenta and where $T^-(\omega_{\pi^-})$ & $T^+(\omega_{\pi^-})$ are the off-shell s-wave isospin-odd and isospin-even scattering amplitudes, respectively. The isospin-odd amplitude, up to order ω_π^3, is given by

$$T^-(\omega_{\pi^-}) = \frac{\omega_{\pi^-}}{2f_\pi^2} + \frac{\gamma\omega_{\pi^-}^3}{8\pi^2 f_\pi^4} - \frac{\omega_{\pi^-}^2 Q}{8\pi^2 f_\pi^4}\ \left(\ln\left[\frac{\omega_{\pi^-}+Q}{m_\pi}\right] - i\frac{\pi}{2}\right)\ , \tag{6.9}$$

where $Q = \sqrt{\omega_{\pi^-}^2 - m_\pi^2}$, $\gamma = \pi^2 g_A^2 f_\pi^2/M^2 + \ln\left[2\Lambda/m_\pi\right]$, and where Λ is chosen such that the empirical value $T^-(m_\pi) = 1.85$ fm is obtained. The leading term of T^-, first predicted by Weinberg and Tomozawa [203, 204], is remarkably close to the empirical value, and Chiral Perturbation Theory converges rapidly. In contrast, the convergence of $T^+(\omega_{\pi^-})$ is known to be poor. Up to order ω_π^3, it is given by

$$T^+(\omega_{\pi^-}) = \frac{\sigma_N - \beta\omega_{\pi^-}^2}{f_\pi^2} + \frac{3g_A^2 m_\pi^3}{16\pi f_\pi^4} + \frac{3g_A^2 m_\pi Q^2\zeta}{64\pi f_\pi^4} + i\frac{\omega_{\pi^-}^2 Q}{8\pi f_\pi^4}\ , \tag{6.10}$$

where $\sigma_N = -4c_1 m_\pi^2 - 9g_A^2 m_\pi^3/64\pi f_\pi^2$ is the pion-nucleon sigma term [205] and $\beta = -2(c_2 + c_3) + g_A^2/4M$. In Ref. [200] the low-energy constant c_1 is chosen to reproduce $\sigma_N \simeq 45 \pm 15$ MeV, the range probed by phenomenological and lattice calculations [206, 207], and the combination $c_2 + c_3$ is determined by the empirical value $T^+(m_\pi) = 0$. The parameter ζ encodes the freedom associated with choosing the interpolating pion field. Its value is scheme dependent and affects other low-energy constants in the χPT and needs to be fixed by fits to data. In Ref. [200], the authors set $\zeta = 0$ to ensure that the residue at the pole of pion propagator in vacuum is one. However, these choices introduce systematic uncertainties because the convergence of the χPT expansion for $T^+(\omega_{\pi^-})$ is not well-understood. To incorporate this uncertainty, and assuming that $Q^2 \ll m_\pi^2$, we rewrite the scattering amplitude as

$$\tilde{T}^+(\omega_{\pi^-}) = -\frac{\tilde{\sigma}}{f_\pi^2}\,\frac{Q^2}{m_\pi^2}\,, \tag{6.11}$$

where $\tilde{\sigma} \simeq \sigma_N$, is treated as model parameter with values in the range $40 - 80$ MeV. Later, we will use constraints on the π^- optical potential in ^{208}Pb to justify this choice.

The contribution from the 2-loop diagram labelled $\widetilde{ds}$ accounts for double-scattering due to the Weinberg-Tomozawa interaction and is given by

$$\Pi_{\widetilde{ds}} =$$

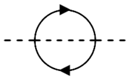

$$= \frac{\omega_{\pi^-}^2}{3(4\pi f_\pi)^4}\left(L(k_{\rm Fn},k_{\rm Fn},Q) + L(k_{\rm Fp},k_{\rm Fp},Q) + 2L(k_{\rm Fn},k_{\rm Fp},Q)\right)\,, \tag{6.12}$$

where

$$\begin{aligned} L(k_{\rm Fp},k_{\rm Fn},Q) &= 4k_{\rm Fn}k_{\rm Fp}(3(k_{\rm Fn}^2 + k_{\rm Fp}^2) + Q^2) + 8Q(k_{\rm Fn}^3 - k_{\rm Fp}^3)\ln\frac{Q + k_{\rm Fn} - k_{\rm Fp}}{Q - k_{\rm Fn} + k_{\rm Fp}} \\ &\quad - 8Q(k_{\rm Fp}^3 + k_{\rm Fn}^3)\ln\frac{Q + k_{\rm Fn} + k_{\rm Fp}}{Q - k_{\rm Fn} - k_{\rm Fp}} \\ &\quad + (3(k_{\rm Fp}^2 - k_{\rm Fn}^2)^2 + 6Q^2(k_{\rm Fp}^2 + k_{\rm Fn}^2) - Q^4)\ln\frac{(k_{\rm Fp} - k_{\rm Fn})^2 - Q^2}{(k_{\rm Fp} + k_{\rm Fn})^2 - Q^2}\,. \end{aligned} \tag{6.13}$$

for $\omega_{\pi^-} > m_\pi$. The diagram labelled (ds) includes higher order contributions to double-scattering. This contains contributions up to order $\omega_{\pi^-}^3$ that were included in the off-shell scattering amplitudes T^+ and T^- defined earlier. Including these contributions, we find that

$$\Pi_{ds} =$$

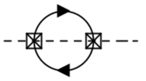

$$= \frac{1}{192\pi^4}\Big[T_{nn}(\omega_{\pi^-})^2 L(k_{\rm Fn},k_{\rm Fn},Q) + T_{pp}(\omega_{\pi^-})^2 L(k_{\rm Fp},k_{\rm Fp},Q) + T_{np}(\omega_{\pi^-})^2 L(k_{\rm Fn},k_{\rm Fp},Q)\Big] , \quad (6.14)$$

where $T_{nn}(\omega_{\pi^-}) = T^+(\omega_{\pi^-}) - T^-(\omega_{\pi^-})$, $T_{pp}(\omega_{\pi^-}) = T^+(\omega_{\pi^-}) + T^-(\omega_{\pi^-})$, and $T_{np}(\omega_{\pi^-}) = -\sqrt{2}T^-(\omega_{\pi^-})$.

The particle-hole diagram (labelled (ph) in Fig. 31) contains the contribution due to the axial current interaction between nucleons and pions. Since the pion momentum is zero, its contribution appears as relativistic correction suppressed by the factor $v_F^2 = k_{\rm F}^2/M^2$, and is given by

$$\Pi_{ph}(\omega_{\pi^-}) =$$

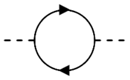

$$= -\frac{g_A^2\omega_{\pi^-}}{f_\pi^2}\left(\frac{k_{\rm Fn}^5 - k_{\rm Fp}^5}{10\pi^2 M^2}\right) . \quad (6.15)$$

This diagram is also suppressed in systems with small isospin asymmetries. For these reasons, Π_{ph} is relatively unimportant in the analysis of pionic atoms [200]. However, as we demonstrate later, this diagram makes a relevant contribution to the pion self-energy in neutron stars.

The 2-loop diagram labelled (pw) includes the attractive p-wave pion-nucleon interaction in the intermediate state. In Fig. 31 we only show one of several possible intermediate states. Others are obtained by connecting the p-wave vertex to the lower Fermion line and by switching the location of the Weinberg-Tomazawa vertex. The intermediate pion can be either neutral pion or a charged pion. We have calculated the contribution from all of these diagrams, and their sum is given by

$$\Pi_{\widetilde{pw}}(\omega_{\pi^-}) = \sum$$

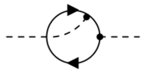

$$= -\left(\frac{\omega_{\pi^-}}{2f_\pi^2}\right)\left(\frac{g_A^2}{2Mf_\pi^2}\right)\Big[2\Big\{I(\omega_{\pi^-};k_n,k_n) - I(\omega_{\pi^-};k_p,k_p) + K(\omega_{\pi^-};k_n,k_p)\Big\} + \Big\{I(0;k_n,k_n) - I(0;k_p,k_p) + K(0;k_n,k_p)\Big\}\Big] \quad (6.16)$$

where the sum indicates a sum over all possible arrangements of the Weinberg-Tomazawa and dotted vertices, and where I and K are given by the following integrals

$$\begin{aligned} I(\omega; A, B) &= \int \frac{d^3l d^3k}{(2\pi)^6} \theta(A-l)\theta(B-k) \frac{(l-k)^2}{(l-k)^2 + m_\pi^2 - \omega^2 - i0^+} \, , \\ K(\omega; A, B) &= \int \frac{d^3l d^3k}{(2\pi)^6} \theta(A-l)\theta(B-k) \frac{2(l^2-k^2)}{(l-k)^2 + m_\pi^2 - \omega^2 - i0^+} \, . \end{aligned} \tag{6.17}$$

We provide useful formulae to calculate I & K in the appendix.

It is straightforward to include higher-order ω_{π^-} terms contributing to the (pw) diagram. The net effect of inserting further pion-nucleon vertices is to replace the WT vertex by the off-shell amplitudes, as was obtained in Eq. 6.14 for the double-scattering contribution. This also allows for the incorporation of the isospin-even contributions, and we find

$$\Pi_{pw}(\omega_{\pi^-}) = \sum$$

$$\begin{aligned} = &- 2T^-(\omega_{\pi^-}) \left(\frac{g_A^2}{2Mf_\pi^2}\right) \Big[\Big\{ I(\omega_{\pi^-}; k_n, k_n) - I(\omega_{\pi^-}; k_p, k_p) + K(\omega_{\pi^-}; k_n, k_p) \Big\} \\ &\qquad + \frac{1}{2} \Big\{ I(0; k_n, k_n) - I(0; k_p, k_p) + K(0; k_n, k_p) \Big\} \Big] \\ &+ 2T^+(\omega_{\pi^-}) \left(\frac{g_A^2}{2Mf_\pi^2}\right) \Big[I(\omega_{\pi^-}; k_n, k_n) + I(\omega_{\pi^-}; k_p, k_p) - I(\omega_{\pi^-}; k_n, k_p) \Big] \, . \end{aligned} \tag{6.18}$$

where again the sum indicates a sum over all possible arrangements of vertices.

The contributions due to diagrams labelled (cr) have also been calculated and are found to be negligibly small (the analytic expressions can be found in Ref. [200]). We have calculated the contribution due to the diagram (ce) and find that its contribution is also negligible. We therefore neglect both in our analysis.

The contribution to the self-energy due to the two-nucleon current $\mathcal{L}_{\pi NN}^{(1)}$ is

$$\Pi_{cd}(\omega_{\pi^-}) = 2 \times$$

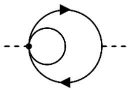

$$= -\frac{g_A c_D \omega_{\pi^-}}{f_\pi^4 \Lambda_\chi} \left(\frac{k_{\mathrm{Fn}}^3 + k_{\mathrm{Fp}}^3}{3\pi^2}\right) \left(\frac{k_{\mathrm{Fn}}^5 - k_{\mathrm{Fp}}^5}{10\pi^2 M^2}\right) \, , \tag{6.19}$$

and appears at order $k_{\mathrm{F}}^8 \omega_{\pi^-}$. At this order, other diagrams contribute that we are not including. We retain this diagram only to study the sensitivity to higher order corrections and to the low-energy constant c_D.

Th pion self-energy at two-loop order is obtained by summing over the individual contributions

$$\Pi_{\rm tot}(\omega_{\pi^-}) = \Pi_{ld}(\omega_{\pi^-}) + \Pi_{ds}(\omega_{\pi^-}) + \Pi_{ph}(\omega_{\pi^-}) + \Pi_{pw}(\omega_{\pi^-}) + \Pi_{cd}(\omega_{\pi^-})\,. \tag{6.20}$$

At the typical densities and isospin asymmetries encountered inside nuclei, the most relevant contributions are due to the terms linear in density and the double-scattering diagram. For example, for $k_{\rm Fn} = 280.5$ MeV and $k_{\rm Fp} = 243$ MeV which approximately correspond to the ambient conditions in the central regions of ^{208}Pb, the individual contributions from the diagrams are listed in Table VIII. The numerical values in the table are obtained by setting $\tilde{\sigma} = 60$ MeV, and $c_D = 1$. Since Π_{ld} and Π_{ds} make the dominant contributions, below we shall use pionic atom data to constrain the range for the parameter $\tilde{\sigma}$ defined in Eq. 6.11.

ω_{π^-}	$\Pi_{ld}/2m_\pi$	$\Pi_{ds}/2m_\pi$	$\Pi_{ph}/2m_\pi$	$\Pi_{pw}/2m_\pi$	$\Pi_{cd}/2m_\pi$
m_π	8.8 MeV	7.5 MeV	-0.96 MeV	-0.76 MeV	-0.16 MeV
165 MeV	23.0 MeV	9.5 MeV	-1.14 MeV	-1.3 MeV	-0.18 MeV

TABLE VIII. Contributions from the individual diagrams to the pion self-energy at $k_{\rm Fn} = 280.5$ MeV and $k_{\rm Fp} = 243$ MeV. We have used $\tilde{\sigma} = 60$ MeV, and $c_D = 1$.

Experimentally measured energy levels of pionic atoms provide useful constraints on the π^- optical potential in neutron-rich heavy-nuclei such as Pb. In the local density approximation, the optical potential at the center of the pionic atom is related to the local pion self-energy : $V_s = \Pi_{\rm tot}(\omega - V_C, k_{\rm Fn}, k_{\rm Fp})/2\omega$, where $\omega = m_\pi - B$, B is the binding energy, and V_C is Coulomb potential at the center of the nucleus, and $k_{\rm Fn}, k_{\rm Fp}$ are the local neutron and proton Fermi momenta, respectively [200]. Phenomenological fits to data suggest that the s-wave component of the π^-optical potential at the center of ^{208}Pb, which we denote as $V_s(^{208}\text{Pb})$, is in the range 28 ± 3 MeV [208, 209].

In Table IX we present our results for the optical potential for several values of $\tilde{\sigma}$ obtained using our two-loop calculation of the π^- self-energy. These values are obtained by assuming that at the center of ^{208}Pb, the baryon density $n_B = 0.16$ fm^{-3}, and the proton density

$\tilde{\sigma}$	40 MeV	50 MeV	60 MeV	70 MeV	80 MeV
$V_s(^{208}\text{Pb})$	24.1 MeV	26.0 MeV	27.9 MeV	29.7 MeV	31.6 MeV

TABLE IX. S-wave optical potential at the center of ^{208}Pb. Pionic atoms data indicate that $V_s \simeq 28 \pm 3$ MeV [209].

$n_p = 0.063$ fm^{-3}. We also assumed that $B \simeq 7$ MeV for the ^{1}S state, and $V_C \simeq -29$ MeV. From Table IX we can conclude that experimental constraints on the π^- optical potential require $\tilde{\sigma}$ to be the range 45 − 75 MeV. We note that if one assumes that $\tilde{\sigma} \approx \sigma_N$, recent analysis of pion-nucleon scattering data that favor $\sigma_N \simeq 60$ MeV [210] is contained in our range for $\tilde{\sigma}$.

6.2. Symmetry energy and π^- condensation in neutron star matter

Dense matter in neutron stars is electrically neutral and in equilibrium with respect to weak interactions. To ensure this, the electron chemical potential $\mu_e = \hat{\mu}$ increases with density and acts as a source for negatively charged particles. π^- condensation becomes energetically favorable when $\mu_e \geq \omega_{\pi^-}$, and the critical density, n_c, for the second-order phase transition is determined by solving

$$\mu_e(n_c) = \sqrt{m_\pi^2 + \Pi_{\rm tot}(\mu_e(n_c))}\,. \tag{6.21}$$

The discussion in the preceding section showed that the pion self-energy depends sensitively on the pion energy and on the individual Fermi momenta of neutrons and protons. The rate at which μ_e increases with density plays a crucial role in determining n_c and is sensitive to interactions between nucleons. It is largely determined by the nuclear symmetry energy

$$S(n_B) = E(n_B, x = 0) - E(n_B, x = 1/2)\,, \tag{6.22}$$

where $E(n_B, x)$ is the energy per baryon at baryon density n_B and proton fraction $x = n_p/n_B$. Microscopic calculations and fits to phenomenological models indicate that the energy per particle at arbitrary proton fraction is well-approximated by

$$E(n_B, x) \approx E(n_B, x = 1/2) + S(n_B)(1 - 2x)^2\,, \tag{6.23}$$

since higher order terms in the expansion have been found to be small, even for $x \ll 1/2$ [211]. In this case, the electron chemical potential in neutron star matter is

$$\mu_e(n_B) = 4S(n_B)(1 - 2x)^2\,. \tag{6.24}$$

The proton fraction x also increases with density, and is calculated self-consistently to ensure electric charge neutrality, i.e., $n_e + n_\mu = n_p$, where $n_e = (\mu_e^2 - m_e^2)^{3/2}/3\pi^2$, and $n_\mu = (\mu_e^2 - m_\mu^2)^{3/2}/3\pi^2$ when $\mu_e > m_\mu$, are the electron and muon number densities, respectively.

Recently, there has been much interest in determining the density dependence of the symmetry energy. Despite progress in both theory and experiment, this dependence remains poorly known at densities reached in neutron stars. In the vicinity of nuclear saturation density, $S(n_B)$ impacts nuclear structure. Nuclear masses, measurements of the neutron-skin thickness, and the electric-dipole polarizability of neutron-rich nuclei such as ^{208}Pb provide useful constraints on $S_0 = S(n_{\rm sat})$. Its density dependence is characterized by the parameter $L = 3n_{\rm sat}\left(dS(n_B)/dn_B\right)_{n_B=n_{\rm sat}}$ [31]. Until recently, experiments, when combined with theoretical models, suggested the empirical range $S_0 = 32 \pm 2$ MeV and $L = 50 \pm 15$ MeV. Theoretical calculations using nucleon-nucleon interactions determined by χEFT predict S_0 and L compatible with this empirical range. For example, a recent calculation that combines many-body perturbation theory (MBPT) and Bayesian estimates for the truncation errors predicts $S_0 = 31.7 \pm 1.1$ MeV and $L = 59.8 \pm 4.1$ MeV [212]. However, the recent measurement of the neutron-skin thickness of ^{208}Pb using parity violating electron scattering imply larger values: $S_0 = 38.1 \pm 4.7$ MeV, and $L = 106 \pm 37$ MeV [213, 214].

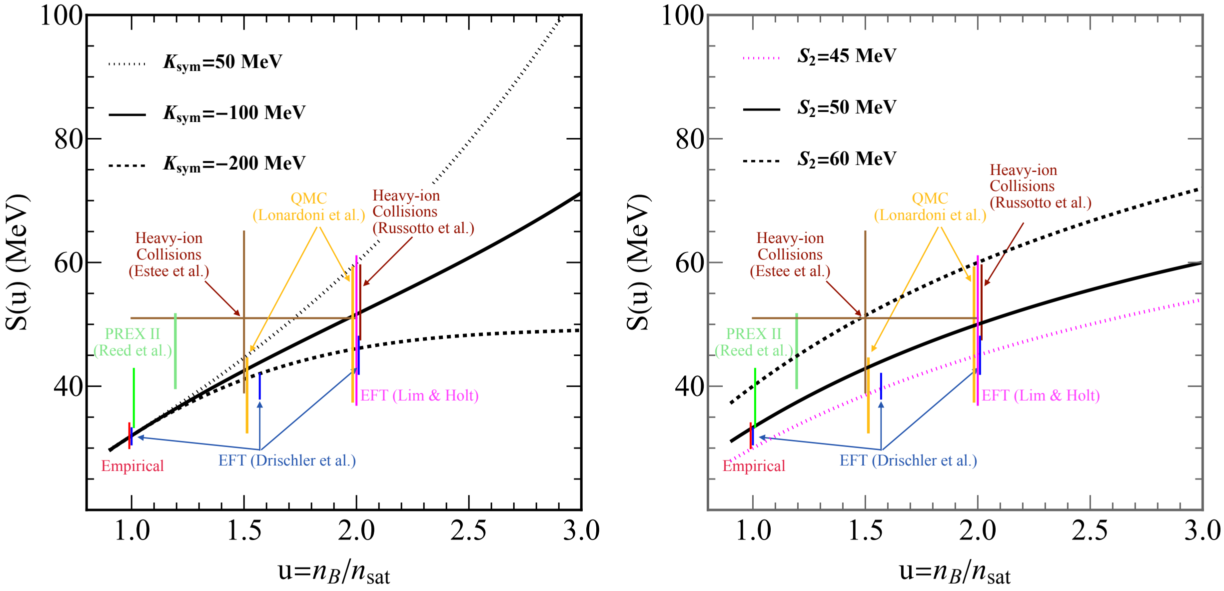

FIG. 32. Experimental and theoretical constraints on the density dependence of the nuclear symmetry energy. Predictions of the parametrization in Eq. 6.25 is shown in the left panel and the predictions of the parametrization in Eq. 6.26 is shown in the right panel .

The symmetry energy at higher density can be accessed in heavy-ion experiments, but is not presently well-determined [215]. At $n_B \simeq 1.5\ n_{\rm sat}$, a recent analysis by Estee et al. of charged pion yields from intermediate-energy heavy-ion collisions suggest that $S(n_B = 1.5 n_{\rm sat} \pm 0.5 n_{\rm sat}) = 52 \pm 13$ MeV [216]. Earlier studies by Russoto et al. of heavy-ion collisions at GSI indicate that $S(n_B \approx 2n_{\rm sat}) = 50 \pm 7$ MeV [217].

Theoretical calculations of the EOS using potentials derived from χEFT also provide useful constraints on the symmetry energy in the interval $1-2\ n_{\rm sat}$. Quantum Monte Carlo calculations by Lonardoni et al., using local χEFT potentials, predicts $S(1.5n_{\rm sat}) \approx 37 \pm 5$ MeV and $S(2n_{\rm sat}) \approx 46 \pm 11$ MeV [218]. In [219], Lim and Holt use MBPT to predict $S(2n_{\rm sat}) \approx 49 \pm 12$ MeV, and Drischler et al. combine MBPT and Bayesian estimates of the χEFT truncation errors (but neglect errors associated with low energy constants) to predict $S(2n_{\rm sat}) \approx 45 \pm 3$ MeV [212]. These constraints are shown in Fig. 32.

The density dependence of the symmetry energy is typically written as expansion about $n_B = n_{\rm sat}$:

$$S(u) = S_0 + L\left(\frac{u-1}{3}\right) + \frac{K_{\rm sym}}{2!}\left(\frac{u-1}{3}\right)^2 + \frac{Q_{\rm sym}}{3!}\left(\frac{u-1}{3}\right)^3 , \tag{6.25}$$

where $u = n_B/n_{\rm sat}$, and the parameters S_0, L, $K_{\rm sym}$, and $Q_{\rm sym}$ are chosen to ensure compatibility with experimental constraints. However, because the parameters $K_{\rm sym}$ and $Q_{\rm sym}$ are poorly constrained, the predictions of Eq. 6.25 at $n_B \gtrsim 2n_{\rm sat}$ vary over a wide range. This is illustrated in the left panel of Fig. 32, which shows a large variation at high density for $K_{\rm sym}$ in the range -200 MeV to 50 MeV. For this reason, Eq. 6.25 is not a useful expansion for $n_B \gtrsim 2n_{\rm sat}$.

In this study we instead adopt a simple ansatz for the symmetry energy, defined by the function

$$\tilde{S}(u) = \frac{2S_2 u}{2+u} , \tag{6.26}$$

which depends on a single parameter S_2 – the symmetry energy at $n_B = 2n_{\rm sat}$. This is a convenient choice because, as shown below, the symmetry energy at $n_B \simeq 2n_{\rm sat}$ plays a critical role in pion condensation. From the right panel of Fig. 32 it is clear that S_2 in the range $45 - 60$ MeV satisfies all existing constraints. The high value $S_2 = 60$ MeV is compatible with the large S_0 and L predicted by PREX and is implied by the heavy-ion data, the $S_2 \simeq 50$ MeV is compatible with the empirical range, and the low value $S_2 = 45$ MeV is in reasonable agreement with the χEFT predictions made in Ref. [212]. This variation, as we shall show below, is adequate to draw useful conclusions about pion condensation at $n_B \lesssim 3n_{\rm sat}$.

The calculation of the pion self-energy presented in the preceding section neglected short-distance interactions between nucleons and assumed that the energies of nucleons were unaltered by the medium. The energy difference between neutrons and protons can be quite large in dense matter, however. It is important to include this energy difference in calculating the pion self-energy because it alters energy denominators associated with diagrams that include an intermediate neutron-proton particle-hole state. A consistent approach to include this effect would be based on Chiral Effective Field Theory (χEFT)[34], as it systematically accounts for short-range interactions along with interactions mediated by pions. However, the predictive power χEFT for $n_B \gtrsim 2n_{\rm sat}$ is not well understood because truncation errors can grow rapidly at these densities (see Ref. [220] for a recent review). For this reason, we will defer to later work a study of pion condensation in which both pion-nucleon and nucleon-nucleon interactions are described systematically, and in what follows we describe a phenomenological model that will suffice to perform a parametric study.

The model we adopt is based on a mean field description of nuclear interactions. It is characterized by just two key parameters: the nuclear symmetry energy and the nucleon effective mass. In general, the strength of phenomenological, short-range interactions in mean field models are chosen to reproduce nuclear masses, and bulk properties of matter such its energy density, pressure, and susceptibilities. A common feature of mean field models is the modification of the single-particle nucleon energies due to their coupling to the mean field generated by other nucleons in the medium. In a large class of these models, the neutron and proton energies are given by

$$\begin{aligned} E_n(p) &= p^2/2\overline{M}_n + \Sigma_n \\ E_p(p) &= p^2/2\overline{M}_p + \Sigma_p \,, \end{aligned} \tag{6.27}$$

respectively. Here $\Sigma_{i=n,p}$ are the mean field energy shifts and $\overline{M}_{i=n,p}$ are nucleon effective masses of neutrons and protons in the medium. The mean field energy shift and the effective masses depend on the baryon density and the isospin asymmetry. Further, if for simplicity one neglects the difference between neutron and proton effective masses and assumes that $\overline{M}_n = \overline{M}_p = \overline{M}$, the difference between neutron and proton mean field energies can be directly related to nuclear symmetry energy. The beta equilibrium relation $\mu_n - \mu_p = \mu_e$, where μ_n and μ_p are the neutron and proton chemical potentials, allows us to write

$$\delta\Sigma = \Sigma_n - \Sigma_p = \mu_e - \left(\frac{k_{\mathrm{Fn}}^2 - k_{\mathrm{Fp}}^2}{2\overline{M}}\right) , \tag{6.28}$$

where $\mu_e = 4S(n_B)(1-2x)$, $k_{\mathrm{Fn}} = (3\pi^2 n_B(1-x))^{1/3}$ and $k_{\mathrm{Fp}} = (3\pi^2 n_B x)^{1/3}$ are the neutron and proton Fermi momenta, respectively.

Using nucleon propagators that include mean field energy shifts and a common nucleon effective mass $\overline{M}$, we have calculated the pion self-energy discussed in the previous section. We find that it only affects those diagrams that contain both neutron and proton intermediate states. In particular, the diagrams in Fig. 31 labelled (*ph*), (*pw*), and (*cd*) are the only ones changed, and the modification is to multiply the corresponding expressions (defined in Eqns. 6.15, 6.18, and 6.19) by the dimensionless factor

$$\xi(\omega_{\pi^-}) = \frac{\omega_{\pi^-}}{\omega_{\pi^-} - \delta\Sigma} , \tag{6.29}$$

and to make the substitution $M \to \overline{M}$. The factor $\xi(\omega_{\pi^-})$ can resonantly enhance the contribution from these diagrams when $\omega_{\pi^-} \simeq \delta\Sigma$. At the condensation threshold when $\omega_{\pi^-} = \mu_e$, the multiplicative factor

$$\xi(\mu_e) = \frac{\mu_e}{\mu_e - \delta\Sigma} = \frac{2\overline{M}\mu_e}{k_{\mathrm{Fn}}^2 - k_{\mathrm{Fp}}^2} , \tag{6.30}$$

depends on the nuclear symmetry energy and nucleon effective mass.

Small energy denominators modify power counting: the diagram labelled (*ph*), which originally contributed at $\mathcal{O}(k_{\mathrm{F}}^5\mu_e)$ now contributes at at $\mathcal{O}(k_{\mathrm{F}}^3\mu_e^2)$; the diagram labelled (*pw*), which originally contributed at $\mathcal{O}(k_{\mathrm{F}}^6\mu_e)$ now contributes at $\mathcal{O}(k_{\mathrm{F}}^4\mu_e^2)$; and the diagram labelled (*cd*), which originally contributed at $\mathcal{O}(k_{\mathrm{F}}^8\mu_e)$ now contributes at at $\mathcal{O}(k_{\mathrm{F}}^6\mu_e^2)$. Crucially, in neutron-rich matter, these enhanced diagrams are attractive.

The contributions from the individual diagrams to the pion self-energy is shown in Fig. 33. We plot the normalized self-energy, defined by $\delta\omega = \Pi(\mu_e)/2m_\pi$, as it provides a rough

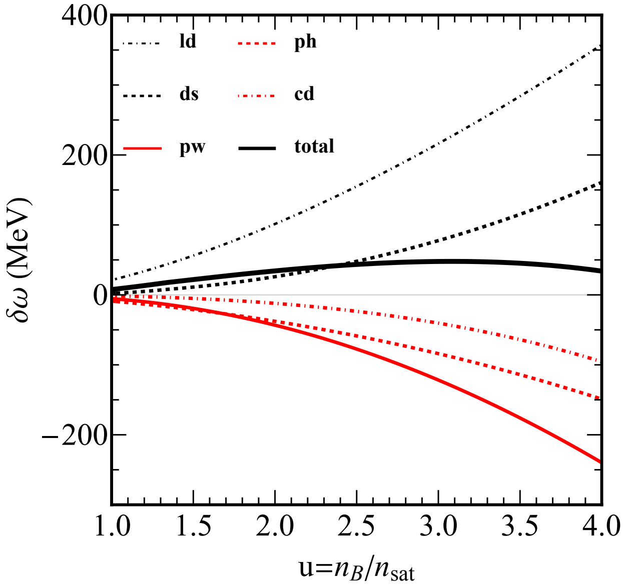

FIG. 33. Contributions to $\delta\omega = \Pi(\mu_e)/2m_\pi$ due to the individual diagrams. Here we have chosen $\tilde{\sigma} = 60$ MeV, $S_2 = 50$ MeV, and $\alpha = 7\%$.

estimate of the energy shift of pions due to interactions. The symmetry energy defined in Eq. 6.26 is used with $S_2 = 50$ MeV. In our parametric study, the density dependence of the nucleon effective mass is given by

$$\overline{M} = M\left(1 - \alpha\frac{n_B}{n_{\rm sat}}\right) , \tag{6.31}$$

and we vary the parameter α in the range $0 - 0.1$ to explore the range predicted by microscopic calculations [221, 222]. In Fig. 33 we have used $\alpha = 0.07$.

The large cancellation between repulsive and attractive contributions over a wide range of baryon density in Fig. 33 is one of our main findings. Previous studies, especially those that focused on p-wave pion condensation, concluded that s-wave pion condensation was unlikely because only repulsive contributions were considered. These contributions, due to the diagrams labelled ld and ds, scale approximately as $k_{\rm Fn}^3\mu_e$ and $k_{\rm Fn}^4\mu_e^2$, respectively. Alternatively, the attractive contributions, from diagrams labelled ph and pw, scale as $k_{\rm Fn}^3\mu_e^2$ and $k_{\rm Fn}^4\mu_e^2$, respectively. Although a comparison between the terms of different order in the figure suggests that χPT remains useful for $n_B \lesssim 3n_{\rm sat}$, due to large cancellations, higher-order terms can play an important role. For example, at $n_B = 3n_{\rm sat}$ the cd diagram, which contributes at order $k_{\rm Fn}^6\mu_e^2$, makes a contribution that is about a factor of 5 smaller than the

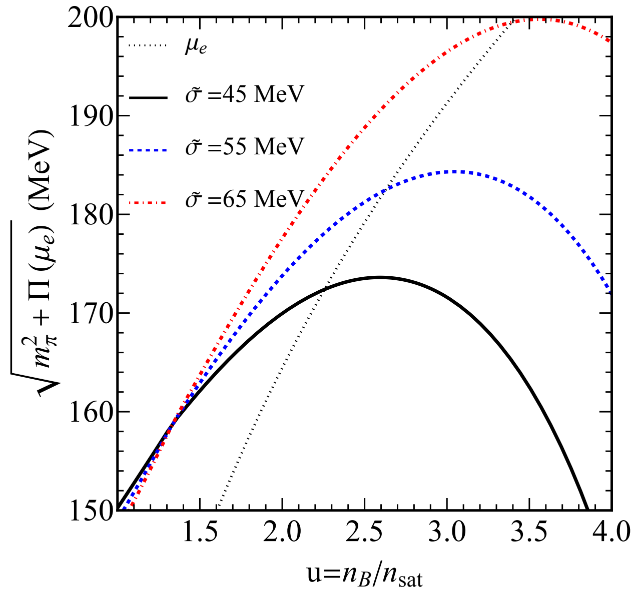

FIG. 34. Energy of a pion at rest in neutron star matter. Here we take $\tilde{\sigma} = 45, 55, 65$ MeV, $S_2 = 50$ MeV, and $\alpha = 7\%$. The electron chemical potential is also shown as the dotted line. The critical density for condensation occurs when $\mu_e(n_B) = \sqrt{m_\pi^2 + \Pi_{\rm tot}(\mu_e(n_B))}$ and corresponds to the point at which the curves intersect.

leading-order contribution for $c_D = 1$, but its magnitude is nonetheless comparable to $\Pi_{\rm tot}$.

In Fig. 34 we plot $m_\pi^* = \sqrt{m_\pi^2 + \Pi_{\rm tot}(\mu_e)}$ as a function of n_B for $\tilde{\sigma} = 45$ MeV, 55 MeV, and 65 MeV, using fiducial values $S_2 = 50$ MeV and $\alpha = 0.07$. The electron chemical potential μ_e is also shown (dotted curve), and the condensation condition Eq. 6.21 is fulfilled when the curves intersect. Notice that the critical density increases rapidly from 2.2 $n_{\rm sat}$ to 3.4 $n_{\rm sat}$ when $\tilde{\sigma}$ is changed from 45 MeV to 65 MeV. In general, we find that the quantity

$$\delta^2 = \mu_e^2 - m_\pi^{*2}\,, \tag{6.32}$$

which is a measure of the proximity to condensation, is small compared with μ_e^2 over a wide density interval: $n_B = 2n_{\rm sat} - 4n_{\rm sat}$. This implies that even small variations in the model parameters and higher-order diagrams can have a large impact on the critical density, especially when $\tilde{\sigma} > 60$ MeV.

This sensitivity to small changes in the model parameters is quantified in Fig. 35. Contours of constant critical density $n_c = 2n_{\rm sat}$ and $n_c = 3n_{\rm sat}$ in the $\tilde{\sigma} - S_2$ plane are shown in the left panel. The critical density as a function of $\tilde{\sigma}$ for various values of c_D and the symmetry energy parameter $S_2 = 50$ MeV are shown in the middle panel, and for $S_2 = 60$

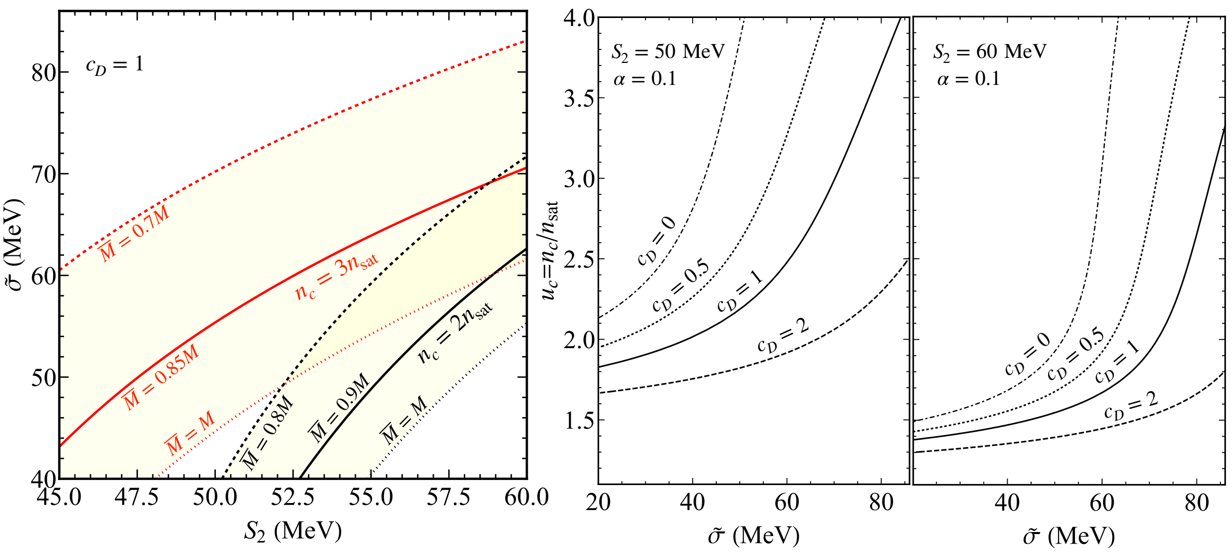

FIG. 35. Contours of constant critical density in the $S_2 - \tilde{\sigma}$ plane for $\alpha = 0, 0.05, 0.1$, and $c_D = 1$ (left panel). In the middle and right panels, we show the critical density as a function of $\tilde{\sigma}$ for various values of c_D and the symmetry energy parameter $S_2 = 50$ MeV (middle panel) and $S_2 = 60$ MeV (right panel).

MeV are shown in the right panel. The results in Fig. 35 can be summarized as follows:

- For large symmetry energy, i.e., $S_2 \gtrsim 55$ MeV, the critical density for condensation $n_c \lesssim 3n_{\rm sat}$. At these lower densities, we expect our χPT -based calculation to be reliable, and condensation is robust with respect to small changes to other parameters.

- When the energy dependence of the isospin scattering amplitude is weak, i.e., $\tilde{\sigma} \lesssim 50$ MeV, $n_c \lesssim 3n_{\rm sat}$ and condensation is robust with respect to small changes to other parameters.

- A modest reduction in the nucleon effective mass with increasing density and positive values for the coupling c_D favor condensation and lower the critical density.

- Condensation at $n_B \lesssim 3n_{\rm sat}$ is unlikely if the symmetry energy is small, i.e., $S_2 < 45$ MeV, and $\tilde{\sigma} > 60$ MeV.

6.3. Implications for Neutron Stars

Properties of the pion-condensed state have been discussed in earlier work [40, 192, 195], here we highlight unique properties of the s-wave pion-condensed ground state that have been previously overlooked. The discussion in the preceding section suggests that s-wave pion condensation is likely in the density interval $2n_{\rm sat} - 3n_{\rm sat}$ if the symmetry energy $S(n_B) \gtrsim 55$ MeV at these densities. The sensitive cancellation between large repulsive and attractive contributions also implies that the energy shift of pions is small and positive, and is typically in the range $10 - 50$ MeV for $\tilde{\sigma} \simeq 45 - 60$ MeV. As we show below, this small, positive shift implies the number density of pions in the condensed state will be small, as it will be regulated by both repulsive self-interactions and interactions with nucleons.

6.3.1. EOS and Neutron Star Structure

To construct a model for the equation of state of neutron star matter with a pion condensate, we write the free energy density including nuclear interactions as

$$\Omega(\mu_B, \hat{\mu}; n_B, x, \theta) = \Omega_B + \Omega_{\pi\pi} + \Omega_{B\pi} + \Omega_e + \Omega_\mu \,, \tag{6.33}$$

where

$$\Omega_B = \epsilon_B(n_B, x) - \mu_B n_n - (\mu_B - \hat{\mu}) n_p \,, \tag{6.34}$$

is the free energy density of the baryons, and

$$\epsilon_B(n_B, x) = \frac{3}{5}\frac{k_{\rm F}^2}{2m} n_B + V(n_B) + n_B(1-2x)^2 S(n_B)$$

is the energy density of asymmetric nuclear matter with baryon density n_B and proton fraction x. Here $k_{\rm F} = (3\pi^2 n_B/2)^{1/3}$, $V(n_B)$ is the potential energy of symmetric nuclear matter, and $S(n_B)$ is the symmetry energy defined earlier.

Ω_π is the free energy of the pion condensate, which includes interactions between pions described by the Lagrangian in Eq. 6.3. It can be calculated in the mean field approximation

[42, 46] by assuming that the charged pion condensate is a spatially uniform classical field

$$\langle \pi^- \rangle = \frac{f_\pi}{\sqrt{2}} \theta e^{-i\hat{\mu}t}, \tag{6.35}$$

where θ is real and characterizes the amplitude, and the time-dependence in equilibrium is determined by the charge chemical potential [193]. Using Eq. 6.3 we obtain the free energy of this classical field

$$\Omega_{\pi\pi} = -f_\pi^2 \frac{\hat{\mu}^2}{2} \sin^2 \theta + 2m_\pi^2 f_\pi^2 \sin^2 \frac{\theta}{2} \,. \tag{6.36}$$

The contribution to the free energy due to the interactions between nucleons and the pion field, can be calculated straightforwardly when the condensate amplitude is small. We find that it is given by

$$\Omega_{B\pi} = \mathrm{Re}\Pi_{\mathrm{tot}}(\hat{\mu}, k_{\mathrm{Fn}}, k_{\mathrm{Fp}}) \frac{f_\pi^2 \theta^2}{2} \,, \tag{6.37}$$

where $\Pi_{\mathrm{tot}}(\hat{\mu}, k_{\mathrm{Fn}}, k_{\mathrm{Fp}})$ is the pion self-energy defined in Eq. 6.20, and $k_{\mathrm{Fn}} = (3\pi^2 n_B(1-x))^{1/3}$ and $k_{\mathrm{Fp}} = (3\pi^2 n_B x)^{1/3}$ are the neutron and proton Fermi momenta. Note that Eq. 6.37 includes quantum fluctuations as the self-energy contains important 2-loop contributions. A calculation that would incorporate higher-order $\theta-$terms into $\Omega_{B\pi}$ requires a proper treatment of the mixing between neutron and proton states induced by the axial current interactions. This is tedious and we defer its calculation to future work. Fortunately, the result in Eq. 6.37 will suffice because we shall find θ to be small.

Electrons and muons are treated as non-interacting Fermi gases and their free energies are given by

$$\Omega_e = \frac{1}{\pi^2} \int_0^{k_{\mathrm{Fe}}} dk k^2 \left(\sqrt{k^2 + m_e^2} - \hat{\mu} \right) \,, \quad \Omega_\mu = \frac{1}{\pi^2} \int_0^{k_{\mathrm{F}\mu}} dk k^2 \left(\sqrt{k^2 + m_\mu^2} - \hat{\mu} \right) \,, \tag{6.38}$$

where $k_{\mathrm{Fe}} = \sqrt{\hat{\mu}^2 - m_e^2}$ and $k_{\mathrm{F}\mu} = \sqrt{\hat{\mu}^2 - m_\mu^2}$ for $\hat{\mu} > m_\mu$, and $k_{\mathrm{F}\mu} = 0$ for $\hat{\mu} \leq m_\mu$. The ground state is obtained by minimizing the free energy with respect to n_B, x and θ, and by enforcing electric charge neutrality. This requires that $\partial\Omega/\partial n_B = 0$, $\partial\Omega/\partial x = 0$, $\partial\Omega/\partial\theta = 0$, and $\partial\Omega/\partial\hat{\mu} = 0$. At given μ_B, the state variables n_B, x, θ, and $\hat{\mu}$ are obtained by solving

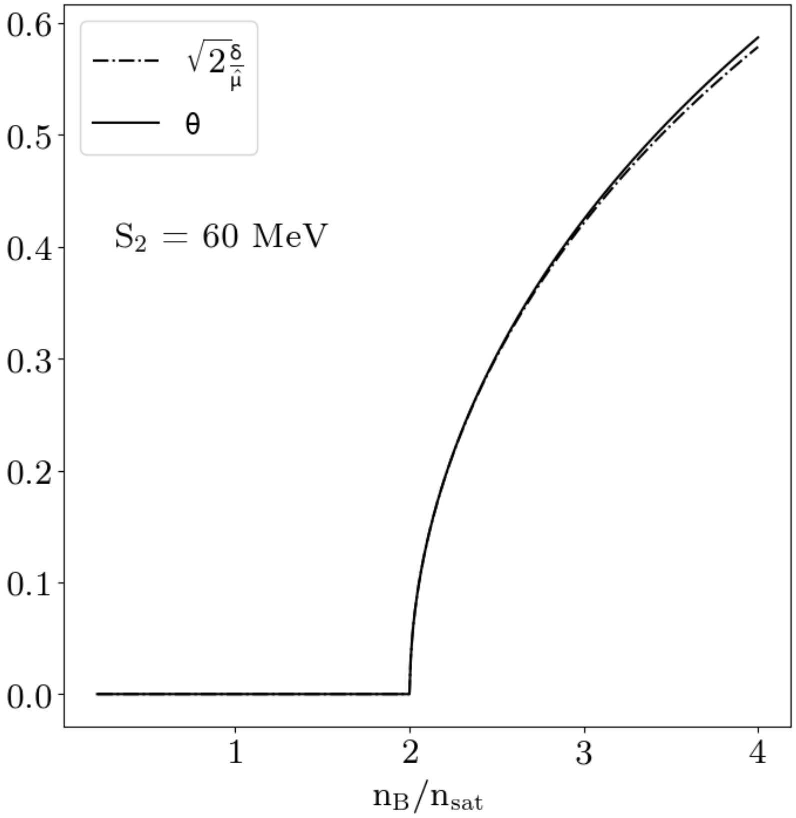

FIG. 36. Resulting value of the θ parameter within a model with constant effective pion mass which is set such that condensation occurs at twice nuclear density. An approximation to the value of θ is shown by the dash-dotted line.

these four equations simultaneously. We find that

$$\theta \approx \frac{\sqrt{2}\delta}{\hat{\mu}}\,, \tag{6.39}$$

where $\delta = \sqrt{\hat{\mu}^2 - m_\pi^{*2}}$, and $m_\pi^{*2} = m_\pi^2 + \Pi_{\rm tot}(\hat{\mu}, k_{\rm Fn}, k_{\rm Fp})$ as defined earlier in section 6.2. For the range of parameters considered in this study we find that $\theta \lesssim 1$ in the pion-condensed phase and this approximate formula is adequate to describe the evolution of the condensate amplitude. The evolution of the value of theta along with the approximation given in Eq. 6.39 is shown in Fig. 36 for comparison.

As an approximation to the full pion energy, we use a model with a constant effective pion mass. This model does not take into account the complex dependencies of the self-energy on u, x, and $\hat{\mu}$, but, given the relatively small changes to the pion energy over a large range of densities, seen in Fig. 34, it gives us a sufficiently accurate model of a second-

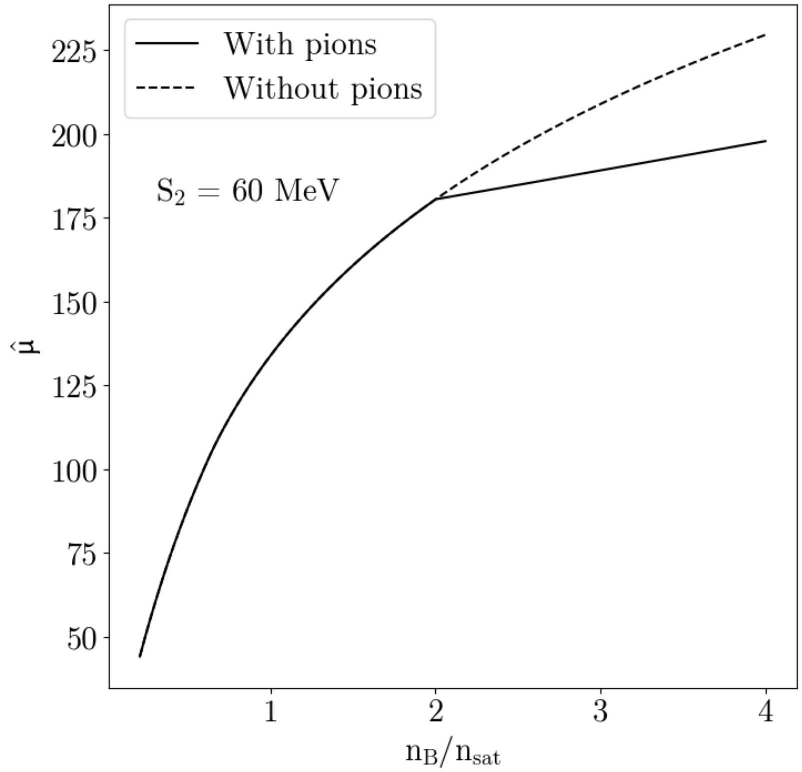

FIG. 37. Evolution of the charge chemical potential, $\hat{\mu}$, parameter as a function of density. The onset of pion condensate abruptly slows $\hat{\mu}$'s increase with density, subsequently limiting the total number of pions that can appear.

order phase transition to the condensate phase. This model allows us to analyze the effect of the pion condensate on the equation of state without needing to take into account the full complexities of the self-energy. We fix the constant effective pion mass such that pion condensation occurs at $n_B = 2n_{\rm sat}$. This is the model used to create Fig. 36, 37, and 38.

The pressure associated with pions, including their interactions with nucleons, given by

$$P_\pi = -(\Omega_{\pi\pi} + \Omega_{B\pi}) \approx \frac{f_\pi^2 \delta^4}{2\hat{\mu}^2}\,, \tag{6.40}$$

is negligibly small compared with the pressure due to baryons because $\delta^2 \ll \hat{\mu}^2$. In the left plot of Fig. 38 we show the charged particle fractions in dense matter calculated for the scenario in which the symmetry energy parameter $S_2 = 60$ MeV. The results in Fig. 38 are for the scenario in which pion condensation occurs at $n_B = 2n_{\rm sat}$. As expected, since the pion condensate furnishes negative charge, the proton fraction in the electrically neutral ground state increases with the amplitude of the pion condensate. The addition of the pions as a source of negative charge means the necessary electron fraction to maintain a neutral state is lower. Figure 37 shows how the charge chemical potentials' increase is abruptly slowed by the onset of condensation. This subsequently ensures that the charge chemical potential is never much greater than the effective pions mass, limiting the number of pions.

The resulting equation of state in the condensed phase is shown in the right plot of Fig 38. However, the change to the baryonic EOS is minimal due to the limited number of pions which appear, with the most significant change in EOS coming from the change of the proton fraction. Eq. 6.41 gives the change of the nucleon pressure given a change in the proton fraction. The overall change to the EOS has only a very small effect on the mass-radius curve.

$$\Delta P_N = P_N(x+\delta x) - P_N(x) = -4\delta x(1-2x-\delta x)u^2 n_0 \frac{\partial S(u)}{\partial u} \tag{6.41}$$

It is reasonable to consider if the onset of pion condensation could create a region of density where the direct Urca process is allowed, potentially leading to faster neutron star cooling. While the increase in the proton fraction and subsequent decrease of the neutron fraction do bring the system closer to the direct Urca threshold, the decrease of the electron fraction, and subsequently its Fermi momentum, undoes much of this. The over all effect of the pion condensate is to bring the system closer to the Urca threshold but the effect is not significant enough to push many systems over it.

6.3.2. High-T_c Superconductivity

The ground state with a charged pion condensate is a superconductor and spontaneously breaks the $U(1)$ electromagnetic gauge symmetry, it also breaks isospin symmetry and parity. Since superconductivity alters the electromagnetic properties it has important implications for magnetic fields and their evolution in neutron stars. In early work, Harrington and Shepard showed that an s-wave charged pion condensate would be a Type II superconductor when its interactions with nucleons was neglected [223]. In this case, when the magnetic field exceeds a critical value, it would penetrate the condensate in the form of flux tubes.

We note that in neutron star matter without pion condensation, Cooper pairing between protons also leads to superconductivity [224]. Its implications for magnetic field structure and evolution are qualitatively similar, but there is one key difference. The critical tem-

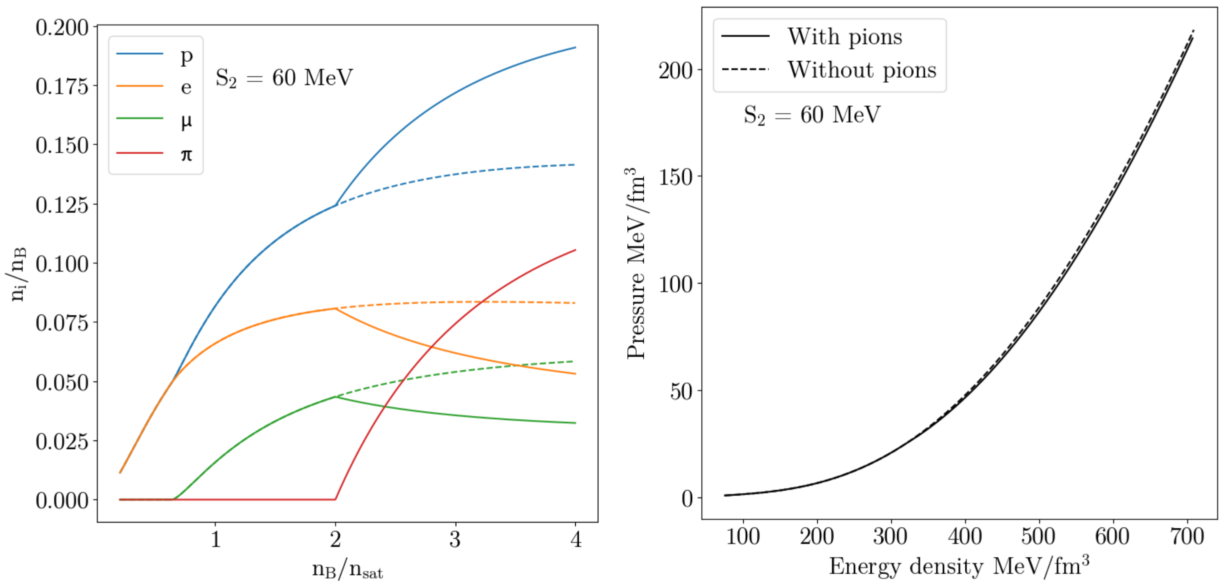

FIG. 38. *Left*: Effect of the pion condensate on particle fractions. The dashed lines show particle fractions of protons, electrons, and muons without any pions while the solid lines show these particle fractions in addition to the pion's when a pion condensate is allowed to form. The pions serve as another source of negative charge, but in doing so decrease the negative charge chemical potential, $\hat{\mu}$. So while the total number of negatively charged particles has increased, the number of electrons and muons decreases. The lower-than-expected $\hat{\mu}$ also limits the pion number fraction. While the proton fraction increases the change is not significant enough to have relevant effects on the EOS. *Right*: Equation of state of the model with and without pions given the symmetry energy parameter, S_2, is equal to 60 MeV. The creation of the pion condensate is unable to dramatically alter the EOS due to the rather small change to the proton fraction. Because the negative charge chemical potential doesn't exceed the pion energy by much, the pion density is limited.

perature for proton superconductivity $T_c^{\mathrm{p}} \lesssim 1$ MeV is significantly smaller than the critical temperature for the pion condensate which we estimate to be

$$T_C^\pi \approx \frac{2\pi}{m_\pi^*}\left(\frac{n_\pi}{\zeta(3)}\right)^{2/3} \simeq 60\left(\frac{m_\pi}{m_\pi^*}\right)\left(\frac{n_\pi}{0.025\ \mathrm{fm}^{-3}}\right)^{2/3} \mathrm{MeV}\,, \tag{6.42}$$

where n_π is the pion density. Eq. 6.42, which assumes that the pion condensate can be approximated as non-interacting Bose-Einstein condensate, should be viewed as crude estimate and warrants further work. Nonetheless, it implies that neutron stars with pion condensates will likely remain in the superconducting state during their birth in core-collapse supernovae and during neutron star mergers when the temperature $T \simeq 30 - 50$ MeV. This is significant because superconductivity due to pion condensation can impact magnetic field evolution during neutron star mergers and core-collapse supernovae and their associated multi-messenger signatures.

6.4. Conclusions on s-wave pion condensation in neutron stars

In this section we have constructed a model for the self-energy of a pion at rest in a dense nuclear medium. This model consists of a two-loop calculation of the pion self-energy within heavy-baryon chiral perturbation theory, which is augmented by in-medium modifications to the nucleon propagators. These modifications include energy shifts and effective masses of the nucleons due to interactions with the nuclear medium.

Qualitative changes arise from these slight modifications. In particular, small energy denominators are produced which modify the power counting of Feynman diagrams. Certain attractive diagrams (in this section denoted Π_{ph}, Π_{pw}, Π_{cd}) are promoted and drive down the pion self-energy. While the model dependence of our study precludes a firm conclusion regarding the existence of s-wave pion condensation in dense, neutron-rich matter, we believe our results show that condensation is not robustly excluded. This is in contrast to the historical position, which posits that the repulsion due to the Weinberg-Tomozawa interaction is sufficient to robustly prevent pion condensation.

We performed a parametric study of our self-energy which revealed several general trends. First, high symmetry energies, small "sigma terms", and small nucleon effective-masses favor condensation. However, the uncertainty of the nuclear symmetry energy at high density and the poor convergence of the T^+ scattering amplitude in chiral perturbation theory prevent firm conclusions.

We explored the implications of this pion self-energy on the properties of neutron stars. While a non-trivial density of pions condense, the equation of state of nuclear matter is changed little by pion condensation. This can be viewed as an example of the "masquerade problem" [225]: though little changes in the mass-radius curve, the contents of a neutron star have changed.

Though the equation of state is only slightly changed by the presence of pions, we speculate that the transport properties of neutron stars are changed by the presence of an s-wave pion condensate. This charged condensate forms a superconductor exhibiting the Meissner effect, thereby altering the propagation of electromagnetic fields. Furthermore, in the condensed state, protons and neutrons form quasiparticles with a mixing angle proportional to the condensate magnitude θ. This mixing will impact direct Urca reactions. Rather than two distant Fermi surfaces between protons and nucleons, the quasiparticles will have Fermi surfaces of lying closer together, which may increase the rate of Urca reactions. We leave for future work exploration of the modifications to transport outlined above.

7. CONCLUSION

Supernovae and neutron stars are complex systems which are still under intense study. Great advancements have been made in the understanding of each but many fundamental questions remain unanswered such as particular details on the supernova explosion mechanism and the matter content in the core of neutron stars. The results presented here establish the need to include pions as explicit degrees of freedom in calculations involving dense, asymmetric nuclear matter.

Within this thesis we have investigated the part pions play in the remaining questions relating to supernovae and neutron stars. In section 3.2, we have shown that that negatively charged pions are an important degree of freedom in hot dense matter encountered in astrophysics. The virial expansion provides a model-independent approach to include pion-nucleon interactions when the fugacities are small and provides strong evidence for the enhancement of the pion number density due to pion-nucleon interactions. In section 4.2, using the pseudo-potential model, we calculate the effect of new pion interactions on the neutrino mean free path, finding that the presence of pions and muons allows for additional charged-current reactions, $\nu_\mu + \pi^- \to \mu^-$ and $\bar{\nu}_\mu + \mu^- \to \pi^-$, which dominate the neutrino mean free path at low energy. These charged-current reactions have the potential to impact on energy transport in protoneutron stars and neutron star mergers.

We also apply the pseudo-potential model to calculations of axion emissivity from pions in section 5 and 5.3.6. The results of the supernova simulation show the pion channel has a significant effect on axion cooling, where previously this channel was thought to be negligible due to the assumed small numbers of pions. As a consequence, the inclusion of axion cooling from this channel significantly shortens the timescale of neutrino emission, in comparison to the case when only bremsstrahlung processes are considered.

Preliminary results for pion effects on the neutron star bulk viscosity and for our detailed reevaluation of s-wave pion condensation are given in sections 4.4 and 6, respectively. In our reevaluation of s-wave pion condensation, we find that the presence of pions does not appreciably alter the equation of state even though the composition changes greatly. This means that while the mass-radius relationship for neutron stars is not affected much by the presence of pions, other observable effects can exist such as the presence of a high critical temperature superconducting phase.

Appendix A: EOS with pions using the virial approximation

In this section I will describe the code which solves for the properties of the equation of state described in section 3.2 in a way which is independent of the nuclear equation of state on which it is based. Within the virial expansion the nucleons of course have a large effect on the pions, which is taken into account by the interaction number density

$$n_{\pi^-}^{\text{int}} = \sum_{N=n,p} z_N z_{\pi^-} b_2^{N\pi^-} \ , \tag{A.1}$$

The pions have a similar, direct effect on the number density of nucleons given by

$$n_N^{\text{int}} = z_N z_{\pi^-} b_2^{N\pi^-} \ , \tag{A.2}$$

However, within the conditions where the virial approximation holds, I have found the pions direct effects on the nucleons to be negligible. Given this, I will first describe the simpler version of the equation of state in which these direct effects on the nucleons from pions are ignored, and at the end of this section describe how I modify this prescription to evaluate the fully consistent equation of state which includes Eq. A.2.

In the simplified method, all we need from the nuclear EOS to which pions are being added is a method for finding the neutron and proton chemical potentials given the baryon density, temperature, and proton fraction. For the detailed example I will assume we are interested in $npe\pi^-$ matter where neutrinos are not trapped and which is in beta equilibrium. In order to solve for the particle fractions within this augmented equation of state, we must be given the ambient conditions. From this we apply restrictions which apply to the matter of interest. The restrictions which apply to this matter are given by

$$\begin{aligned} Y_p &= Y_e + Y_{\pi^-} \\ \mu_n - \mu_p &= \mu_e \end{aligned} \tag{A.3}$$

which are charge neutrality and beta equilibrium respectively. The Y_i are the particle fractions relative to the baryon density. The condition on the pion chemical potential

$$\mu_n - \mu_p = \mu_{\pi^-} \tag{A.4}$$

Should be equilibrated on timescales corresponding to the strong interaction and so will be assumed to always hold for the purpose of this work. In this type of matter, we require the baryon density and temperature to be specified which we consider to be the ambient conditions.

I will call the function which does the bulk of the work in this code: `defining_equations`. It takes in the baryon density, temperature, and the proton fraction and returns a single number which is zero when charge neutrality and beta equilibrium are satisfied. This function is called many times with various proton fractions using Newtons method, binary search, or any more sophisticated method to find this zero point and thus, the correct value of the proton fraction.

When the `defining_equations` function is called, it immediately finds the neutron and proton chemical potentials from the nuclear equation of state which also has baryon density, temperature, and the proton fraction as input parameters. These in turn give the electron and pion chemical potentials from the respective restrictions given above. It is then straight-forward to use the Fermi-Dirac distribution and Bose-Einstein distribution to find the number density of electrons and the number density of free pions. To find the number density of pions with interactions in this approximation, all that is required is to add the contribution from Eq. A.1. Finally, the function returns the difference between the left- and right-hand sides of the charge neutrality condition.

The `defining_equations` function forms the bulk of the physics calculations (outside of the nuclear EOS implementation) as once the zero of `defining_equations` is found, one can repeat the steps that occur in the function to find the correct values for particle number densities and chemical potentials. These can be used to obtain any of the other properties of interest like the energy and pressure.

In order to modify this method to consistently account for the direct effects of pions on the nucleons, only a few changes need to be made. We will again assume $npe\pi^-$ matter where neutrinos are not trapped and which is in beta equilibrium (generalizations to other types of matter will follow later in this section). The addition of the terms in Eq. A.2 to the neutron and proton densities can be taken into account by including two additional input parameters as well as two additional constraints. In addition to the proton fraction, we also include the neutron and proton chemical potentials, for which the appropriate values will be found via Newton's method. So, in the consistent case, the input to the `defining_equations` function is the baryon density, temperature, proton fraction, neutron chemical potential, and proton chemical potential. Subsequently, we can skip the step of calculating the nucleon chemical potentials from the nuclear EOS and instead calculate the proton and neutron densities from their chemical potentials using the nuclear EOS. Add to these the respective values from Eq. A.2 and these values can be compared to the neutron and proton densities obtained from the baryon density and proton fraction. Finally, to complete the `defining_equations` function it must again return the discrepancy from neutral matter but is also required to return the difference between the two values of neutron density and the difference between the two values of the proton density. Then, as before, this function can be called via a Newton-like solver for the point where all return values are zero, indicating that the correct values of proton fraction and nucleon chemical potentials have been found.

The calculation of two number densities for both neutrons and protons may seem redundant, but these added conditions do effectively constrain the extra inputs of the chemical potentials as well as ensure the nucleon number densities satisfy the correct values to consistently account for the pions effects through the virial expansion. This can be seen by the fact that one pair of densities is dependent only on the baryon density and proton fraction, independent of chemical potentials, while the other set (which includes the contribution from Eq. A.2) is dependent on the chemical potentials.

Some of the interesting modifications are including muons, neutrino-trapped matter, and matter out of beta equilibrium. I will briefly describe modifications to the `defining_equations` function which can account for each of these in any combination.

Including muons: Similarly to electrons, muons can be approximated as non-interacting and even have equal chemical potential while in beta equilibrium without trapped neutrinos. They can be included in the code in an identical manner, being sure to include them in the calculation of the charge neutrality discrepancy.

Neutrino-trapped matter: When neutrinos are trapped their chemical potential is no longer zero. These will be included as additional parameters to the function, similar to the baryon density and temperature as they are conditions the matter satisfies as opposed to values to be found by the code. Other values could be used for this purpose, such as the total lepton fractions. No extra constraints are returned by the code compared to matter which is identical but doesn't trap neutrinos and the only changes needed are to correctly account for beta equilibrium including the neutrino chemical potential. For the electron this is given by

$$\mu_n - \mu_p = \mu_e - \mu_{\nu_e} \tag{A.5}$$

where μ_{ν_e} is the chemical potential of electron neutrinos which is the negative of the electron anti-neutrinos' chemical potential. A similar equation holds for muons. In the `defining_equations` function, once the nucleon chemical potentials are found their difference along with the neutrino chemical potential, gives the charge lepton chemical potential, and the code can continue as before.

Matter out of beta equilibrium: Matter out of beta equilibrium requires a substantially different function to evaluate. This is mostly due to the fact that without the beta equilibrium condition, some of that values we previously solved for must instead be given as conditions for the matter. I have used this code in calculations of bulk viscosity as in the calculations within section 4.4. In this case, the extra specified conditions I have used are the particle fractions of all but one charged particle: the electron. Since charge neutrality is still assumed, the value of the electron fraction can be found directly from the given values. Given the particle fractions as well as the baryon density and temperature, one can find the nucleon densities, and from them, the nucleon chemical potentials using the nuclear EOS. Since the leptons are assumed to be free particles, their chemical potentials can be found by numerically inverting the equation for their number densities. The only remaining quantity to fully specify the EOS is the pion chemical potential. In general, Eq. A.4 would be used to determine the pion chemical potential, but it is necessary to relax this condition in the calculation of susceptibilities for bulk viscosity calculations. In this case one can use a similar method that was used in the `defining_equations` function to determine the proton fraction but instead for the pion chemical potential, where the two numbers to be compared are the pion fraction given as input and the pion fraction calculated using the virial expansion using a variable chemical potential. As before the zero of this function is found using Newtons method or similar algorithm.

Appendix B: Pseudo-potential pion self-energy calculation

The pseudo-potential ansatz for the pion self-energy from [26] is discussed in 3.3 and is given by

$$\Sigma_{\pi^-}(p) = \int \frac{d^3k}{(2\pi)^3} \sum_{N=n,p} f_N(E_N(k))\ V^{ps}_{N\pi^-}(p_{cm})\,, \tag{B.1}$$

This is just an integral over the distribution of nucleons, f_N, multiplied by a pseudo-potential, V^{ps}. The pion-nucleon pseudo-potential is directly proportional to the phase shifts, δ, and is given by

$$V^{(ps)}_{N\pi^-}(p_{\rm cm}) = -\sum_{I,l,\nu} \alpha_l (2l+1) \frac{2\pi\delta^I_{l,\nu}}{\bar{m}\ p_{\rm cm}}\,. \tag{B.2}$$

Here, $p_{\rm cm} = \bar{m}\sqrt{\frac{p^2}{m_\pi^2} + \frac{k^2}{m_N^2} - \frac{2pk}{m_\pi m_N}\cos\theta}$ is the center of mass momentum, and $\bar{m} = m_\pi m_N/(m_N + m_\pi)$ is the reduced mass. The sum is over allowed values of the isospin (I), angular momentum values (l), and nucleon spin-projections ($\nu = +, -$).

The values of the α_l are determined by evaluating the pion number density using a Bose-Einstein distribution and Eq. B.1 and fitting to values of the pion number density obtained using the virial expansion method described in section A. The fitting requires choosing points in baryon density and temperature space, one for each of the α_l. Since the values of α_l control the strength of the s-wave and p-wave phase shifts, it makes sense to choose one point to be at low temperature and the other to be at some higher temperature, as low temperatures should be more strongly influenced by the s-wave relative to high temperatures. The original pseudo-potential ansatz used equal values for the s-wave and p-wave fitting factors, α. Due to the strong p-wave attraction the value of the fitting factor was highly suppressed, causing the s-wave phase shift contribution to be unnaturally small. By having separate fitting factors for the s-wave and p-wave phase shifts this issue is mitigated.

In EOS calculations, this self-energy ansatz can be used to calculate the pion distribution function. This means an EOS similar to the one described in Appendix A can be constructed. The construction is very similar, but instead of including pion-nucleon interactions through the additive virial correction in Eq. A.1, they are instead accounted for directly in the integral over the pion distribution function. The main difference that occurs is that it is now necessary to account for the distribution of nucleons. This means for any given conditions it will be necessary to pass the distribution functions of nucleons (or parameters that can be used to recreate them) to the pion density calculation. In my version of this code, the distribution of nucleons is reproduced using the effective masses and chemical potentials of the nucleons within the Fermi-Dirac distribution. The self-consistent version of this calculation, where nucleons are directly affected by the pseudo-potential, has not been implemented. These effects should not be large as noted in Appendix A.

Appendix C: Maxwell Relations

The first law of thermodynamics in $npe^-\mu^-\nu_e\nu_\mu\pi^-$ matter can be written

$$\begin{aligned} dE = -P\,dV + T\,dS + \mu_n\,dN_n + \mu_p\,dN_p + \mu_e\,dN_e \\ + \mu_\mu\,dN_\mu + \mu_{\nu_e}\,dN_{\nu_e} + \mu_{\nu_\mu}\,dN_{\nu_\mu} + \mu_\pi\,dN_\pi\,. \end{aligned} \tag{C.1}$$

We normalize all quantities by baryon number N_B

$$\begin{aligned} d\left(\frac{\varepsilon}{n_B}\right) = \frac{P}{n_B^2}\,dn_B + T\,d\left(\frac{s}{n_B}\right) + \mu_n\,dx_n + \mu_p\,dx_p \\ + \mu_e\,dx_e + \mu_\mu\,dx_\mu + \mu_{\nu_e}\,dx_{\nu_e} + \mu_{\nu_\mu}\,dx_{\nu_\mu} + \mu_\pi\,dx_\pi\,. \end{aligned} \tag{C.2}$$

We know from the allowed chemical reactions that $dx_n = -\,dx_p$, $dx_e = dx_p - dx_\mu - dx_\pi$, $dx_{\nu_e} = dx_\pi + dx_\mu - dx_p$, and $dx_{\nu_\mu} = -\,dx_\mu$ and so all particle fractions can be expressed in terms of the proton, muon, and pion fractions. We Legendre transform the temperature/entropy term [226], getting the final expression

$$\begin{aligned} d\left(\frac{\varepsilon - sT}{n_B}\right) = \frac{P}{n_B^2}\,dn_B - \frac{s}{n_B}\,dT - \delta\mu_1\,dx_p \\ + (\delta\mu_1 - \delta\mu_2)\,dx_\mu + (\delta\mu_1 - \delta\mu_3)\,dx_\pi\,. \end{aligned} \tag{C.3}$$

From this 1st law of thermodynamics, we can derive six Maxwell relations (if we only consider derivatives with respect to n_B or x_i) [226]. The three that are relevant are written in Eqs. 4.41, 4.42, and 4.43.

Appendix D: Weak interaction rate phase space integrals

1. Direct Urca (with electrons)

The rate (per volume) of the neutron decay process $n \rightarrow p + e^- + \bar{\nu}_e$ is

$$\Gamma = \int \frac{d^3p_n}{(2\pi)^3}\frac{d^3p_p}{(2\pi)^3}\frac{d^3p_e}{(2\pi)^3}\frac{d^3p_{\bar{\nu}_e}}{(2\pi)^3}(2\pi)^4\delta^4(p_n - p_p - p_e - p_{\bar{\nu}_e})\frac{\sum_{\text{spins}}|\mathcal{M}|^2}{2^4E_nE_pE_eE_{\bar{\nu}_e}}f_n(1-f_p)(1-f_e)(1-f_{\bar{\nu}_e}). \tag{D.1}$$

The matrix element is given by

$$\sum_{\text{spins}}|\mathcal{M}|^2 = 32G_F^2\cos^2\theta_c[(1+g_A)^2(p_p\cdot p_e)(p_n\cdot p_\nu) + (g_A^2-1)m^2(p_e\cdot p_\nu) \tag{D.2}$$

$$+ (g_A-1)^2(p_n\cdot p_e)(p_p\cdot p_\nu)], \tag{D.3}$$

but we will take the nucleons to be nonrelativistic and eliminate the (small) term that is proportional to $(1-g_A^2)$, which reduces the matrix element down to the momentum-independent quantity (see Appendix C in [227])

$$\frac{\sum_{\text{spins}}|\mathcal{M}|^2}{2^4E_nE_pE_eE_\nu} = 2G_F^2\cos^2\theta_c(1+3g_A^2). \tag{D.4}$$

The phase space integral reduces from 12 to 8 dimensions after integrating over the delta functions. Then a spherical coordinate system can be chosen in such a way to render three additional angular integrals trivial, leaving a 5-dimensional integral. Two more integrals can be done analytically, leaving a 3-dimensional integral to do numerically. This integral has been done with the full matrix element (Eq. D.3) with $g_A = 1$ in [81], with the non-relativistic matrix element D.4 in [75], and in the neutrino-transparent case in [77, 78].

The rate of the inverse electron capture process $n + \nu_e \rightarrow e^- + p$ is

$$\Gamma = \int \frac{d^3p_n}{(2\pi)^3}\frac{d^3p_p}{(2\pi)^3}\frac{d^3p_e}{(2\pi)^3}\frac{d^3p_{\nu_e}}{(2\pi)^3}(2\pi)^4\delta^4(p_n - p_p - p_e + p_{\nu_e})\frac{\sum_{\text{spins}}|\mathcal{M}|^2}{2^4E_nE_pE_eE_{\nu_e}}f_n(1-f_p)(1-f_e)f_{\nu_e}. \tag{D.5}$$

The matrix element for $n + \nu_e \rightarrow e^- + p$ is also given by Eq. D.4 (or Eq. D.3) due to crossing symmetry, and the phase space integration is done almost identically to the neutron decay case.

The direct Urca processes involving a muon are obtained by replacing the electron mass and chemical potential with the muon mass and chemical potential. While electrons can be treated as ultrarelativistic particles (though we do not assume this in our calculation), muons cannot be. The electron neutrino chemical potential is also changed to the muon neutrino chemical potential.

2. Electron-muon conversion

The rate of $\mu^- \to e^- + \bar{\nu}_e + \nu_\mu$ is

$$\Gamma = \int \frac{d^3p_\mu}{(2\pi)^3}\frac{d^3p_e}{(2\pi)^3}\frac{d^3p_{\bar{\nu}_e}}{(2\pi)^3}\frac{d^3p_{\nu_\mu}}{(2\pi)^3}(2\pi)^4\delta^4(p_\mu - p_e - p_{\bar{\nu}_e} - p_{\nu_\mu})\frac{\sum_{\text{spins}}|\mathcal{M}|^2}{2^4E_\mu E_e E_{\bar{\nu}_e}E_{\nu_\mu}}f_\mu(1-f_e)(1-f_{\bar{\nu}_e})(1-f_{\nu_\mu}). \tag{D.6}$$

The matrix element is given by

$$\sum_{\text{spins}}|\mathcal{M}|^2 = 128G_F^2(p_\mu\cdot p_{\nu_e})(p_{\nu_\mu}\cdot p_e). \tag{D.7}$$

The rate of $\mu^- + \bar{\nu}_\mu \to e^- + \bar{\nu}_e$ is

$$\Gamma = \int \frac{d^3p_\mu}{(2\pi)^3}\frac{d^3p_e}{(2\pi)^3}\frac{d^3p_{\bar{\nu}_e}}{(2\pi)^3}\frac{d^3p_{\bar{\nu}_\mu}}{(2\pi)^3}(2\pi)^4\delta^4(p_\mu - p_e - p_{\bar{\nu}_e} - p_{\bar{\nu}_\mu})\frac{\sum_{\text{spins}}|\mathcal{M}|^2}{2^4E_\mu E_e E_{\bar{\nu}_e}E_{\bar{\nu}_\mu}}f_\mu(1-f_e)(1-f_{\bar{\nu}_e})(1-f_{\bar{\nu}_\mu}). \tag{D.8}$$

The rate of $\mu^- + \nu_e \to e^- + \nu_\mu$ is

$$\Gamma = \int \frac{d^3p_\mu}{(2\pi)^3}\frac{d^3p_e}{(2\pi)^3}\frac{d^3p_{\nu_e}}{(2\pi)^3}\frac{d^3p_{\nu_\mu}}{(2\pi)^3}(2\pi)^4\delta^4(p_\mu - p_e - p_{\nu_e} - p_{\nu_\mu})\frac{\sum_{\text{spins}}|\mathcal{M}|^2}{2^4E_\mu E_e E_{\nu_e}E_{\nu_\mu}}f_\mu(1-f_e)(1-f_{\nu_e})(1-f_{\nu_\mu}). \tag{D.9}$$

The rate of $\mu^- + \nu_e + \bar{\nu}_\mu \to e^-$ is given by

$$\Gamma = \int \frac{d^3p_\mu}{(2\pi)^3}\frac{d^3p_e}{(2\pi)^3}\frac{d^3p_{\nu_e}}{(2\pi)^3}\frac{d^3p_{\bar{\nu}_\mu}}{(2\pi)^3}(2\pi)^4\delta^4(p_\mu - p_e - p_{\nu_e} - p_{\bar{\nu}_\mu})\frac{\sum_{\text{spins}}|\mathcal{M}|^2}{2^4E_\mu E_e E_{\nu_e}E_{\bar{\nu}_\mu}}f_\mu(1-f_e)(1-f_{\nu_e})(1-f_{\bar{\nu}_\mu}). \tag{D.10}$$

All four reactions in this section have the same matrix element (Eq. D.7) due to crossing symmetry. The phase space integration proceeds the same way as for the Urca processes, and is (briefly) described in [81].

Appendix E: Full expression for bulk viscosity

In this section, we give the definitions of P, Q, R, S, T, U in the expression for the bulk viscosity (Eq. 4.45). We keep C_3 in the expression, even though (as discussed in the main text), it vanishes. First, we define the variables

$$\begin{aligned}
a &\equiv A_1\lambda_1 + A_2\lambda_2 + A_3\lambda_3 \qquad \text{(E.1)}\\
b &\equiv B_1\lambda_1 + B_2\lambda_2 + B_3\lambda_3\\
c &\equiv C_1\lambda_1 + C_2\lambda_2 + C_3\lambda_3\\
d &\equiv D_1\lambda_1 + D_2\lambda_2 + D_3\lambda_3\\
e &\equiv A_1\lambda_6 - A_2(\lambda_2 + \lambda_5 + \lambda_6) + A_3\lambda_5\\
f &\equiv B_1\lambda_6 - B_2(\lambda_2 + \lambda_5 + \lambda_6) + B_3\lambda_5\\
g &\equiv C_1\lambda_6 - C_2(\lambda_2 + \lambda_5 + \lambda_6) + C_3\lambda_5\\
h &\equiv D_1\lambda_6 - D_2(\lambda_2 + \lambda_5 + \lambda_6) + D_3\lambda_5\\
i &\equiv A_1\lambda_4 + A_2\lambda_5 - A_3(\lambda_3 + \lambda_4 + \lambda_5)\\
j &\equiv B_1\lambda_4 + B_2\lambda_5 - B_3(\lambda_3 + \lambda_4 + \lambda_5)\\
k &\equiv C_1\lambda_4 + C_2\lambda_5 - C_3(\lambda_3 + \lambda_4 + \lambda_5)\\
l &\equiv D_1\lambda_4 + D_2\lambda_5 - D_3(\lambda_3 + \lambda_4 + \lambda_5).
\end{aligned}$$

Then,

$$
\begin{aligned}
P = {} & (A_1 - A_3)c^2f^2i - (A_1 - A_2)cdf^2i - 2(A_1 - A_3)bcfgi + (A_1 - A_2)bdfgi \\
& - A_1cdfgi + (A_1 - A_3)b^2g^2i + A_1bdg^2i + (A_1 - A_2)bcfhi + A_1c^2fhi - (A_1 - A_2)b^2ghi \\
& - A_1bcghi - (A_1 - A_3)c^2efj + (A_1 - A_2)cdefj + (A_1 - A_3)bcegj + A_1cdegj + (A_1 - A_3)acfgj \\
& - (A_1 - A_2)adfgj - (A_1 - A_3)abg^2j - A_1adg^2j - (A_1 - A_2)bcehj - A_1c^2ehj \\
& + (A_1 - A_2)abghj + A_1acghj + (A_1 - A_3)cdfij - (A_1 - A_2)d^2fij - (A_1 - A_3)dg^2ij \\
& - (A_1 - A_3)bchij + (A_1 - A_2)bdhij + (A_1 - A_3)cghij + (A_1 - A_2)dghij - (A_1 - A_2)ch^2ij \\
& - (A_1 - A_3)cdej^2 + (A_1 - A_2)d^2ej^2 + (A_1 - A_3)achj^2 - (A_1 - A_2)adhj^2 \\
& + (A_1 - A_3)bcefk - (A_1 - A_2)bdefk - (A_1 - A_3)acf^2k + (A_1 - A_2)adf^2k - (A_1 - A_3)b^2egk \\
& - A_1bdegk + (A_1 - A_3)abfgk + A_1adfgk + (A_1 - A_2)b^2ehk + A_1bcehk - (A_1 - A_2)abfhk \\
& - A_1acfhk - (A_1 - A_3)bdfik - A_1d^2fik + (A_1 - A_3)dfgik + (A_1 - A_3)b^2hik \\
& + A_1bdhik - (A_1 - A_3)cfhik + A_1dghik - A_1ch^2ik + (A_1 - A_3)bdejk + A_1d^2ejk \\
& + (A_1 - A_3)degjk - (A_1 - A_3)abhjk - A_1adhjk - (A_1 - A_2)dehjk - (A_1 - A_3)aghjk \\
& + (A_1 - A_2)ah^2jk - (A_1 - A_3)defk^2 - A_1dehk^2 + (A_1 - A_3)afhk^2 + A_1ah^2k^2 \\
& + (A_1 - A_2)bdfil + A_1cdfil - (A_1 - A_2)dfgil - A_1dg^2il - (A_1 - A_2)b^2hil \\
& - A_1bchil + (A_1 - A_2)cfhil + A_1cghil + (A_1 - A_3)bcejl - 2(A_1 - A_2)bdejl \\
& - A_1cdejl - (A_1 - A_3)acfjl + (A_1 - A_2)adfjl - (A_1 - A_3)cegjl + (A_1 - A_3)ag^2jl \\
& + (A_1 - A_2)abhjl + A_1achjl + (A_1 - A_2)cehjl - (A_1 - A_2)aghjl - (A_1 - A_3)b^2ekl \\
& - A_1bdekl + (A_1 - A_3)abfkl + A_1adfkl + (A_1 - A_3)cefkl + (A_1 - A_2)defkl + A_1degkl \\
& - (A_1 - A_3)afgkl + A_1cehkl - (A_1 - A_2)afhkl - 2A_1aghkl + (A_1 - A_2)b^2el^2 \\
& + A_1bcel^2 - (A_1 - A_2)abfl^2 - A_1acfl^2 - (A_1 - A_2)cefl^2 - A_1cegl^2 + (A_1 - A_2)afgl^2 \\
& + A_1ag^2l^2
\end{aligned}
\tag{E.2}
$$

$$\begin{aligned} Q = {} & (A_1 - A_2)b^2e + A_1bce - (A_1 - A_2)abf - A_1acf - (A_1 - A_2)cef - A_1ceg \\ & + (A_1 - A_2)afg + A_1ag^2 + (A_1 - A_3)b^2i + A_1bdi - 2(A_1 - A_3)cfi + (A_1 - A_2)dfi \\ & + (A_1 - A_3)g^2i - A_1chi - (A_1 - A_2)ghi - (A_1 - A_3)abj - A_1adj + (A_1 - A_3)cej \\ & - 2(A_1 - A_2)dej + (A_1 - A_2)ahj - (A_1 - A_3)dij - A_1dek + (A_1 - A_3)afk \\ & - (A_1 - A_3)egk + 2A_1ahk + (A_1 - A_2)ehk + (A_1 - A_3)hik - A_1dil - (A_1 - A_2)hil \\ & + (A_1 - A_3)ajl - (A_1 - A_3)ekl + A_1al^2 + (A_1 - A_2)el^2 \end{aligned} \tag{E.3}$$

$$R = A_1a + (A_1 - A_2)e + (A_1 - A_3)i \tag{E.4}$$

$$S = (dgj - chj - dfk + bhk + cfl - bgl)^2 \tag{E.5}$$

$$\begin{aligned} T = {} & c^2f^2 - 2bcfg + b^2g^2 + 2cdfj - 2dg^2j - 2bchj + 2cghj + d^2j^2 - 2bdfk \\ & + 2dfgk + 2b^2hk - 2cfhk - 2dhjk + h^2k^2 - 2bdjl + 2chjl + 2dfkl - 2ghkl \\ & + b^2l^2 - 2cfl^2 + g^2l^2 \end{aligned} \tag{E.6}$$

$$U = b^2 - 2cf + g^2 - 2dj + 2hk + l^2. \tag{E.7}$$

Appendix F: Bulk viscosity $\lambda_3 \to \infty$

In this section, we give the definitions of $\alpha, \beta, \gamma, \varepsilon$ in the expression for the bulk viscosity (Eq. 4.46). We set $C_3 = 0$, consistent with our EOS.

$$
\begin{aligned}
\alpha = {} & \frac{(\lambda_1+\lambda_4)(\lambda_2+\lambda_5)+(\lambda_1+\lambda_2+\lambda_4+\lambda_5)\lambda_6}{(B_3+D_3)^2} \\
& \times \Big\{ \big(\lambda_1+\lambda_4\big)\big[(A_3B_2-A_2B_3)D_1+(A_1B_3-A_3B_1)D_2+(A_2B_1-A_1B_2)D_3\big] \\
& \times \big[-(A_1-A_3)B_3C_1+(A_1-A_2)(B_3D_1-B_1D_3)-A_1C_1D_3\big] \\
& + \big(\lambda_2+\lambda_5\big)\big[(A_1-A_3)B_3C_2+(A_1-A_2)(B_2D_3-B_3D_2)+A_1C_2D_3\big] \\
& \times \big[(A_3B_2-A_2B_3)(C_1-D_1)+(A_1B_3-A_3B_1)(C_2-D_2)-(A_2B_1-A_1B_2)D_3 \\
& + A_3(C_1D_2-C_2D_1)+(A_1C_2-A_2C_1)D_3\big] \\
& + \lambda_6\big[(A_3B_2-A_2B_3)C_1+(A_1B_3-A_3B_1)C_2+A_3(C_1D_2-C_2D_1)+(A_1C_2-A_2C_1)D_3\big] \\
& \times \big[-(A_1-A_3)B_3(C_1-C_2)+(A_1-A_2)(B_3D_1-B_1D_3)+(A_1-A_2)(B_2D_3-B_3D_2) \\
& - A_1D_3(C_1-C_2)\big]\Big\}.
\end{aligned}
\tag{F.1}
$$

$$
\begin{aligned}
\beta = {} & (\lambda_1+\lambda_4)\left[A_1-\frac{A_3B_3}{B_3+D_3}\right]\left[A_1-A_3\frac{B_1+D_1}{B_3+D_3}\right]+(\lambda_2+\lambda_5)\left[A_2-\frac{A_3B_3}{B_3+D_3}\right]\left[A_2-A_3\frac{B_2+D_2}{B_3+D_3}\right] \\
& + \lambda_6(A_1-A_2)\left[(A_1-A_2)-A_3\frac{B_1-B_2+D_1-D_2}{B_3+D_3}\right]
\end{aligned}
\tag{F.2}
$$

$$
\gamma = [\lambda_6(\lambda_1+\lambda_2+\lambda_4+\lambda_5)+(\lambda_1+\lambda_4)(\lambda_2+\lambda_5)]^2\left[\frac{D_3(B_1C_2-B_2C_1)+B_3(C_1D_2-C_2D_1)}{B_3+D_3}\right]^2
\tag{F.3}
$$

$$
\varepsilon = \left(\frac{B_3D_1-B_1D_3}{B_3+D_3}\right)^2(\lambda_1+\lambda_4)^2-2\frac{B_3D_2-B_2D_3}{B_3+D_3}\left(C_1+\frac{B_1D_3-B_3D_1}{B_3+D_3}\right)(\lambda_1+\lambda_4)(\lambda_2+\lambda_5)
\tag{F.4}
$$

$$
\begin{aligned}
& + \left(C_2+\frac{B_2D_3-B_3D_2}{B_3+D_3}\right)^2(\lambda_2+\lambda_5)^2+2C_1\left(\frac{B_3(D_1-D_2)-(B_1-B_2)D_3}{B_3+D_3}\right)(\lambda_1+\lambda_4)\lambda_6 \\
& - 2C_2\left(C_1-C_2-\frac{B_3(D_1-D_2)-D_3(B_1-B_2)}{B_3+D_3}\right)(\lambda_2+\lambda_5)\lambda_6+(C_1-C_2)^2\lambda_6^2.
\end{aligned}
\tag{F.5}
$$

Appendix G: Bulk viscosity without pions

In this section, we give the definitions of $\tilde{\alpha}$, $\tilde{\beta}$, $\tilde{\gamma}$, in the bulk viscosity expression Eq. 4.47

$$\begin{aligned}\tilde{\alpha} = [\lambda_2\lambda_6 + \lambda_1(\lambda_2+\lambda_6)]\Big\{&(A_1B_2 - A_2B_1)[(A_1-A_2)B_1 + A_1C_1]\lambda_1 \\ &+ [(A_1-A_2)B_2 + A_1C_2][A_1(B_2+C_2) - A_2(B_1+C_1)]\lambda_2 \\ &- (A_1C_2 - A_2C_1)[(A_1-A_2)(B_1-B_2) + A_1(C_1-C_2)]\lambda_6\Big\}\end{aligned} \tag{G.1}$$

$$\tilde{\beta} = A_1^2\lambda_1 + A_2^2\lambda_2 + (A_1-A_2)^2\lambda_6 \tag{G.2}$$

$$\tilde{\gamma} = (B_2C_1 - B_1C_2)^2[\lambda_2\lambda_6 + \lambda_1(\lambda_2+\lambda_6)]^2 \tag{G.3}$$

$$\begin{aligned}\tilde{\varepsilon} = {}&B_1^2\lambda_1^2 + 2B_2(B_1+C_1)\lambda_1\lambda_2 + (B_2+C_2)^2\lambda_2^2 - 2(B_1-B_2)C_1\lambda_1\lambda_6 \\ &- 2C_2(B_1 - B_2 + C_1 - C_2)\lambda_2\lambda_6 + (C_1-C_2)^2\lambda_6^2\end{aligned} \tag{G.4}$$

Ref. [81] studied bulk viscosity in $npe^-\mu^-\nu_e\nu_\mu$ matter in the cases where $\lambda_6 \to 0$ and $\lambda_6 \to \infty$. In the limit $\lambda_6 \to 0$, our expression simplifies to

$$\begin{aligned}\zeta = {}&\frac{(A_1B_2 - A_2B_1)[(A_1-A_2)B_1 + A_1C_1]\lambda_1^2\lambda_2}{(B_2C_1 - B_1C_2)^2\lambda_1^2\lambda_2^2 + [B_1^2\lambda_1^2 + 2B_2(B_1+C_1)\lambda_1\lambda_2 + (B_2+C_2)^2\lambda_2^2]\,\omega^2 + \omega^4} \\ &+ \frac{[(A_1-A_2)B_2 + A_1C_2][A_1(B_2+C_2) - A_2(B_1+C_1)]\lambda_1\lambda_2^2}{(B_2C_1 - B_1C_2)^2\lambda_1^2\lambda_2^2 + [B_1^2\lambda_1^2 + 2B_2(B_1+C_1)\lambda_1\lambda_2 + (B_2+C_2)^2\lambda_2^2]\,\omega^2 + \omega^4} \\ &+ \frac{(A_1^2\lambda_1 + A_2^2\lambda_2)\omega^2}{(B_2C_1 - B_1C_2)^2\lambda_1^2\lambda_2^2 + [B_1^2\lambda_1^2 + 2B_2(B_1+C_1)\lambda_1\lambda_2 + (B_2+C_2)^2\lambda_2^2]\,\omega^2 + \omega^4}.\end{aligned} \tag{G.5}$$

In the limit where $\lambda_6 \to \infty$,

$$\zeta = \frac{\left(\dfrac{A_2C_1 - A_1C_2}{C_1 - C_2}\right)\left[A_1 + \dfrac{(A_1-A_2)(B_1-B_2)}{C_1-C_2}\right](\lambda_1+\lambda_2)}{\left(\dfrac{B_2C_1 - B_1C_2}{C_1-C_2}\right)^2(\lambda_1+\lambda_2)^2 + \omega^2} \tag{G.6}$$

Appendix H: Integrals $I(\omega; A, B)$ and $K(\omega; A, B)$

In this appendix, we reduce the integrals $I(\omega; A, B)$ and $K(\omega; A, B)$ appearing in Π_{pw}. Using the techniques described in [200], the integral I of Eq.6.16 can be reduced to

$$
\begin{aligned}
I(\omega; A, B) &= \int \frac{d^3l d^3k}{(2\pi)^6} \theta(A-l)\theta(B-k) \frac{(l-k)^2}{(l-k)^2 + m_\pi^2 - \omega^2 - i0^+} \\
&= \frac{(A+B)^6}{192\pi^4} \left(\left[(1-r)^3 f_1(r,\xi) + f_2(r,\xi)\right] + \frac{i\pi}{2} \left|\xi\right| \theta(1 - |\xi|^{1/2}) \theta(-\xi) \chi(|\xi|^{1/2}) \right)
\end{aligned}
\tag{H.1}
$$

where

$$
\begin{aligned}
r &= \frac{|A-B|}{A+B} \\
\xi &= \frac{m_\pi^2 - \omega^2}{(A+B)^2} \\
\chi(z) &= 2z(1-r)^3\theta(r-z) + (1-z)^2(z^2 + 2z - 3r^2)\theta(z-r) \\
f_1(r,\xi) &= P \int_0^1 dz \; \frac{2z^4}{z^2+\xi} \theta(r-z) \\
f_2(r,\xi) &= P \int_0^1 dz \; \frac{z^3(1-z)^2(z^2+2z-3r^2)}{z^2+\xi} \theta(z-r)
\end{aligned}
$$

and where the P indicates a principal value integral. Both f_1 and f_2 have piecewise closed-form expressions easily computed on computer algebra systems, but the expressions are long; for these reasons neglect them here. However, when $A = B$ expressions simplify and we print them here:

$$
\begin{aligned}
I(\omega; A, A) &= \frac{A^6}{3\pi^4} \left[\frac{1}{12} + \frac{1}{2s^2} + \frac{3}{4s} - \frac{2\tanh^{-1}(\sqrt{s})}{s^{3/2}} + \log(1-s) \Big(\frac{1}{2s^3} - \frac{3}{2s^2} \Big) \right], \; s < 0 \\
&= \frac{A^6}{3\pi^4} \Bigg[\frac{1}{12} + \frac{1}{2s^2} + \frac{3}{4s} - s^{-3/2} \log\Big(\frac{1+\sqrt{s}}{|1-\sqrt{s}|} \Big) + \log(|1-s|) \Big(\frac{1}{2s^3} - \frac{3}{2s^2} \Big) \\
&\qquad + \frac{i\pi}{2} \theta(s-1) \Big(\frac{1}{s^3} - \frac{3}{s^2} + \frac{2}{s^{3/2}} \Big) \Bigg], \; s > 0 \,.
\end{aligned}
\tag{H.2}
$$

where $s = \frac{4A^2}{\omega^2 - m_\pi^2}$. The integral K of Eq.6.16 can be reduced to the following two-dimensional integral

$$\begin{aligned} K(\omega; A, B) =& \int \frac{d^3l d^3k}{(2\pi)^6} \theta(A-l)\theta(B-k) \frac{2(l^2-k^2)}{(l-k)^2 + m_\pi^2 - \omega^2 - i0^+} \\ =& \frac{1}{(2\pi)^4} \int_0^A dl \int_0^B dk\ 2kl(l^2-k^2) \times \\ & \left\{ \log(\frac{1+\zeta}{1-\zeta})\theta(1-|\zeta|) + \log(\frac{\zeta+1}{\zeta-1})\theta(|\zeta|-1) + i\pi\theta(1-|\zeta|) \right\} \end{aligned} \tag{H.3}$$

where

$$\zeta = \frac{l^2 + k^2 + m_\pi^2 - \omega^2}{2lk} .$$

---

[1] R. Bollig, H. T. Janka, A. Lohs, et al. Muon Creation in Supernova Matter Facilitates Neutrino-Driven Explosions. *Physical Review Letters*, 119(24):242702, dec 2017.

[2] Norman K. Glendenning. *Compact stars: Nuclear physics, particle physics, and general relativity.* Springer, New York, 1997.

[3] H. Th Janka, K. Langanke, A. Marek, et al. Theory of core-collapse supernovae. *Physics Reports*, 442(1-6):38–74, apr 2007.

[4] Tobias Fischer, Niels Uwe Bastian, David Blaschke, et al. The state of matter in simulations of core-collapse supernovae-reflections and recent developments, dec 2017.

[5] J. M. Lattimer and M. Prakash. The Physics of Neutron Stars, apr 2004.

[6] Hans Thomas Janka. Explosion mechanisms of core-collapse supernovae. *Annual Review of Nuclear and Particle Science*, 62:407–415, 2012.

[7] A. Burrows and D. Vartanyan. Core-collapse supernova explosion theory, jan 2021.

[8] Gordon Baym and Christopher Pethick. NEUTRON STARS. *Annu Rev Nucl Sci*, 25, nov 1975.

[9] Luke F. Roberts and Sanjay Reddy. *Neutrino Signatures from Young Neutron Stars*, pages 1605–1635. Springer International Publishing, Cham, 2017.

[10] Georg G. Raffelt. *Stars as Laboratories for Fundamental Physics.* Chicago University Pres, Chicago, 1996.

[11] R. M. Bionta, G. Blewitt, C. B. Bratton, et al. Observation of a neutrino burst in coincidence with supernova 1987A in the Large Magellanic Cloud. *Physical Review Letters*, 58(14):1494–1496, apr 1987.

[12] K. Hirata, T. Kajita, M. Koshiba, et al. Observation of a neutrino burst from the supernova SN1987A. *Physical Review Letters*, 58(14):1490–1493, apr 1987.

[13] M. Oertel, M. Hempel, T. Klähn, and S. Typel. Equations of state for supernovae and compact stars. *Reviews of Modern Physics*, 89(1):15007, 2017.

[14] L. Woltjer. X-Rays and Type i Supernova Remnants. *The Astrophysical Journal*, 140:1309, oct 1964.

[15] H. T. Cromartie, E. Fonseca, S. M. Ransom, et al. Relativistic Shapiro delay measurements of an extremely massive millisecond pulsar, sep 2020.

[16] Michela Mapelli and Nicola Giacobbo. The cosmic merger rate of neutron stars and black holes. *Monthly Notices of the Royal Astronomical Society*, 479(4):4391–4398, oct 2018.

[17] Michele Maggiore, Chris Van Den Broeck, Nicola Bartolo, et al. Science case for the Einstein telescope, mar 2020.

[18] Jocelyn S. Read, Luca Baiotti, Jolien D.E. Creighton, et al. Matter effects on binary neutron star waveforms. *Physical Review D - Particles, Fields, Gravitation and Cosmology*, 88(4):044042, aug 2013.

[19] Albino Perego, Sebastiano Bernuzzi, and David Radice. Thermodynamics conditions of matter in neutron star mergers. *European Physical Journal A*, 55(8):124, aug 2019.

[20] Stefan Scherer. Introduction to Chiral Perturbation Theory. In *Advances in Nuclear Physics, Volume 27*, pages 277–538. Springer, Boston, MA, dec 2005.

[21] P. A. Zyla, R. M. Barnett, J. Beringer, et al. Review of particle physics, aug 2020.

[22] David B. Kaplan. Five lectures on effective field theory. oct 2005.

[23] V. BERNARD, N. KAISER, and ULF-G. MEIßNER. CHIRAL DYNAMICS IN NUCLEONS AND NUCLEI. *International Journal of Modern Physics E*, 04(02):193–344, jan 1995.

[24] David Griffths. *Introductory to Elementary Particles.* Wiley, 2nd ed. edition, 2008.

[25] Madappa Prakash, Ignazio Bombaci, Manju Prakash, et al. Composition and structure of protoneutron stars. *Physics Report*, 280(1):1–77, 1997.

[26] Bryce Fore and Sanjay Reddy. Pions in hot dense matter and their astrophysical implications. *Physical Review C*, 101(3):35809, mar 2020.

[27] Richard C. Tolman. Static solutions of einstein's field equations for spheres of fluid. *Physical Review*, 55(4):364–373, feb 1939.

[28] J. R. Oppenheimer and G. M. Volkoff. On massive neutron cores. *Physical Review*, 55(4):374–381, feb 1939.

[29] G. Raaijmakers, S. K. Greif, T. E. Riley, et al. Constraining the Dense Matter Equation of State with Joint Analysis of NICER and LIGO/Virgo Measurements. *The Astrophysical Journal*, 893(1):L21, apr 2020.

[30] T. H.R. Skyrme. The effective nuclear potential. *Nuclear Physics*, 9(4):615–634, 1958.

[31] A. W. Steiner, M. Prakash, J. M. Lattimer, and P. J. Ellis. Isospin asymmetry in nuclei and neutron stars. *Physics Reports*, 411(6):325–375, 2005.

[32] Gordon Baym, Christopher Pethick, and Peter Sutherland. The Ground State of Matter at High Densities: Equation of State and Stellar Models. *The Astrophysical Journal*, 170:299, dec 1971.

[33] J. W. Negele and D. Vautherin. Neutron star matter at sub-nuclear densities. *Nuclear Physics, Section A*, 207(2):298–320, jun 1973.

[34] E. Epelbaum, H. W. Hammer, and Ulf G. Meißner. Modern theory of nuclear forces. *Reviews of Modern Physics*, 81(4):1773–1825, 2009.

[35] A. B. Migdal. Phase transitions (π-condensation) in nuclei and neutron stars. *Physics Letters B*, 45(5):448–450, 1973.

[36] R. F. Sawyer. Condensed π- Phase in neutron-star matter. *Physical Review Letters*, 29(6):382–385, aug 1972.

[37] A. B. Migdal. Pion fields in nuclear matter. *Reviews of Modern Physics*, 50(1):107–172, jan 1978.

[38] W. Weise and G. E. Brown. Equation of state for neutron matter in the presence of a pion condensate. *Physics Letters B*, 58(3):300–303, 1975.

[39] S. O. Bäckman and W. Weise. Calculation of the threshold for π- condensation in neutron matter. *Physics Letters B*, 55(1):1–5, 1975.

[40] A. B. Migdal, E. E. Saperstein, M. A. Troitsky, and D. N. Voskresensky. Pion degrees of freedom in nuclear matter. *Physics Reports*, 192(4-6):179–437, sep 1990.

[41] A. Akmal and V. R. Pandharipande. Spin-isospin structure and pion condensation in nucleon matter. *Physical Review C - Nuclear Physics*, 56(4):2261–2279, 1997.

[42] D. B. Kaplan and A. E. Nelson. Strange goings on in dense nucleonic matter. *Physics Letters B*, 175(1):57–63, jul 1986.

[43] D. B. Kaplan and A. E. Nelson. Kaon condensation in dense matter. *Nuclear Physics, Section A*, 479(C):273–284, mar 1988.

[44] Hideyuki Umeda, Sachiko Tsuruta, and Ken'ichi Nomoto. Nonstandard thermal evolution of neutron stars. *The Astrophysical Journal*, 433:256, sep 1994.

[45] N. Kaiser and W. Weise. Systematic calculation of s-wave pion and kaon self-energies in asymmetric nuclear matter. *Physics Letters, Section B: Nuclear, Elementary Particle and High-Energy Physics*, 512(3-4):283–289, jul 2001.

[46] Vesteinn Thorsson, Madappa Prakash, and James M. Lattimer. Composition, structure and evolution of neutron stars with kaon condensates. *Nuclear Physics A*, 572(3-4):693–731, may 1994.

[47] Roger Dashen, Shang Keng Ma, and Herbert J. Bernstein. S-matrix formulation of statistical mechanics. *Physical Review*, 187(1):345–370, nov 1969.

[48] Raju Venugopalan and Madappa Prakash. Thermal properties of interacting hadrons. *Nuclear Physics, Section A*, 546(4):718–760, 1992.

[49] Pasi Huovinen and Peter Petreczky. Hadron resonance gas with repulsive interactions and fluctuations of conserved charges. *Physics Letters, Section B: Nuclear, Elementary Particle and High-Energy Physics*, 777:125–130, 2018.

[50] C. J. Horowitz and A. Schwenk. The virial equation of state of low-density neutron matter. *Physics Letters, Section B: Nuclear, Elementary Particle and High-Energy Physics*, 638(2-3):153–159, 2006.

[51] M. Dutra, O. Lourenço, J. S. Sá Martins, et al. Skyrme interaction and nuclear matter constraints. *Physical Review C - Nuclear Physics*, 85(3):35201, 2012.

[52] I. Tews, T. Krüger, K. Hebeler, and A. Schwenk. Neutron matter at next-to-next-to-next-to-leading order in chiral effective field theory. *Physical Review Letters*, 110(3):32504, 2013.

[53] S. Gandolfi, J. Carlson, S. Reddy, et al. The equation of state of neutron matter, symmetry energy and neutron star structure. *European Physical Journal A*, 50(2):1–11, 2014.

[54] Pok Man Lo. S-matrix formulation of thermodynamics with N-body scatterings. *European Physical Journal C*, 77(8):533, aug 2017.

[55] Martin Hoferichter, Jacobo Ruiz de Elvira, Bastian Kubis, and Ulf G. Meißner. Roy-Steiner-equation analysis of pion-nucleon scattering. *Physics Reports*, 625:1–88, 2016.

[56] Ulf G. Meißner, José A. Oller, and Andreas Wirzba. In-medium chiral perturbation theory beyond the mean-field approximation. *Annals of Physics*, 297(1):27–66, 2002.

[57] Martin Hoferichter, Jacobo Ruiz De Elvira, Bastian Kubis, and Ulf G. Meißner. Matching Pion-Nucleon Roy-Steiner Equations to Chiral Perturbation Theory. *Physical Review Letters*, 115(19):192301, 2015.

[58] G. D. Mahan. *Many Particle Physics, Third Edition.* Plenum, New York, 2000.

[59] A. Burrows and J. M. Lattimer. The birth of neutron stars. *The Astrophysical Journal*, 307:178, 1986.

[60] J. A. Pons, S. Reddy, M. Prakash, et al. Evolution of Proto–Neutron Stars. *The Astrophysical Journal*, 513(2):780–804, 1999.

[61] Yuichiro Sekiguchi, Kenta Kiuchi, Koutarou Kyutoku, and Masaru Shibata. Gravitational waves and neutrino emission from the merger of binary neutron stars. *Physical Review Letters*, 107(5):51102, 2011.

[62] Sanjay Reddy, Madappa Prakash, and James Lattimer. Neutrino interactions in hot and dense matter. *Physical Review D - Particles, Fields, Gravitation and Cosmology*, 58(1):27, 1998.

[63] Mark G. Alford and Steven P. Harris. β equilibrium in neutron-star mergers. *Physical Review C*, 98(6):065806, dec 2018.

[64] J. Gasser and G. R.S. Zarnauskas. On the pion decay constant. *Physics Letters, Section B: Nuclear, Elementary Particle and High-Energy Physics*, 693(2):122–128, 2010.

[65] C. J. Horowitz and K. Wehrberger. Neutrino neutral current interactions in nuclear matter. *Nuclear Physics, Section A*, 531(3-4):665–684, 1991.

[66] Sanjay Reddy, Madappa Prakash, James M. Lattimer, and Jose A. Pons. Effects of strong and electromagnetic correlations on neutrino interactions in dense matter. *Physical Review C - Nuclear Physics*, 59(5):2888–2918, 1999.

[67] Luke F. Roberts and Sanjay Reddy. Charged current neutrino interactions in hot and dense matter. *Physical Review C*, 95(4):45807, apr 2017.

[68] Curt Cutler, Lee Lindblom, and Randall J. Splinter. Damping times for neutron star oscillations. *The Astrophysical Journal*, 363:603, nov 1990.

[69] Mark G. Alford, Luke Bovard, Matthias Hanauske, et al. Viscous Dissipation and Heat Conduction in Binary Neutron-Star Mergers. *Physical Review Letters*, 120(4):41101, 2018.

[70] Raymond F. Sawyer. Bulk viscosity of hot neutron-star matter and the maximum rotation rates of neutron stars. *Physical Review D*, 39(12):3804–3806, jun 1989.

[71] Mark G. Alford, Simin Mahmoodifar, and Kai Schwenzer. Large amplitude behavior of the bulk viscosity of dense matter. *Journal of Physics G: Nuclear and Particle Physics*, 37(12):125202, nov 2010.

[72] B. T. Goodwin and C. J. Pethick. Transport properties of degenerate neutrinos in dense matter. *The Astrophysical Journal*, 253:816, feb 1982.

[73] L. VAN DEN HORN and C. VAN WEERT. Transport properties of neutrinos in stellar collapse. II: Shear viscosity, heat construction, and diffusion. *Astronomy and astrophysics (Berlin. Print)*, 136(1):74–80, 1984.

[74] Mark G. Alford and Steven P. Harris. Damping of density oscillations in neutrino-transparent nuclear matter. *Physical Review C*, 100(3):35803, 2019.

[75] Mark Alford, Arus Harutyunyan, and Armen Sedrakian. Bulk viscosity of baryonic matter with trapped neutrinos. *Physical Review D*, 100(10), 2019.

[76] Steven P. Harris, Bryce Fore, and Sanjay Reddy. Pion contribution to the bulk viscosity of neutrino-trapped nuclear matter. 2022.

[77] Mark G. Alford, Alexander Haber, Steven P. Harris, and Ziyuan Zhang. Beta equilibrium under neutron star merger conditions. *Universe 2021, Vol. 7, Page 399*, 7(11):399, oct 2021.

[78] Mark G. Alford and Steven P. Harris. ¡math¿ ¡mi¿β¡/mi¿ ¡/math¿ equilibrium in neutron-star mergers. *Physical Review C*, 98(6):065806, dec 2018.

[79] D. Greiner, W. and Neise, L. and Stocker, H. and Rischke. *Thermodynamics and statistical mechanics*. Springer-Verlag, 1995.

[80] Andreas Reisenegger. Deviations from chemical equilibrium due to spin-down as an internal heat source in neutron stars. *The Astrophysical Journal*, 442:749, oct 1995.

[81] Mark Alford, Arus Harutyunyan, and Armen Sedrakian. Bulk viscosity from Urca processes: $npe\mu$-neutrino-trapped matter. aug 2021.

[82] Mikhail E. Gusakov and Elena M. Kantor. Bulk viscosity of superfluid hyperon stars. *Physical Review D - Particles, Fields, Gravitation and Cosmology*, 78(8):083006, oct 2008.

[83] P. B. Jones. Bulk viscosity of neutron-star matter. *Physical Review D*, 64(8):084003, sep 2001.

[84] Mark G. Alford and Alexander Haber. Strangeness-changing rates and hyperonic bulk viscosity in neutron star mergers. *Physical Review C*, 103(4):045810, apr 2021.

[85] R D Peccei and Helen R Quinn. CP Conservation in the Presence of Instantons. *Phys. Rev. Lett.*, 38:1440–1443, 1977.

[86] R D Peccei and Helen R Quinn. Constraints Imposed by CP Conservation in the Presence of Instantons. *Phys. Rev. D*, 16:1791–1797, 1977.

[87] Steven Weinberg. A New Light Boson? *Physical Review Letters*, 40(4):223, jan 1978.

[88] Frank Wilczek. Problem of Strong ¡math display="inline"¿ ¡mi¿P¡/mi¿ ¡/math¿ and ¡math display="inline"¿ ¡mi¿T¡/mi¿ ¡/math¿ Invariance in the Presence of Instantons. *Physical Review Letters*, 40(5):279–282, jan 1978.

[89] Paolo Di Vecchia, Maurizio Giannotti, Massimiliano Lattanzi, and Axel Lindner. Round Table on Axions and Axion-like Particles. *PoS*, Confinemen:34, sep 2019.

[90] Luca Di Luzio, Maurizio Giannotti, Enrico Nardi, and Luca Visinelli. The landscape of QCD axion models. *Phys. Rept.*, 870:1–117, 2020.

[91] Prateek Agrawal and Others. Feebly-Interacting Particles:FIPs 2020 Workshop Report. 2021.

[92] Giovanni di Cortona, Edward Hardy, Javier Pardo Vega, and Giovanni Villadoro. The QCD axion, precisely. *JHEP*, 01:34, 2016.

[93] Sz. Borsanyi and Others. Calculation of the axion mass based on high-temperature lattice quantum chromodynamics. *Nature*, 539(7627):69–71, 2016.

[94] Igor G. Irastorza and Javier Redondo. New experimental approaches in the search for axion-like particles. *Progress in Particle and Nuclear Physics*, 102:89–159, sep 2018.

[95] Pierre Sikivie. Invisible Axion Search Methods. *Reviews of Modern Physics*, 93(1):15004, mar 2021.

[96] Georg G Raffelt. Astrophysical axion bounds. *Lect. Notes Phys.*, 741:51–71, 2008.

[97] Maurizio Giannotti, Igor Irastorza, Javier Redondo, and Andreas Ringwald. Cool WISPs for stellar cooling excesses. *Journal of Cosmology and Astroparticle Physics*, 2016(5):057, may 2016.

[98] Maurizio Giannotti, Igor G. Irastorza, Javier Redondo, et al. Stellar recipes for Axion hunters. *Journal of Cosmology and Astroparticle Physics*, 2017(10):010, oct 2017.

[99] Pierluca Carenza, Tobias Fischer, Maurizio Giannotti, et al. Improved axion emissivity from a supernova via nucleon-nucleon bremsstrahlung. *Journal of Cosmology and Astroparticle Physics*, 2019(10):016, oct 2019.

[100] Alexandre Payez, Carmelo Evoli, Tobias Fischer, et al. Revisiting the SN1987A gamma-ray limit on ultralight axion-like particles. *JCAP*, 02:6, 2015.

[101] Francesca Calore, Pierluca Carenza, Maurizio Giannotti, et al. Bounds on axionlike particles from the diffuse supernova flux. *Phys. Rev. D*, 102(12):123005, 2020.

[102] Robert Bollig, William DeRocco, Peter W Graham, and Hans-Thomas Janka. Muons in supernovae: implications for the axion-muon coupling. *Phys. Rev. Lett.*, 125(5):51104, 2020.

[103] L. F. Abbott and P. Sikivie. A cosmological bound on the invisible axion. *Physics Letters B*, 120(1-3):133–136, jan 1983.

[104] John Preskill, Mark B. Wise, and Frank Wilczek. Cosmology of the invisible axion. *Physics Letters B*, 120(1-3):127–132, jan 1983.

[105] Michael Dine and Willy Fischler. The not-so-harmless axion. *Physics Letters B*, 120(1-3):137–141, jan 1983.

[106] S Borsanyi, M Dierigl, Z Fodor, et al. Axion cosmology, lattice QCD and the dilute instanton gas. *Phys. Lett. B*, 752:175–181, 2016.

[107] Andreas Ringwald. Alternative dark matter candidates: Axions. *PoS*, NOW2016:81, jun 2016.

[108] N. Du, Others, N. Force, et al. A Search for Invisible Axion Dark Matter with the Axion Dark Matter Experiment. *Phys. Rev. Lett.*, 120(15):151301, apr 2018.

[109] T Braine and Others. Extended Search for the Invisible Axion with the Axion Dark Matter Experiment. *Phys. Rev. Lett.*, 124(10):101303, 2020.

[110] P. Brun, A. Caldwell, L. Chevalier, et al. A new experimental approach to probe QCD axion dark matter in the mass range above 40μeV. *European Physical Journal C*, 79(3):1–16, mar 2019.

[111] Marco Gorghetto, Edward Hardy, and Giovanni Villadoro. Axions from strings: the attractive solution. *Journal of High Energy Physics 2018 2018:7*, 2018(7):1–57, jul 2018.

[112] Marco Gorghetto, Edward Hardy, and Giovanni Villadoro. More Axions from Strings. *SciPost Physics*, 10(2):050, feb 2020.

[113] Andreas Ringwald and Ken'ichi Saikawa. Axion dark matter in the post-inflationary Peccei-Quinn symmetry breaking scenario. *Physical Review D*, 93(8):085031, apr 2016.

[114] Georg G. Raffelt, Javier Redondo, and Nicolas Viaux Maira. The meV mass frontier of axion physics. *Physical Review D*, 84(10):103008, nov 2011.

[115] Luca Di Luzio, Marco Fedele, Maurizio Giannotti, et al. Solar Axions Cannot Explain the XENON1T Excess. *Physical Review Letters*, 125(13):131804, sep 2020.

[116] J Isern, E García-Berro, S Torres, et al. Axions and the luminosity function of white dwarfs: the thin and thick discs, and the halo. *Monthly Notices of the Royal Astronomical Society*, 478(2):2569–2575, aug 2018.

[117] Mikhail V. Beznogov, Ermal Rrapaj, Dany Page, and Sanjay Reddy. Constraints on axion-like particles and nucleon pairing in dense matter from the hot neutron star in HESS J1731-347. *Physical Review C*, 98(3):035802, sep 2018.

[118] Pierluca Carenza, Bryce Fore, Maurizio Giannotti, et al. Enhanced Supernova Axion Emission and Its Implications. *Physical Review Letters*, 126(7):071102, feb 2021.

[119] Tobias Fischer, Pierluca Carenza, Bryce Fore, et al. Observable signatures of enhanced axion emission from protoneutron stars. *Physical Review D*, 104(10):103012, nov 2021.

[120] Michael S. Turner. Axions from SN1987A. *Physical Review Letters*, 60(18):1797–1800, may 1988.

[121] Adam Burrows, Michael S. Turner, and R. P. Brinkmann. Axions and SN 1987A. *Physical Review D*, 39(4):1020–1028, feb 1989.

[122] Adam Burrows, M. Ted Ressell, and Michael S. Turner. Axions and SN 1987A: Axion trapping. *Physical Review D*, 42(10):3297–3309, nov 1990.

[123] Christoph Hanhart, Daniel R. Phillips, and Sanjay Reddy. Neutrino and axion emissivities of neutron stars from nucleon-nucleon scattering data. *Physics Letters, Section B: Nuclear, Elementary Particle and High-Energy Physics*, 499(1-2):9–15, feb 2001.

[124] Georg Raffelt and David Seckel. Multiple-scattering suppression of the bremsstrahlung emission of neutrinos and axions in supernovae. *Physical Review Letters*, 67(19):2605–2608, nov 1991.

[125] Steen Hannestad and Georg Raffelt. Supernova Neutrino Opacity from Nucleon-Nucleon Bremsstrahlung and Related Processes. *The Astrophysical Journal*, 507(1):339–352, nov 1998.

[126] Georg Raffelt and Thomas Strobel. Reduction of weak interaction rates in neutron stars by nucleon spin fluctuations: Degenerate case. *Physical Review D - Particles, Fields, Gravitation and Cosmology*, 55(2):523–527, jan 1997.

[127] Michael S Turner. Dirac neutrinos and SN1987A. *Phys. Rev. D*, 45:1066–1075, 1992.

[128] Georg Raffelt and David Seckel. A selfconsistent approach to neutral current processes in supernova cores. *Phys. Rev. D*, 52:1780–1799, 1995.

[129] Wolfgang Keil, Hans-Thomas Janka, David N Schramm, et al. A Fresh look at axions and SN-1987A. *Phys. Rev. D*, 56:2419–2432, 1997.

[130] Irene Tamborra, Lorenz Huedepohl, Georg Raffelt, and Hans-Thomas Janka. Flavor-dependent neutrino angular distribution in core-collapse supernovae. *Astrophys. J.*, 839:132, 2017.

[131] Jihn E Kim. Weak Interaction Singlet and Strong CP Invariance. *Phys. Rev. Lett.*, 43:103, 1979.

[132] Mikhail A Shifman, A I Vainshtein, and Valentin I Zakharov. Can Confinement Ensure Natural CP Invariance of Strong Interactions? *Nucl. Phys. B*, 166:493–506, 1980.

[133] A R Zhitnitsky. On Possible Suppression of the Axion Hadron Interactions. (In Russian). *Sov. J. Nucl. Phys.*, 31:260, 1980.

[134] Michael Dine, Willy Fischler, and Mark Srednicki. A Simple Solution to the Strong CP Problem with a Harmless Axion. *Phys. Lett. B*, 104:199–202, 1981.

[135] A Bartl, C J Pethick, and A Schwenk. Supernova matter at subnuclear densities as a resonant Fermi gas: Enhancement of neutrino rates. *Phys. Rev. Lett.*, 113:81101, 2014.

[136] Tobias Fischer, Gang Guo, Gabriel Martínez-Pinedo, et al. Muonization of supernova matter. *Physical Review D*, 102(12):123001, dec 2020.

[137] Anton Andronic, Peter Braun-Munzinger, Krzysztof Redlich, and Johanna Stachel. Decoding the phase structure of QCD via particle production at high energy. *Nature (London)*, 561(7723):321–330, 2018.

[138] J R Wilson and R W Mayle. Report on the progress of supernova research by the Livermore group. *Phys.Rept.*, 227:97–111, 1993.

[139] A. Akmal, V. R. Pandharipande, and D. G. Ravenhall. Equation of state of nucleon matter and neutron star structure. *Physical Review C - Nuclear Physics*, 58(3):1804–1828, 1998.

[140] A.∼S. Schneider, C Constantinou, B Muccioli, and M Prakash. Akmal-Pandharipande-Ravenhall equation of state for simulations of supernovae, neutron stars, and binary mergers. *Phys. Rev. C*, 100(2):25803, 2019.

[141] Georg Raffelt and David Seckel. Bounds on Exotic Particle Interactions from SN 1987a. *Phys. Rev. Lett.*, 60:1793, 1988.

[142] Michael S Turner. Axions from SN 1987a. *Phys. Rev. Lett.*, 60:1797, 1988.

[143] Adam Burrows, M.Ted Ressell, and Michael S Turner. Axions and SN1987A: Axion trapping. *Phys. Rev. D*, 42:3297–3309, 1990.

[144] Georg G Raffelt. Astrophysical methods to constrain axions and other novel particle phenomena. *Phys. Rept.*, 198:1–113, 1990.

[145] Tobias Fischer, Sovan Chakraborty, Maurizio Giannotti, et al. Probing axions with the neutrino signal from the next galactic supernova. *Phys. Rev. D*, 94(8):85012, 2016.

[146] Wolfgang Keil, H.Thomas Janka, and Ewald Muller. Ledoux convection in protoneutron stars: A Clue to supernova nucleosynthesis? *Astrophys. J.*, 473:L111, 1996.

[147] A Mezzacappa and S W Bruenn. Type II supernovae and Boltzmann neutrino transport: The Infall phase. *Astrophys. J.*, 405:637–668, 1993.

[148] A Mezzacappa and S W Bruenn. A numerical method for solving the neutrino Boltzmann equation coupled to spherically symmetric stellar core collapse. *Astrophys. J.*, 405:669–684, 1993.

[149] Anthony Mezzacappa and Stephen W Bruenn. Stellar Core Collapse: A Boltzmann Treatment of Neutrino-Electron Scattering. *Astrophys. J.*, 410:740, 1993.

[150] Matthias Liebendorfer, O E Bronson Messer, Anthony Mezzacappa, et al. A Finite Difference Representation of Neutrino Radiation Hydrodynamics in Spherically Symmetric General Relativistic Spacetime. *The Astrophysical Journal Supplement Series*, 150(1):263–316, jan 2004.

[151] Matthias Liebendorfer, Stephan Rosswog, and Friedrich-Karl Thielemann. An Adaptive Grid, Implicit Code for Spherically Symmetric, General Relativistic Hydrodynamics in Comoving Coordinates. *The Astrophysical Journal Supplement Series*, 141(1):229–246, jul 2002.

[152] T Fischer, S C Whitehouse, A Mezzacappa, et al. Protoneutron star evolution and the neutrino driven wind in general relativistic neutrino radiation hydrodynamics simulations. *Astron.Astrophys.*, 517:A80, 2010.

[153] Gang Guo, Gabriel Martínez-Pinedo, A Lohs, and Tobias Fischer. Charged-current muonic reactions in core-collapse supernovae. *Physical Review D*, 102(2):023037, jul 2020.

[154] Tobias Fischer, Gang Guo, Alan A Dzhioev, et al. Neutrino signal from proto-neutron star evolution: Effects of opacities from charged-current–neutrino interactions and inverse neutron decay. *Physical Review C*, 101(2):025804, feb 2020.

[155] Stephen W Bruenn. Stellar core collapse - Numerical model and infall epoch. *The Astrophysical Journal Supplement Series*, 58:771, aug 1985.

[156] James M Lattimer and F.Douglas Swesty. A Generalized equation of state for hot, dense matter. *Nucl.Phys.*, A535:331–376, 1991.

[157] H Shen, H Toki, K Oyamatsu, and K Sumiyoshi. Relativistic equation of state of nuclear matter for supernova and neutron star. *Nucl.Phys.*, A637:435–450, 1998.

[158] Matthias Hempel and Jurgen Schaffner-Bielich. Statistical Model for a Complete Supernova Equation of State. *Nucl.Phys.*, A837:210, 2010.

[159] M Hempel, J Schaffner-Bielich, S Typel, and G Röpke. Light clusters in nuclear matter: Excluded volume versus quantum many-body approaches. *Phys. Rev. C*, 84(5):55804, 2011.

[160] A.∼W. Steiner, M Hempel, and T Fischer. Core-collapse Supernova Equations of State Based on Neutron Star Observations. *Astrophys. J.*, 774:17, 2013.

[161] S Typel. Relativistic model for nuclear matter and atomic nuclei with momentum-dependent self-energies. *Phys. Rev. C*, 71(6):64301, 2005.

[162] S Typel, G Röpke, T Klähn, et al. Composition and thermodynamics of nuclear matter with light clusters. *Phys. Rev. C*, 81:15803, 2010.

[163] S Typel, M Oertel, and T Klähn. CompOSE - CompStar Online Supernovae Equations of State. 2013.

[164] J Antoniadis, P.∼C.∼C. Freire, N Wex, et al. A Massive Pulsar in a Compact Relativistic Binary. *Science*, 340:448, 2013.

[165] Emmanuel Fonseca, Timothy T Pennucci, Justin A Ellis, et al. The NANOGrav Nine-year Data Set: Mass and Geometric Measurements of Binary Millisecond Pulsars. *Astrophys. J.*, 832(2):167, 2016.

[166] F. X. Timmes and Dave Arnett. The Accuracy, Consistency, and Speed of Five Equations of State for Stellar Hydrodynamics. *The Astrophysical Journal Supplement Series*, 125(1):277–294, nov 1999.

[167] T Fischer, G. Martínez-Pinedo, M Hempel, and M Liebendörfer. Neutrino spectra evolution during protoneutron star deleptonization. *Physical Review D*, 85(8):083003, apr 2012.

[168] Ralf Peter Brinkmann and Michael S Turner. Numerical Rates for Nucleon-Nucleon Axion Bremsstrahlung. *Phys. Rev. D*, 38:2338, 1988.

[169] Gang Guo and Gabriel Martínez-Pinedo. Chiral Effective Field Theory Description of Neutrino Nucleon–Nucleon Bremsstrahlung in Supernova Matter. *The Astrophysical Journal*, 887(1):58, dec 2019.

[170] Tobias Fischer. The role of medium modifications for neutrino-pair processes from nucleon-nucleon bremsstrahlung. *Astronomy & Astrophysics*, 593:A103, sep 2016.

[171] S E Woosley, A Heger, and T A Weaver. The evolution and explosion of massive stars. *Rev. Mod. Phys.*, 74:1015–1071, 2002.

[172] Meng-Ru Wu, Yong-Zhong Qian, Gabriel Martínez-Pinedo, et al. Effects of neutrino oscillations on nucleosynthesis and neutrino signals for an $18M_\odot$ supernova model. *Physical Review D*, 91(6):065016, mar 2015.

[173] Shirley Weishi Li, Luke F Roberts, and John F Beacom. Exciting prospects for detecting late-time neutrinos from core-collapse supernovae. *Phys. Rev. D*, 103(2):23016, 2021.

[174] K Abe and Others. Hyper-Kamiokande Design Report. 2018.

[175] G L Fogli, E Lisi, A Mirizzi, and D Montanino. Probing supernova shock waves and neutrino flavor transitions in next-generation water-Cerenkov detectors. *JCAP*, 04:2, 2005.

[176] A Mirizzi, I Tamborra, H.-T. Janka, et al. Supernova neutrinos: production, oscillations and detection. *Nuovo Cimento Rivista Serie*, 39:1–112, 2016.

[177] Alessandro Strumia and Francesco Vissani. Precise quasielastic neutrino/nucleon cross-section. *Phys. Lett. B*, 564:42–54, 2003.

[178] L.∼F. Roberts, G Shen, V Cirigliano, et al. Protoneutron Star Cooling with Convection: The Effect of the Symmetry Energy. *Phys. Rev. Lett.*, 108(6):61103, feb 2012.

[179] Brendan Reed and C J Horowitz. Total Energy in Supernova Neutrinos and the Tidal Deformability and Binding Energy of Neutron Stars. *Phys. Rev. D*, 102(10):103011, 2020.

[180] Andrea Gallo Rosso, Francesco Vissani, and Maria Cristina Volpe. What can we learn on supernova neutrino spectra with water Cherenkov detectors? *JCAP*, 04:40, 2018.

[181] Jonathan Braithwaite and Hendrik C Spruit. A fossil origin for the magnetic field in A stars and white dwarfs. *Nature (London)*, 431(7010):819–821, oct 2004.

[182] Tomoya Takiwaki, Kei Kotake, and Katsuhiko Sato. SPECIAL RELATIVISTIC SIMULATIONS OF MAGNETICALLY DOMINATED JETS IN COLLAPSING MASSIVE STARS. *The Astrophysical Journal*, 691(2):1360–1379, feb 2009.

[183] J M LeBlanc and J R Wilson. A Numerical Example of the Collapse of a Rotating Magnetized Star. *Astrophys.J.*, 161:541, 1970.

[184] C Winteler, R Käppeli, A Perego, et al. MAGNETOROTATIONALLY DRIVEN SUPERNOVAE AS THE ORIGIN OF EARLY GALAXY r -PROCESS ELEMENTS? *The Astrophysical Journal*, 750(1):L22, may 2012.

[185] Philipp Mösta, Sherwood Richers, Christian D Ott, et al. MAGNETOROTATIONAL CORE-COLLAPSE SUPERNOVAE IN THREE DIMENSIONS. *The Astrophysical Journal*, 785(2):L29, apr 2014.

[186] Philipp Mösta, Christian D Ott, David Radice, et al. A large-scale dynamo and magnetoturbulence in rapidly rotating core-collapse supernovae. *Nature (London)*, 528(7582):376–379, dec 2015.

[187] M Kachelriess, C Wilke, and G Wunner. Axion cyclotron emissivity of magnetized white dwarfs and neutron stars. *Phys. Rev. D*, 56(2):1313–1319, jul 1997.

[188] Tomoyuki Maruyama, A Baha Balantekin, Myung-Ki Cheoun, et al. Axion production from Landau quantization in the strong magnetic field of magnetars. *Physics Letters B*, 779:160–165, apr 2018.

[189] Georg Raffelt and Leo Stodolsky. Mixing of the photon with low-mass particles. *Phys. Rev. D*, 37(5):1237–1249, mar 1988.

[190] Andrea Caputo, Pierluca Carenza, Giuseppe Lucente, et al. Axion-like Particles from Hypernovae. *arXiv e-prints*, page arXiv:2104.05727, apr 2021.

[191] D. J. Scalapino. π- Condensate in dense nuclear matter. *Physical Review Letters*, 29(6):386–388, aug 1972.

[192] R. F. Sawyer and D. J. Scalapino. Pion condensation in superdense nuclear matter. *Physical Review D*, 7(4):953–964, feb 1973.

[193] Gordon Baym. Pion condensation in nuclear and neutron star matter. *Physical Review Letters*, 30(26):1340–1342, jun 1973.

[194] Gordon Baym and Elliott Flowers. Pion condensation in neutron star matter: Equilibrium conditions and model calculations. *Nuclear Physics, Section A*, 222(1):29–64, apr 1974.

[195] Chi-Kwan Au and Gordon Baym. Pion condensation in neutron star matter. (II). Nuclear forces and stability. *Nuclear Physics, Section A*, 236(2):500–522, dec 1974.

[196] R. Dashen and J. T. Manassah. Pion phase transition in chiral symmetry breaking model. *Physics Letters B*, 50(4):460–462, jun 1974.

[197] S. Barshay and G. E. Brown. Death to pion condensates in nuclear matter. *Physics Letters B*, 47(2):107–109, oct 1973.

[198] T E O Ericson and Wolfram Weise. *Pions and Nuclei.* Oxford : Clarendon Press, 1988.

[199] J. M. Lattimer. Neutron stars and the nuclear matter equation of state, sep 2021.

[200] E. E. Kolomeitsev, N. Kaiser, and W. Weise. Chiral Dynamics of Deeply Bound Pionic Atoms. *Physical Review Letters*, 90(9):4, mar 2003.

[201] Nadia Fettes, Ulf G. Meißner, and Sven Steininger. Pion-nucleon scattering in chiral perturbation theory (I): Isospin-symmetric case. *Nuclear Physics A*, 640(2):199–234, sep 1998.

[202] E. Epelbaum, A. Nogga, W. Glöckle, et al. Three-nucleon forces from chiral effective field theory. *Physical Review C - Nuclear Physics*, 66(6):17, dec 2002.

[203] Steven Weinberg. Pion scattering lengths. *Physical Review Letters*, 17(11):616–621, sep 1966.

[204] Y. Tomozawa. Pyeryenormirovka aksialcyrillic small soft signno-vyektornoicyrillic, short kostanty svyazi i dliny rassyeyaniya myezona barionom. *Il Nuovo Cimento A*, 46(4):707–717, jan 1966.

[205] M. E. Sainio. Pion-nucleon sigma-term - a review. oct 2001.

[206] Martin Hoferichter, Jacobo Ruiz De Elvira, Bastian Kubis, and Ulf G. Meißner. High-Precision Determination of the Pion-Nucleon σ Term from Roy-Steiner Equations. *Physical Review Letters*, 115(9):092301, aug 2015.

[207] Sz. Borsanyi, Z. Fodor, C. Hoelbling, et al. Ab-initio calculation of the proton and the neutron's scalar couplings for new physics searches. jul 2020.

[208] E. Friedman and A. Gal. On the determination of the pion effective mass in nuclei from pionic atoms. *Physics Letters, Section B: Nuclear, Elementary Particle and High-Energy Physics*, 432(3-4):235–240, jul 1998.

[209] E. Friedman. Indications of partial chiral symmetry restoration from pionic atoms. *Physics Letters, Section B: Nuclear, Elementary Particle and High-Energy Physics*, 524(1-2):87–92, jan 2002.

[210] Martin Hoferichter, Jacobo Ruiz de Elvira, Bastian Kubis, and Ulf G. Meißner. Remarks on the pion–nucleon σ-term. *Physics Letters, Section B: Nuclear, Elementary Particle and High-Energy Physics*, 760:74–78, sep 2016.

[211] Bao-An Li, Lie-Wen Chen, and Che Ming Ko. Recent Progress and New Challenges in Isospin Physics with Heavy-Ion Reactions. *Phys. Rept.*, 464:113–281, 2008.

[212] C. Drischler, R. J. Furnstahl, J. A. Melendez, and D. R. Phillips. How Well Do We Know the Neutron-Matter Equation of State at the Densities Inside Neutron Stars? A Bayesian Approach with Correlated Uncertainties. *Physical Review Letters*, 125(20):202702, nov 2020.

[213] D. Adhikari, H. Albataineh, D. Androic, et al. Accurate Determination of the Neutron Skin Thickness of Pb 208 through Parity-Violation in Electron Scattering. *Physical Review Letters*, 126(17):172502, apr 2021.

[214] Brendan T. Reed, F. J. Fattoyev, C. J. Horowitz, and J. Piekarewicz. Implications of PREX-2 on the Equation of State of Neutron-Rich Matter. *Physical Review Letters*, 126(17):172503, apr 2021.

[215] C. J. Horowitz, E. F. Brown, Y. Kim, et al. A way forward in the study of the symmetry energy: Experiment, theory, and observation. *Journal of Physics G: Nuclear and Particle Physics*, 41(9):093001, jul 2014.

[216] J. Estee, W. G. Lynch, C. Y. Tsang, et al. Probing the Symmetry Energy with the Spectral Pion Ratio. *Physical Review Letters*, 126(16):162701, apr 2021.

[217] P. Russotto, S. Gannon, S. Kupny, et al. Results of the ASY-EOS experiment at GSI: The symmetry energy at suprasaturation density. *Physical Review C*, 94(3):034608, sep 2016.

[218] D. Lonardoni, I. Tews, S. Gandolfi, and J. Carlson. Nuclear and neutron-star matter from local chiral interactions. *Physical Review Research*, 2(2):022033, may 2020.

[219] Yeunhwan Lim and Jeremy W. Holt. Neutron Star Tidal Deformabilities Constrained by Nuclear Theory and Experiment. *Physical Review Letters*, 121(6):062701, aug 2018.

[220] C. Drischler, J. W. Holt, and C. Wellenhofer. Chiral effective field theory and the high-density nuclear equation of state, jan 2021.

[221] X. L. Shang, A. Li, Z. Q. Miao, et al. Nucleon effective mass in hot dense matter. *Physical Review C*, 101(6):065801, jun 2020.

[222] Bao-An Li, Bao-Jun Cai, Lie-Wen Chen, and Jun Xu. Nucleon Effective Masses in Neutron-Rich Matter. *Prog. Part. Nucl. Phys.*, 99:29–119, 2018.

[223] Barry J. Harrington and Harvey K. Shepard. Superconducting properties of pion condensates. *Physical Review D*, 16(12):3437–3449, dec 1977.

[224] Gordon Baym, Christopher Pethick, and David Pines. Superfluidity in neutron stars, 1969.

[225] Mark Alford, Matt Braby, Mark Paris, and Sanjay Reddy. Hybrid Stars that Masquerade as Neutron Stars. *The Astrophysical Journal*, 629(2):969–978, aug 2005.

[226] Robert H. Swendsen. *An introduction to statistical mechanics and thermodynamics.*

[227] Steven P. Harris. *Transport in neutron star mergers.* PhD thesis, may 2020.